



Norwegian University of
Science and Technology

Optimization of Electrical Conductivity in Screw Extruded Wires

Geir Langelandsvik

Materials Science and Engineering

Submission date: June 2017

Supervisor: Hans Jørgen Roven, IMA

Co-supervisor: Trond Furu, IMA
Oddvin Reiso, IMA

Norwegian University of Science and Technology
Department of Materials Science and Engineering

Preface

This master's thesis is written at NTNU, Department of Materials Science and Engineering, during spring 2017. The thesis is a result of research collaboration between NTNU and Hydro Aluminium. I hereby declare that this master's thesis has been done independently and in accordance with regulations at NTNU.

Geir Langelandsvik

Geir Langelandsvik
NTNU Trondheim
June 2017

Acknowledgement

I would like to thank the following persons for help and guidance making this Master's thesis:

Staff Engineer Torild Krogstad and Chief Engineers Trygve Lindahl Schanche and Pål Christian Skaret for tutorial guidance with experimental equipment.

Senior Engineer Yingda Yu for assistance with electron microscopy.

Adjunct Professors Trond Furu and Oddvin Reiso for close guidance throughout the project period.

And last, Professor Hans Jørgen Roven, for rewarding guidance and fruitful discussions.

Aims of work

This master's thesis seeks to assess the effect of alloying elements in solid solution and in precipitated state on electrical properties. Extra attention will be given to the influence of iron, and how the formation kinetics of ferrous intermetallic particles behave during tempering.

The study aims at developing a precise method to evaluate which factors characterize a well-performing electrical conductor. Three different methods will be evaluated and compared in these terms; wire drawing, isothermal tempering and screw extrusion.

The screw extrusion method of aluminium is under continuous development. To achieve the aim of commercializing screw extrusion, it is crucial to understand the microstructural development during extrusion and eventual tempering. Several characterization techniques are utilized in this thesis to determine how commercial pure aluminium behaves under these two processes.

Abstract

In this thesis, the novel production method of screw extrusion was used to produce an electrical conducting wire of commercial pure aluminium. To optimize electrical properties, effects of impurity atoms in solid solution were examined by resistance measurements and microstructural analysis by light optical microscopy, SEM and TEM.

Performed actions revealed that precipitation of iron is a major contributor to increasing the electrical conductivity of aluminium. Precipitation kinetics, summarized in a newly assessed TTT-diagram, showed the most rapid precipitation around 450 °C, Figure 51. The produced screw extruded wire had a fine sub-grain structure arising from repeated deformation, recrystallization and concurrent precipitation during extrusion. The final product performed very well in terms of ultimate tensile strength and electrical conductivity; 61 MPa and 64.30 %IACS, respectively. Tempering after screw extrusion resulted in a decreased conductivity, but with a slight enhancement of the tensile strength.

Sammendrag

I denne oppgaven har elektrisk ledende tråder av kommersielt renaluminium har blitt produsert ved skruuekstrudering. For å optimalisere elektriske egenskaper har effekten av fremmedatomer i fast løsning blitt undersøkt gjennom resistansemålinger og mikrostrukturnalyse i LOM, SEM og TEM.

Undersøkelser viser at presipitering av jern er en viktig bidragsyter til å øke ledningsevnen i aluminium. Et nykonstruert TTT-diagram viser at presipiteringskinetikken er raskest ved 450 °C, se figur 51. Produsert tråd ved skruuekstrudering fremviste en fin sub-kornstruktur som følge av gjentakende deformasjon, rekrySTALLISASJON og samtidig presipitering under ekstrudering. Produktets sluttegenskaper viste en god kombinasjon av strekkfasthet og elektrisk ledningsevne, henholdsvis 61 MPa og 64.30 %IACS. Varmebehandling etter skruuekstrudering resulterte i en svekkelse av ledningsevne, men med noe antydning til økt fasthet.

Contents

Preface	i
Acknowledgement	iii
Aims	v
Abstract	vii
Sammendrag	ix
1 Introduction	1
2 Theoretical background	3
2.1 Wire drawing	3
2.2 Screw extrusion	3
2.3 The Al-Fe and Al-Fe-Si phase systems	4
2.4 Precipitation and recrystallization	6
2.5 Electrical conductivity and resistivity	7
2.6 Mathiessen's rule	9
2.6.1 Contribution of temperature	9
2.6.2 Contribution of dislocations and point defects	10
2.6.3 Contribution of solid solutions and precipitates	10
2.6.4 Contribution of grain size	12
2.7 The International Annealed Copper Standard (IACS)	12
3 Experimental procedure	13
3.1 Base materials	13
3.1.1 Drawn wire	13
3.1.2 Screw extruded wire	13
3.2 Metallographic procedures	14
3.2.1 Sample preparation	14
3.2.2 Microscopy examination	15
3.3 Mechanical measurements	18
3.3.1 Hardness testing	18
3.3.2 Tensile testing	18
3.4 Conductivity measurements	19
3.5 Tempering	20
3.5.1 5 minutes temper of drawn wire	20
3.5.2 Isothermal temper of drawn wire	21
3.5.3 Isothermal temper of screw extruded wire	22
4 Results	25
4.1 Drawn wire - 5 minutes temper	25
4.1.1 Electrical and mechanical properties	25
4.1.2 Microstructure	26
4.2 Drawn wire - Isothermal temper	28
4.2.1 Electrical properties	28
4.2.2 Mechanical properties	28

4.2.3	Grain structure	31
4.2.4	Ferrous particles	32
4.3	Screw extruded wire	37
4.3.1	Electrical properties	37
4.3.2	Mechanical properties	38
4.3.3	Grain structure	41
4.3.4	Particle analysis	47
5	Discussion	53
5.1	Effects of 5 minute temper on drawn wire	53
5.2	Isothermal temper of drawn wire	53
5.2.1	Precipitation mechanisms	53
5.2.2	Mechanical properties	58
5.3	Screw extruded wire	59
5.3.1	Mechanical properties	59
5.3.2	Microstructural evolution during screw extrusion	59
5.3.3	Ferrous particles	60
5.3.4	Oxides	61
5.3.5	Effect of isothermal tempering on screw extruded wire	61
5.3.6	Conductivity evolution	62
5.4	Strength-conductivity relation for electrical conductors	63
6	Conclusion	65
	References	67
	Appendices	I
A	Conversion from resistance to conductivity	I
B	Calibration of AOIP OM21	IX
C	Hardness measurements	XI
D	EDS spectra	XV
E	Risk assessment	XXI

1 Introduction

The electrical conductor market is at present highly competitive. Drawn copper wires are constantly challenged by aluminium solutions with lower cost, better conductivity-to-density ratio and easier availability. Even though aluminium alloys exhibit only half the conductivity of copper, the mentioned reasons have made aluminium an increased market contributor after World War II [1]. This market involves a range of applications, from overhead power lines to wiring and electronic transformers.

Electrical conducting wires of commercial pure aluminium is today made by cold drawing. These wires show good mechanical properties, while their electrical performance is intermediate. Screw extrusion is mentioned as a possible process to enhance the conductivity without compromising the strength redundantly. Hydro and NTNU have in collaboration developed this novel extrusion method which enables continuous feeding of granular material. This introduces major benefits in terms of energy consumption and cost. Firstly, the possibility of utilizing scrap metal with low purchase costs is an eco-friendly as well as profitable solution versus remelting. With continuous extruding, intermediate processing steps can be evaded. The location independence of the extruder represents another benefit. If screw extrusion proves to be economically beneficial, huge market shares lay ahead.

This thesis will compare commercial wire drawing and screw extrusion for a 1XXX aluminium alloy. Differences in electrical conductivity, mechanical properties and microstructure will be revealed and discussed.

2 Theoretical background

2.1 Wire drawing

Wire drawing is a forming process where a billet is pulled through one or several dies to reduce the cross-sectional area and increase length. The process is particularly utilized for drawing conductors for the automotive and electronic industry [2]. The process resembles extrusion, except the wire is pulled through the die, not pushed. Circular geometry is the most common product, but more complex shapes can be produced. Most drawing operations of aluminium are performed at room temperature. Figure 1 show a conceptual sketch of the wire drawing process.

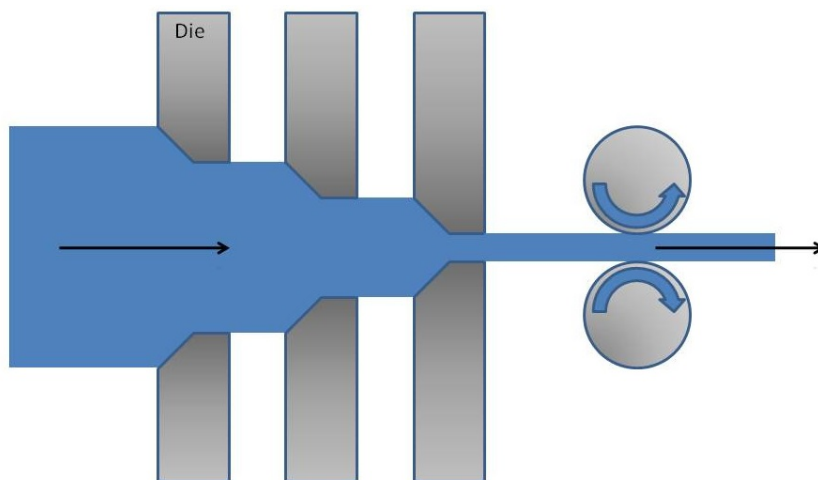


Figure 1: Principal sketch of wire drawing. A billet is pulled through several dies to produce wire. Figure from [3].

Several parameters influence the end product; area reduction, number of die steps, drawing speed, die angle and use of lubrication are amongst them. The degree of area reduction is related to plastic strain and hence work hardening, which increases the dislocation density. Drawing speed and die angle can alter the frictional force between die and wire, inducing unwanted heating of the material. The use of liquid lubricants solves this issue satisfactorily in today's industry [4, 5].

2.2 Screw extrusion

Prolonged collaboration between Hydro and NTNU has resulted in a unique, continuous extrusion process. It involves a rotating screw supplied with granulated feedstock, which extrude a wire through a stationary die. Figure 2 shows a conceptual sketch of the extruder.

The process starts by feeding cleaned, granulated raw material in the rear end of the extruder. Raw material is transported forward in the chamber by an engine-driven screw, which starts compressing the material. At terminal chamber position, high compression forces from the screw end and chamber walls arise, pushing the raw material through the

die. These forces produce a great amount of heat. To maintain tight operation control, the extruder can be cooled with compressed air and heated by a copper induction coil.

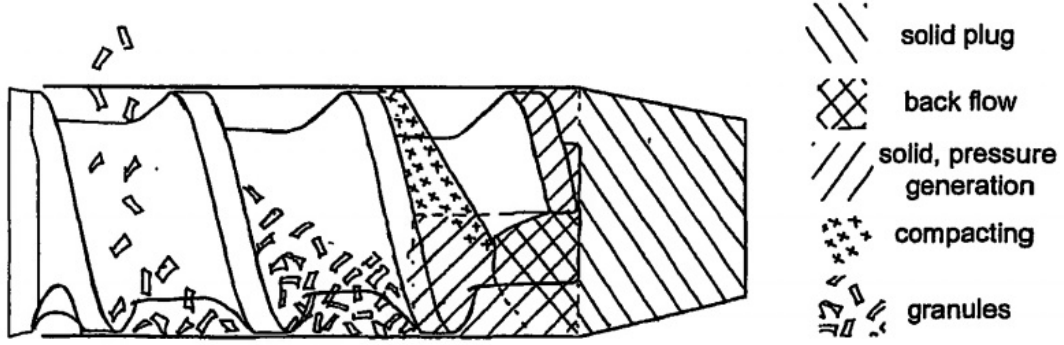


Figure 2: Principal sketch of the screw extruder showing granule feeding and pressure build-up. Figure from [6].

A double flight screw was utilized in this master’s thesis. The double flight design ensures a more symmetric pressure build-up at the extrusion die position. Combined with a steady feeding of material, it yields less probability for producing degraded wires compared to a single flight screw. The increased volume occupation of the double flight represents a drawback, as the extrusion efficiency decreases.

2.3 The Al-Fe and Al-Fe-Si phase systems

The Al-Fe phase diagram has been thoroughly studied through the last century, mainly in the ferro-rich end. Assessments and overviews of the Al-rich part have been provided over the last 30 years [7–10]. A newly assessed phase diagram, contributed by Li et al., is shown in Figure 3 [11]. The low temperature eutectic at 654 °C coincide with the maximum solid solubility of iron in pure aluminium; 0.052 wt%. The solubility decreases rapidly from this value, as seen from Figure 4 [12, 13]. This gives iron a high driving force for precipitation upon cooling. With commercial cooling rates of 0.1 to 100 K⁻¹, a mixture of stable and metastable phases is observed. The mixture consists of stable Al₁₃Fe₄ and metastable Al₅Fe, Al₆Fe and Al₉Fe₂, dependent on cooling rate. An overview is provided in Table 1. The altered conditions of nucleation and growth upon increased supercooling is the reason for formation of metastable phases.

Table 1: Overview of Al-Fe and Al-Fe-Si intermetallic phases. Data from [14–18].

Phase	Space group	Structure	Equilibrium phase
Al ₁₃ Fe ₄	C ₂ m	Monoclinic	Yes
Al ₅ Fe	Unknown	Body-centered tetragonal	No
Al ₆ Fe	Ccmm	Orthohombic	No
Al ₉ Fe ₂	P2 ₁ /c	Monoclinic	No
α-Al ₁₅ Fe ₆ Si ₅ (τ ₅)	P6 ₃ /mmc	Hexagonal	Yes
β-Al ₉ Fe ₂ Si ₂ (τ ₆)	A2/a	Monoclinic	Yes

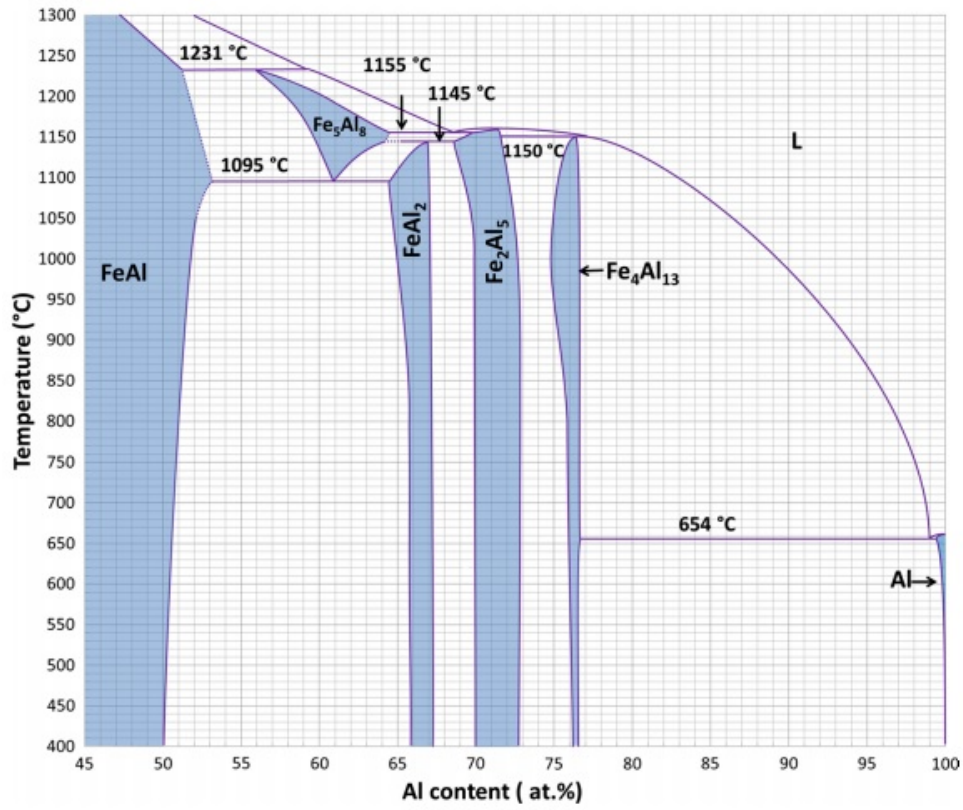


Figure 3: Al-rich part of the binary Al-Fe phase diagram. Figure from [11].

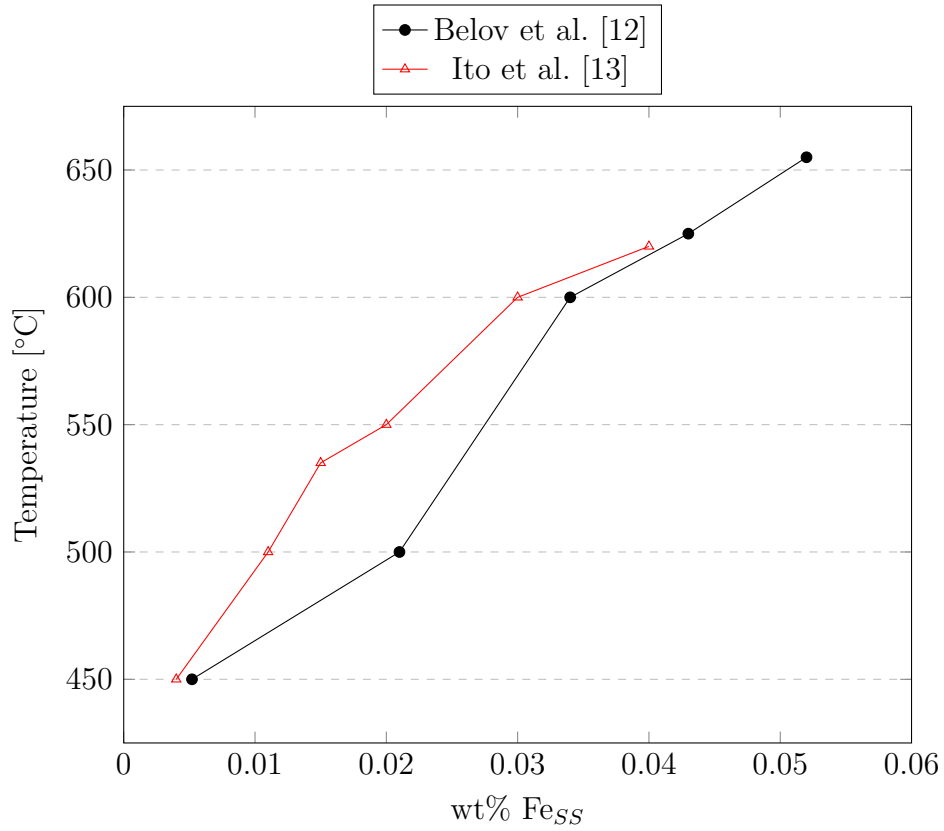


Figure 4: Solid solubility limit of iron in aluminium at different temperatures.

Even dilute additions of silicon to an aluminium-iron alloy affects the final microstructure. Zhao reported an increase of both tensile strength and electrical conductivity of a dilute Al-Si alloy by adding small amounts of iron [19]. This resulted in precipitation of α - and β -Al-Fe-Si intermetallic phases, in addition to mentioned Al-Fe phases. The amount and presence of phases are dependent on composition, cooling rate and quantity of trace elements [14, 19]. The ternary Al-Fe-Si phase diagram at the solidus temperature in metastable condition represents the expected phases, Figure 5 [20]. Composition and structure of the α - and β phases are provided in Table 1.

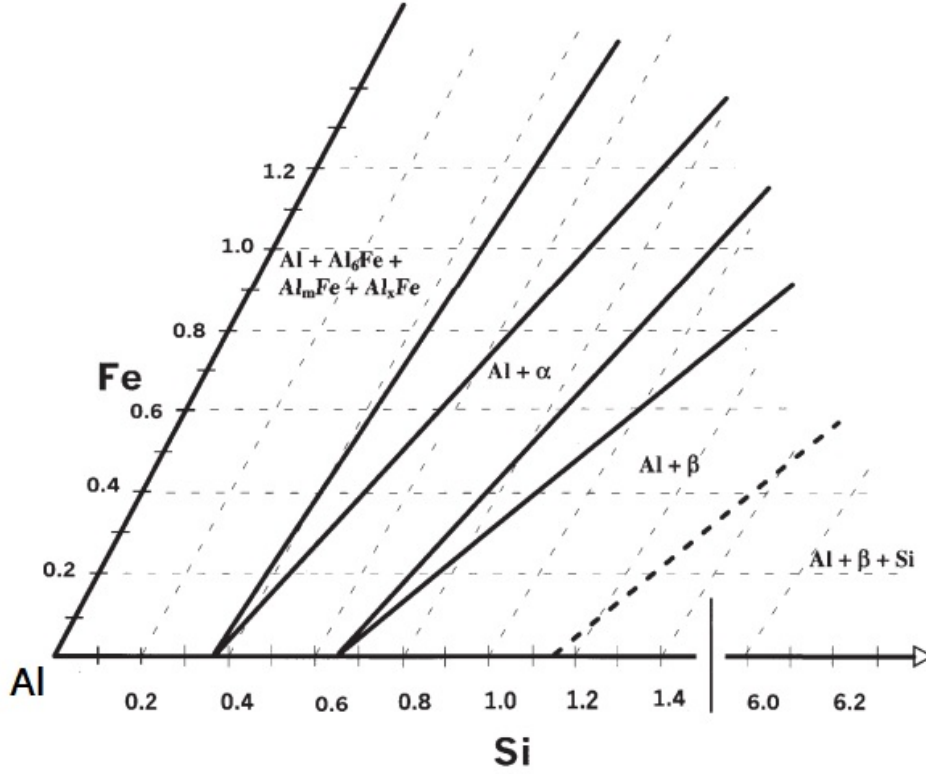


Figure 5: Al-corner of ternary Al-Fe-Si phase diagram at solidus temperature. Figure from [20].

2.4 Precipitation and recrystallization

Precipitation in materials happen when the foreign atom solubility limit is exceeded. Metals usually form precipitates as intermetallic particles, which can deposit heterogeneously or homogeneously. Homogeneous deposition of intermetallic particles happens independently throughout the matrix. The heterogeneous case has preferred nucleation sites, like grain boundaries, vacancy clusters or dislocation networks. The $\text{Al}_{13}\text{Fe}_4$ equilibrium phase is showed to precipitate at grain boundaries and dislocations [21].

Precipitation involves redistribution of atoms into new positions, and therefore is diffusion closely related to this mechanism. Aluminium can precipitate metastable phases or supersaturate alloying elements as a consequence of high supercooling. This is often utilized in heat treatable 6XXX aluminium alloys to increase the strength [22].

When metals are deformed plastically, it stores the imposed energy by creating dislocation

networks and small subgrains within original grains. This stored energy is annihilated upon heating. The supplied heat energy enables the material to rearrange itself to a low-energy state with deformation-free grains; this process is called recrystallization. Recrystallization and precipitation will in certain temperature intervals occur at the same time. This is termed concurrent precipitation. In this case fine precipitates pins the dislocation structure, which inhibits nucleation and growth of new grains [23].

2.5 Electrical conductivity and resistivity

All materials are capable of leading current through its structure to a greater or lesser extent. The classical distinction between conductors are tripartite; electrical conductors, semiconductors and insulators. Metals like aluminium and copper belong to the first group, which conduct electrons very well; silicon to the second group, taking intermediate conduction values; and third polymers and ceramics which are electrical insulating. A fourth sophisticated group, called superconductors, is not encountered here.

The resistance R of a material is proportional to the length L and cross-section area A of the specimen, given by Equation 1:

$$R = \rho \left(\frac{L}{A} \right) \quad (1)$$

where ρ is the electrical resistivity, an intrinsic property of the solid. Conductivity is the inverse property, Equation 2:

$$\sigma = \frac{1}{\rho} \quad (2)$$

The reason for the high conductivity in metals originate from the electronic energy band structure, illustrated in Figure 6. When the highest occupied conduction band is only partly filled with electrons, the amount of energy required to move electrons to higher energy levels is small. This makes numerous electrons free to move, resulting in a great electrical conductivity [24]. For insulators, the energy levels near the Fermi energy are separated by a large band gap, leaving very few electrons free to excite.

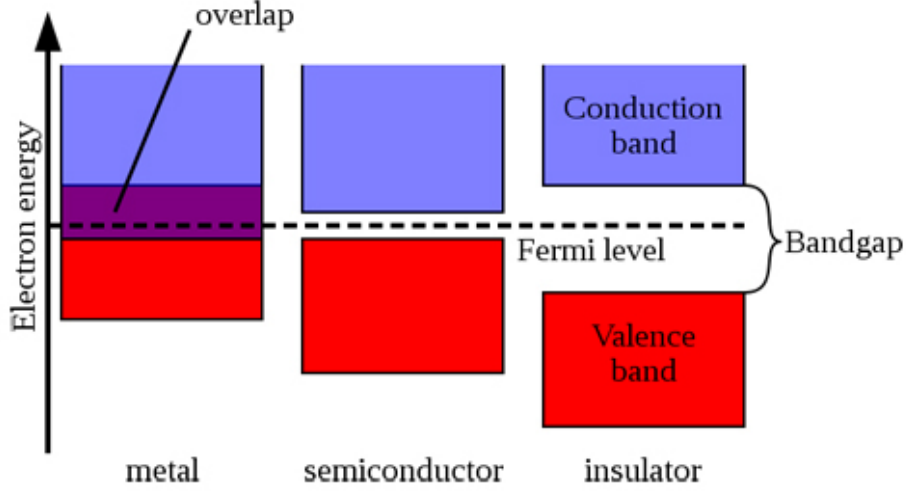


Figure 6: Band structure model for metals, semiconductors and insulators. Overlapping of bands close to the Fermi level governs the electrical conductivity. Figure from [25].

Shape and volume of the Fermi surface influences how well a metal performs as a conductor, as only electrons close to the Fermi energy E_F contribute to the electric current [26]. As seen from Equation 3, conductivity is proportional to the relaxation time τ , where n is number of free electrons, e the electric charge and m_e^* the effective electron mass. τ is related to the Fermi energy through Equation 4, where l is the mean free path between electron collisions. By combining these into Equation 5, it is evident that the Fermi energy affects the intrinsic conductivity properties of a metal [27].

$$\sigma = \frac{ne^2\tau}{m_e^*} \quad (3)$$

$$\tau = \frac{\sqrt{m_e^*}l}{\sqrt{2E_F}} \quad (4)$$

$$\sigma = \frac{ne^2l}{\sqrt{2E_Fm_e^*}} \quad (5)$$

Under optimized conditions, electrons near E_F are easily accelerated and migrate in a desired direction under an electric field. This quantity is termed as mobility μ , and the dependence to conductivity is shown in Equation 6. The mobility of electrons is hampered by several factors, described in the next section.

$$\sigma = ne\mu \quad (6)$$

2.6 Mathiessen's rule

Crystalline lattice defects serve as scattering points for conduction electrons, hampering their free path and flow. This lowers the mobility μ of electrons, thus increasing the resistivity ρ . Empirical results show that the total resistivity is the sum of contributions from thermally excited lattice vibrations (phonons) and lattice imperfections. These mechanisms act almost independently of each other [28]. This observation is summarized in the well-known Mathiessen's rule, Equation 7. $\rho(T)$ is the total resistivity at temperature T , $\rho_L(T)$ and ρ_d the contribution of phonons and defects, respectively. Figure 7 shows a graphical representation of Mathiessen's rule for copper with nickel in solid solution at different temperatures.

$$\rho(T) = \rho_L(T) + \rho_d \quad (7)$$

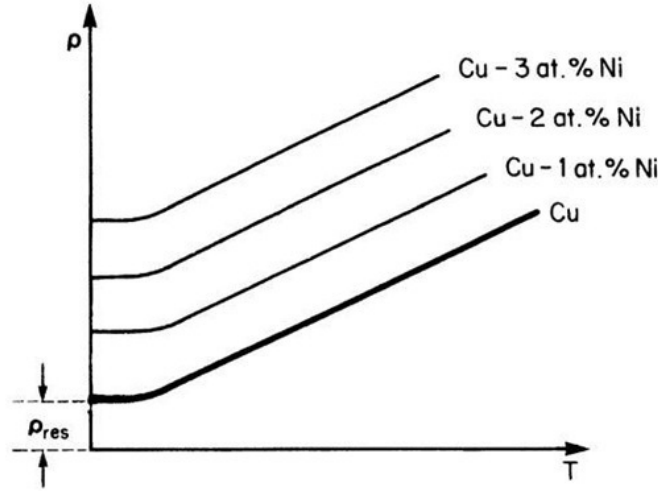


Figure 7: Electrical resistivity for copper at different temperatures. The effect of temperature and lattice impurities are indicated. Figure from [29].

2.6.1 Contribution of temperature

With increasing temperature in the material, the thermal energy will increase the elastic lattice vibrations, so-called phonons [24]. Phonons increase the scattering of electrons, leading to a substantial increase in resistivity for metals, as shown in Figure 7. The linear dependence between resistivity and temperature is given by Equation 8,

$$\rho(T) = \rho_0 + (1 + \alpha(T - T_0)) \quad (8)$$

where ρ_0 is the metals' resistivity at the given temperature T_0 , α the empirical temperature resistivity coefficient and $(T - T_0)$ the temperature difference.

2.6.2 Contribution of dislocations and point defects

Point and line defects like vacancies and dislocations are introduced in the material upon raising temperatures and work hardening. This introduces small defects in the crystal, and work as scattering points for electrons. For dislocations, it is evident that the core and not the elastic strain field is responsible for the scattering [30]. Several studies point out a linear dependence between dislocation density and resistivity at low straining levels, illustrated in Figure 8. The resistivity gradient decreases with increasing deformation due to annihilation of dislocations. At very high straining grades, an equilibrium of production and annihilation of dislocations is reached, explaining the flat range in Figure 8 [30, 31].

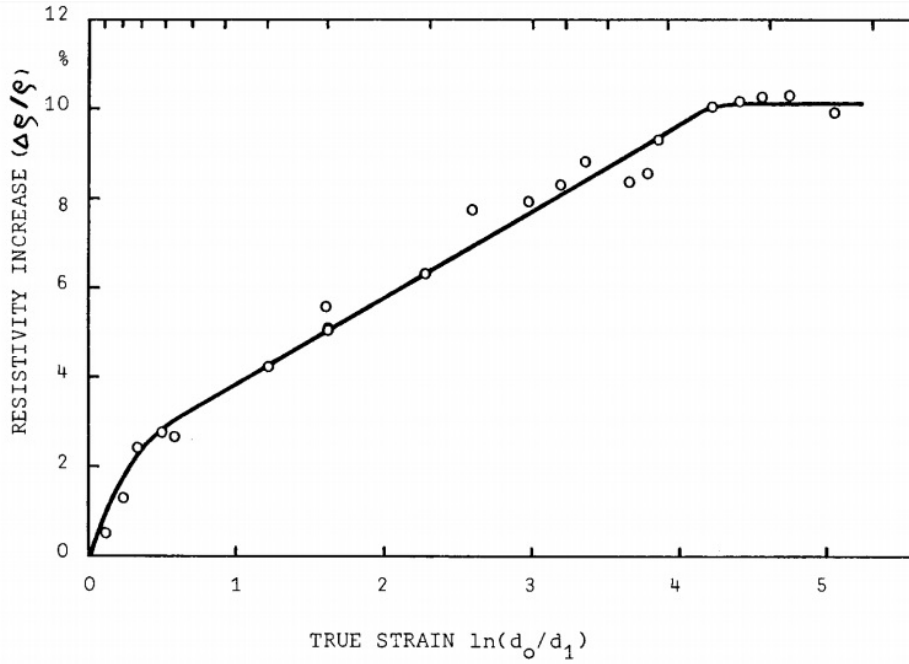


Figure 8: The contribution of dislocations from plastic deformation to increase resistivity of 99.99% pure aluminium. Figure from [30].

2.6.3 Contribution of solid solutions and precipitates

Solid solution of alloying elements in the host lattice is a well-known hardening mechanism. The strain field from the size difference of atoms hampers the dislocation glide. It is also a major contributor to scattering of electrons, thus substitutional solved atoms are often referred to as the most harmful contributor to lower conductivity.

The literature provides several predictions on the contribution of elements in solid solution, and in many different forms. Three models are presented in this thesis. First, Equation 9 by Lok [32], which expresses the resulting conductivity σ in MS/m as a function of weight% iron, manganese and silicon in solid solution ($Fe_{SS}\%$, $Mn_{SS}\%$ and $Si_{SS}\%$, respectively). Second, Kutner quantify the resistivity increase in $\text{p}\Omega\text{m}$ for several alloying elements per weight%, presented in Table 2 [33]. Third, Karabay states the conductivity decrease in %IACS per weight% alloying element, graphically shown in Figure 9 [34].

$$\frac{1}{\sigma} = 0.0267 + 0.036Mn_{SS}\% + 0.032Fe_{SS}\% + 0.0068Si_{SS}\% \quad (9)$$

Table 2: Effect of atoms in solid solution on electrical resistivity in aluminium. ρ is specific resistivity in Ωm and c is the concentration in $wt\%$. Data from Kutner [33].

Element	$d\rho/dc$ [$10^{-10} \Omega m/wt\%$]	Element	$d\rho/dc$ [$10^{-10} \Omega m/wt\%$]
Zr	454	Cu	31
Cr	421	B	13
V	333	Zn	10
Mn	307	Fe	9
Ti	259	Ni	5
Mg	56	Pb	2
Si	52	Sn	1

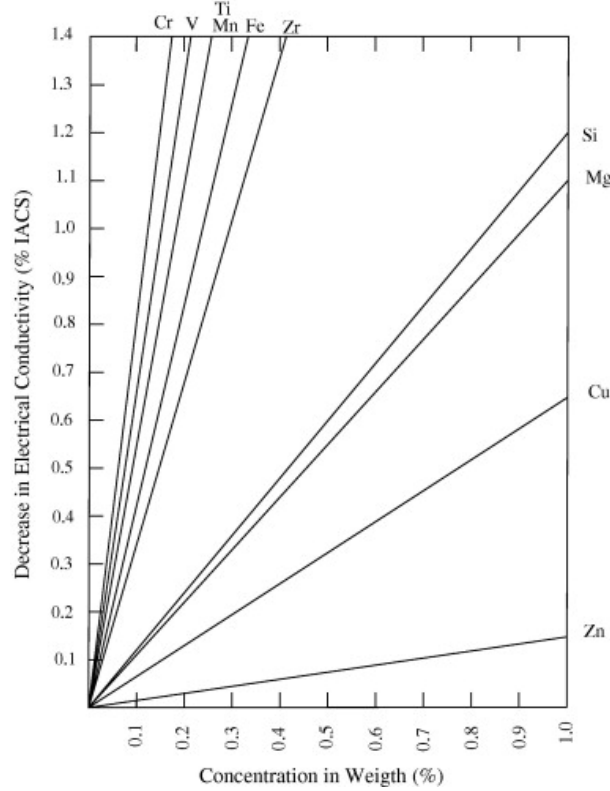


Figure 9: Contribution of atoms in solid solution to lowering electrical conductivity in aluminium. Figure from Karabay [34].

Precipitation of solute elements is one way to avoid loss of conductivity. Additional alloying or heat treatments are possible solutions to encourage precipitation [35, 36]. The work of Olafsson et al. on several commercial aluminium alloys showed, dependent on composition and heat treatment, a contribution of 6-17% from precipitates to the resistivity [37]. Still, precipitates play a role in reducing conductivity, but to a far less extent than atoms in solid solution. The strength gain in particle strengthening and pinning

effects during recrystallization and grain growth may compensate for the conductivity losses.

2.6.4 Contribution of grain size

The lack of crystallinity in grain boundaries make them similar to linear defects, hence reduce conductivity. The expressed contribution is rather minor in commercial alloys, due to the large distances between grain boundaries compared to solute atoms, precipitates and dislocations. For SPD materials with a nano-scaled sub-grain structure, both electrical and mechanical properties are actually enhanced, due to precipitation of alloying elements on grain boundaries and the Hall-Petch effect [38].

2.7 The International Annealed Copper Standard (IACS)

Conductivity in metals are usually in the range of megasiemens per meter (MS/m). A convenient way of comparing conductivity between metals and alloys is referring to the International Annealed Copper Standard (IACS). 100 %IACS is defined as the conductivity of a pure annealed copper wire with cross-section of one square millimeter at 20 °C, corresponding to a numeric value of 58.001 MS/m [39]. A comparison of different metals is provided in Figure 10 [40]. Ultra pure aluminium have approximately half the conductivity of pure copper, 64.94 %IACS [41].

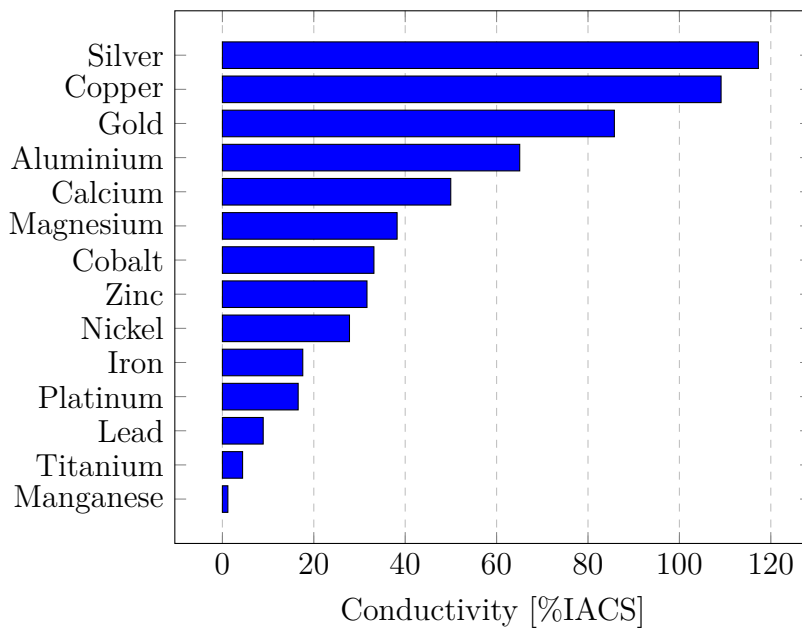


Figure 10: Representation of conductivity for pure metals in terms of %IACS. Data from [40].

3 Experimental procedure

3.1 Base materials

3.1.1 Drawn wire

The tempering processes described in this thesis are performed with a commercial pure, cold drawn aluminium wire. This wire was also the feedstock for screw extrusion. It was produced by Hydro Karmøy and drawn by Nexans down to a diameter of 3.02 mm. Chemical composition for this alloy, belonging to the 1XXX series, is given in Table 3. The information was provided by Hydro Sunndalsøra [42].

Table 3: Chemical composition of drawn 1XXX wire. Data from [42].

Element	Composition [wt%]	Element	Composition [wt%]
Fe	0.157	Ni	0.004
Si	0.058	Ca	0.004
Zn	0.022	Ti	0.002
Cu	0.013	Mn	0.001
Ga	0.013	Pb	0.001
V	0.006	Other	0.004
Na	0.006	Al	Balance

3.1.2 Screw extruded wire

Three series of screw extruded wires were produced autumn 2016 by Langelandsvik [43]. Small pellets of drawn wire was used as feedstock. Prior to extrusion, the feedstock was rinsed in acetone and water, then dried at 120 °C for 12 hours in a Termaks hot closet to resolve moisture. Minimum 24 hours before extrusion, a thermal treatment at 350 °C for 30 minutes was performed in a Nabertherm 85 HA air circulation oven to burn off remaining grease. The cleaning process was based on the work of Bilsbak [44].

The most promising screw extruded wire series, produced with a die temperature equal 450 °C and water quenched, will be examined further in this thesis. Table 4 provides detailed process parameters. A short wire section is shown in Figure 11.

Table 4: Overview of screw extruded wire and process parameters.

Diameter [mm]	Process	Temperature [°C]	Cooling
2.88	Screw extrusion	450	Water quench

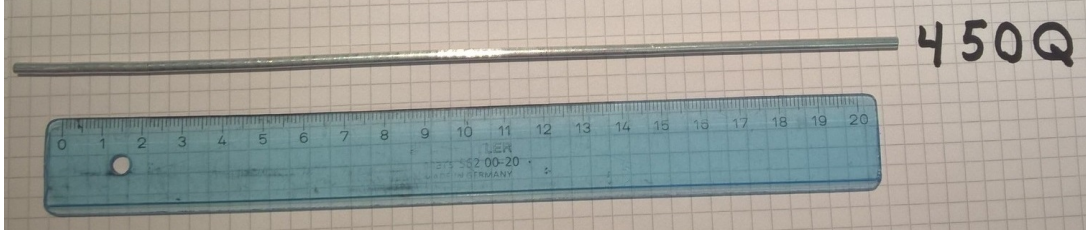


Figure 11: Section of screw extruded wire produced at 450 °C.

3.2 Metallographic procedures

3.2.1 Sample preparation

All samples were mechanically grinded and polished prior to microstructural examinations. Grinding and polishing were performed using a Struers Labopol-21 and Struers TegraForce-5, respectively. The nine step routine to obtain a scratch and deformation free surface is provided in Table 5. Due to the soft matrix of commercial pure aluminium, all samples were prepared by hand and with great care. The reduced disc rotation velocity under the 1 μm polishing steps was in order to avoid spilling of slurry due to high rotational forces. During the two final steps, samples were rotated back and forth, to avoid comet tails in the final microstructure.

Table 5: Procedure for polishing commercial pure aluminium.

Process	Roughness	Grind agent	Velocity (rpm)	Cleaning	Comment
Grinding	#FEPA 320	SiC paper	300	Water	-
Grinding	#FEPA 500	SiC paper	300	Water	-
Grinding	#FEPA 500	SiC paper	300	Water	-
Grinding	#FEPA 500	SiC paper	300	Water	-
Polishing	9 μm	SiC spray	300	Water, soap, ethanol, drying	-
Polishing	3 μm	SiC spray	300	Water, soap, ethanol, drying	-
Polishing	1 μm	Diapro NAP B1 slurry	150	Water, soap, ethanol, drying	-
Polishing	1 μm	Diapro NAP B1 slurry	150	Water, soap, ethanol, drying	Rotating sample
Polishing	40 nm	10% OP-U 90% water	300	Water, soap, ethanol, drying	Rotating sample

In order to highlight the grain structure in polarized light, polished samples were anodized in 5% tetrafluoroboric acid for 90 seconds with an applied voltage of 20 V. Samples were immediately rinsed in water and ethanol after anodizing.

For grain examination using Electron Backscatter Diffraction (EBSD), samples were electropolished using a Struers Lectropol-5, with the ethanol based electrolyte A2-I [45]. The process was executed with an applied voltage of 20 V for 5 seconds at -30 °C. Some EBSD samples had to be prepared without use of aggressive etchants like A2-I. These were instead vibration polished in a Buehler VibroMet2 for 10 hours with a vibration amplitude equal 70%.

Examination of solute precipitation and grain structure of screw extruded- and tempered wires were performed by Transmission Electron Microscopy (TEM). Wires were observed in the longitudinal section, as shown in Figure 12. Sections were prepared to thin foils with 3 mm diameter and a thickness of 80 μm . Foils were then electropolished by using a Struers LaboPol-5 apparatus. A 2:1 mixture of methanol and nitric acid at 20 V was used as etching solution at -30 °C until foils had a small hole in the center.

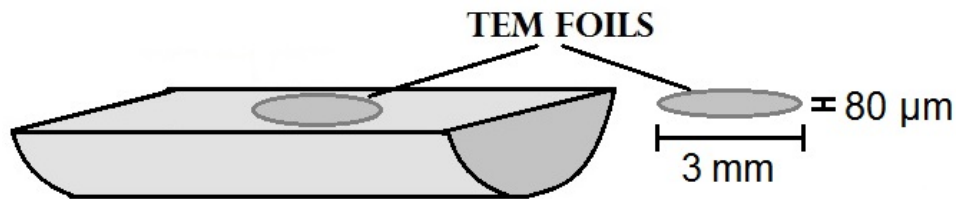
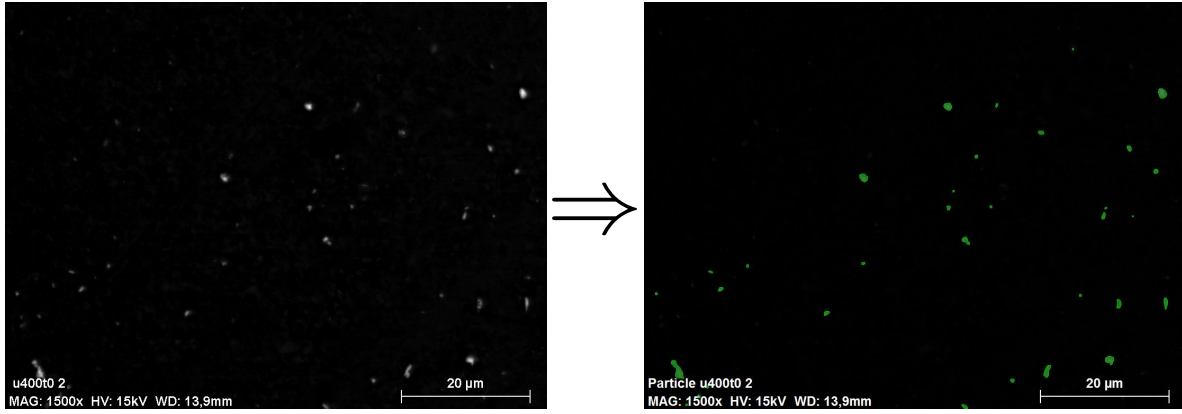


Figure 12: TEM foils prepared from wire length section, i.e. in the mid section.

3.2.2 Microscopy examination

Selected samples were examined in Leica MeF4 Light Optical Microscope (LOM), Figure 14 (a). Polished samples were imaged in bright field, while anodized samples were imaged with cross-polarized light and a sub- λ -plate with a 7° tilt in the column to reveal the grain structure.

Particle area distributions were determined by the computer software Feature connected to the Hitachi SU6600 Field Emission SEM (FESEM), Figure 14 (b). The software calculated the pixel area based on a electron backscatter (BSE) image. To obtain a reliable data collection, the contrast was severely underexposed to approximately binarize the image for processing in Feature. Each sample has an data collection consisting of seven arbitrary chosen areas. One example is shown in Figure 13.



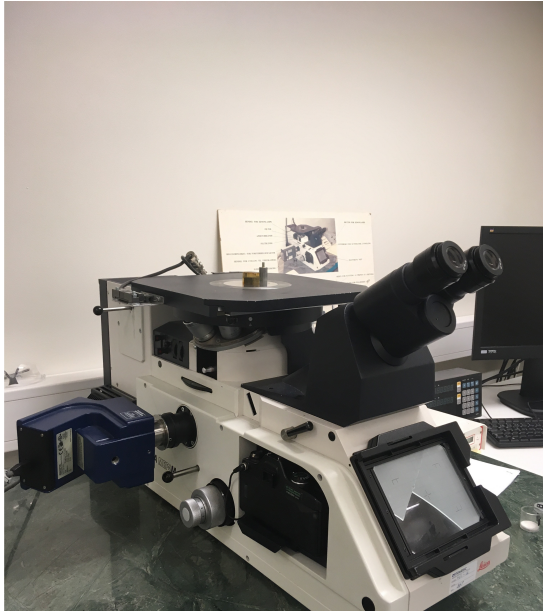
(a) Original BSE image from Hitachi SU6600 (b) Software processed BSE image in Feature

Figure 13: Images for determining particle area distributions in tempered wires.

Quantitative element analysis of particles were performed with backscatter imaging in combination with an Energy Dispersive X-Ray Spectroscopy (EDS) tool attached. A Zeiss Supra 55 VP FESEM with settings 120 μm aperture, 10 keV accelerating voltage and high current mode was used to obtain a precise data collection.

Information of grain structure and texture was obtained by Electron Backscatter Diffraction (EBSD). A Zeiss Ultra 55 Ltd.ed. FESEM, Figure 14 (c), was set up with a 300 μm aperture, 20 keV accelerating voltage and high current mode. An indexing step size ranging from 1-5 μm was chosen dependent on total scanning area. A finer step size was chosen at increasing magnification. EBSD results were post-processed by the computer softwares TSL OIM Data Collection 7 and TSL OIM Analysis 7.

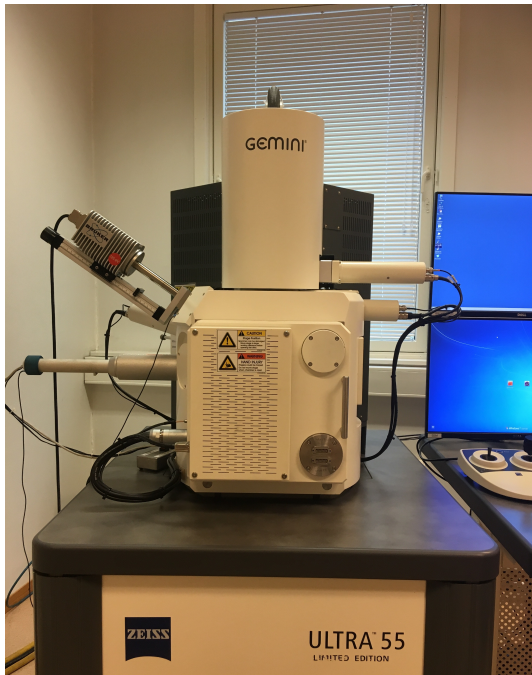
Selected wire specimens were examined in a JEOL JEM-2010 Transmission Electron Microscope, Figure 14 (d). Acceleration voltage equal 200 keV and a double tilt holder was utilized. Images were taken in both bright and dark field mode in a low index zone axis ($\langle 100 \rangle$ or $\langle 110 \rangle$).



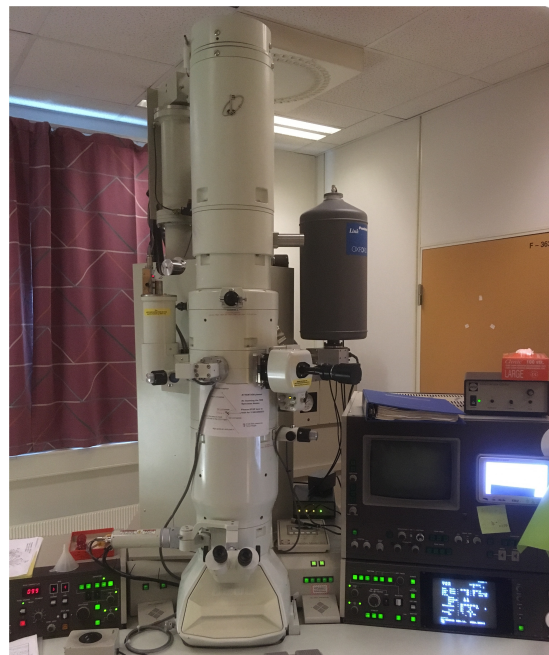
(a) Leica MeF4 Light Optical Microscope.



(b) Hitachi SU6600 Field Emission SEM.



(c) Zeiss Ultra 55 Ltd.ed. Field Emission SEM.



(d) JEOL JEM-2010 TEM.

Figure 14: Images of microscopes utilized for examining the material microstructures.

3.3 Mechanical measurements

3.3.1 Hardness testing

All investigated materials were tested. Samples were grinded with #FEPA 1200 SiC paper before the measurement to ensure consistent results. Testing was performed with a Matsuzawa DVK-1s hardness testing machine, using 1 kilogram force (kgf) and indentation time and depth equal 15 s and 100 μm , respectively. The hardness machine was not calibrated prior to measurements. Every samples had at least six indentations in the central area, as showed in Figure 15. An average of the results are presented in Hardness Vickers, HV.

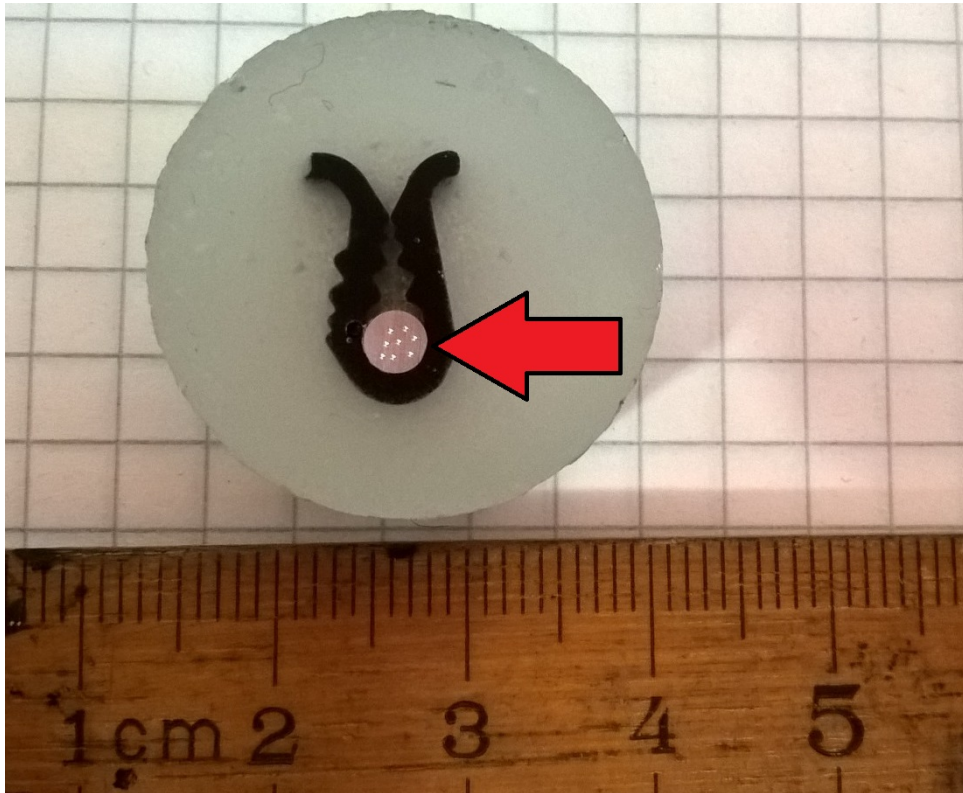
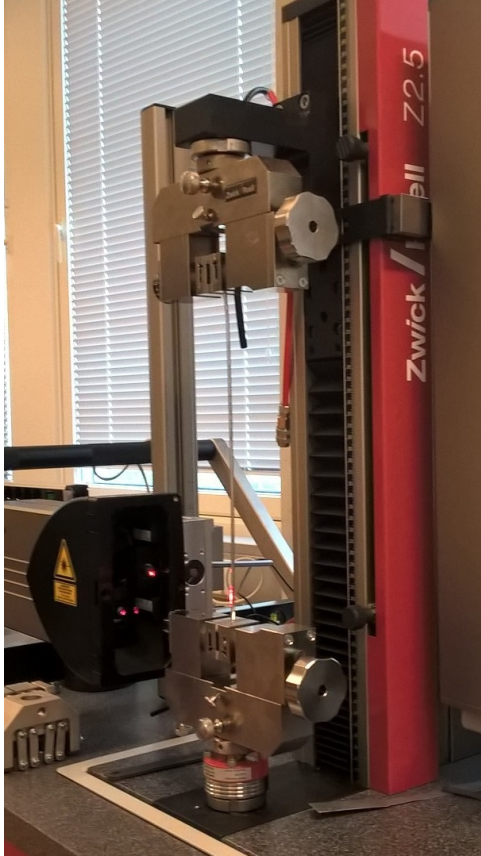


Figure 15: Mounted sample (red arrow) in cross-section showing hardness indentations in the central area.

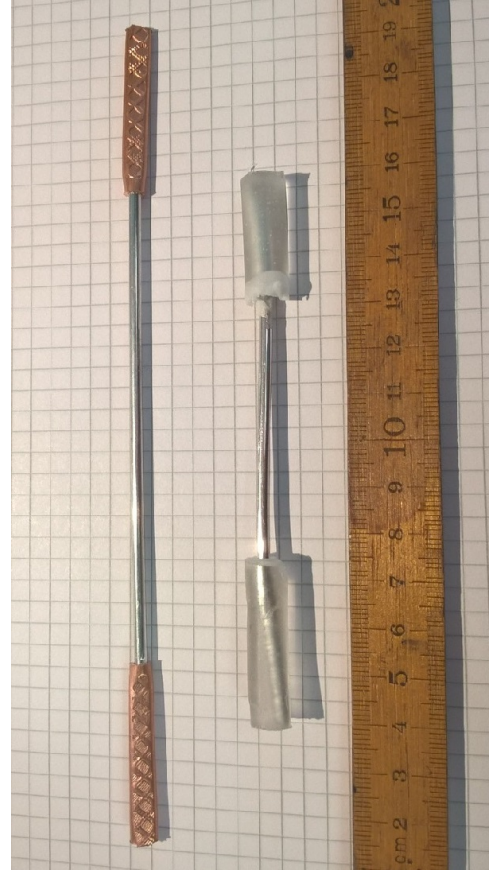
3.3.2 Tensile testing

The mechanical behaviour of wires was identified through uniaxial tensile testing. Due to the narrow wire diameter of approximately 3 mm, the tensile specimen bars were not machined. Instead, 2 cm long copper clamps were pinched at the terminal bar position as shown in Figure 16 (b). This ensured good grip in the tensile machine for the soft, tempered wires. Untempered, drawn wires were harder, which required stronger adhesion between wire and clamp. This was solved by casting epoxy around a grounded wire, see Figure 16 (b). The 'gauge length' was 100 mm and 60 mm for the copper clamped and epoxy clamped specimens, respectively.

The tests were performed using a Zwick Roell 2.5 kN tensile test machine, assembled with a laser extensometer for measuring the engineering strain, Figure 16 (a). The cross-sectional sample area was calculated and all samples were strained until fracture at a crosshead speed of 3 mm/min.



(a) Zwick Roell 2.5 kN tensile machine with laser extensometer.



(b) Tensile specimens with copper (left) and epoxy cast (right) clamps to ensure reliable testing.

Figure 16: Tensile test assemble utilized throughout this thesis.

3.4 Conductivity measurements

The electrical conductivity of wires was determined by an AOIP OM21 microhmmeter, Figure 17. Resistance results from the device were combined with calculated cross-section of wires and distance between measuring points to determine the conductivity. Conversion procedure from resistance to conductivity and associated results are provided in Appendix A.

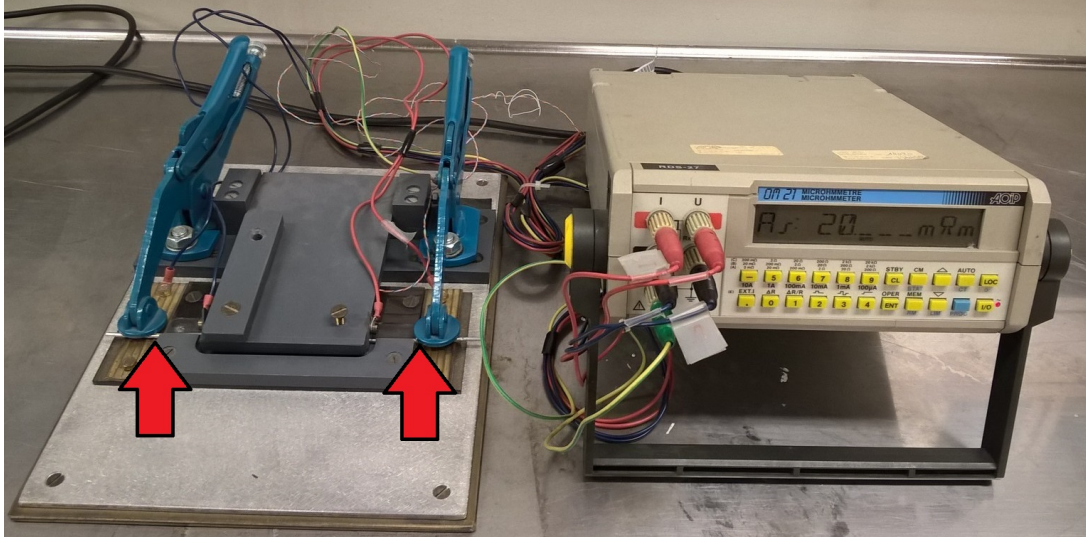


Figure 17: AOIP OM21 microhmmeter. On the left is the metering station with sample inserted (red arrows), the measuring unit to the right.

To ensure reliable measurements, the microhmmeter was calibrated with an ultra pure aluminium Vigeland wire at three different temperatures. The results showed an apparatus uncertainty of $\pm 0.69 \mu\Omega$. Data for this calibration is given in Appendix B.

To ensure straight wires, all samples were stretched in tensile just above the yield point. Shortly before measuring, samples were grinded with #FEPA 240 SiC paper and washed with ethanol to remove the oxide layer and remaining grease. To avoid subsequent fouling and heating from fingers, gloves were used. Wire surface temperature was determined by a K-type thermocouple and fed into the microhmmeter. The microhmmeter was used in temperature compensated mode with a default temperature coefficient of resistance equal 0.4030 K^{-1} . Every sample was measured 16 times in the same position, and an average is presented in %IACS.

3.5 Tempering

3.5.1 5 minutes temper of drawn wire

In order to determine the driving force for recovery, recrystallization and grain growth for the drawn wire, a tempering experiment was carried out. Short pellets and longer bars were utilized for grain inspection and conductivity measurements, respectively. The samples were heated in a Nabertherm 85HA air circulation furnace for five minutes and immediately water quenched. Table 6 provides the experiment parameters. The corresponding grain size was determined by average grain intercept method.

Table 6: Process parameters for short tempering of drawn wires.

Temperature [°C]	Time [min]	Cooling
350	5	Water quench
450	5	Water quench
550	5	Water quench

3.5.2 Isothermal temper of drawn wire

The contribution of iron in solid solution and precipitated state on electrical conductivity was investigated by an isothermal tempering process. Samples of the drawn wire were first solid solution treated at 640 °C for 1 hour. A Nabertherm HR Chamber convection oven with inert argon gas connection to prevent oxidation was used, shown in Figure 19. The inert gas was supplied to a small chamber inside the oven with a feed-rate of 3 L/min. The wires were inserted in the chamber on a steel-plate, which was covered in aluminium foil to prevent iron contamination.

After the solid solution treatment at 640 °C, wires were water quenched. This ensured a high supersaturation of iron in solid solution, Figure 4. It was then isothermally tempered in a salt bath at different temperatures up to 96 hours. The time-temperature lapses are illustrated in Figure 18.

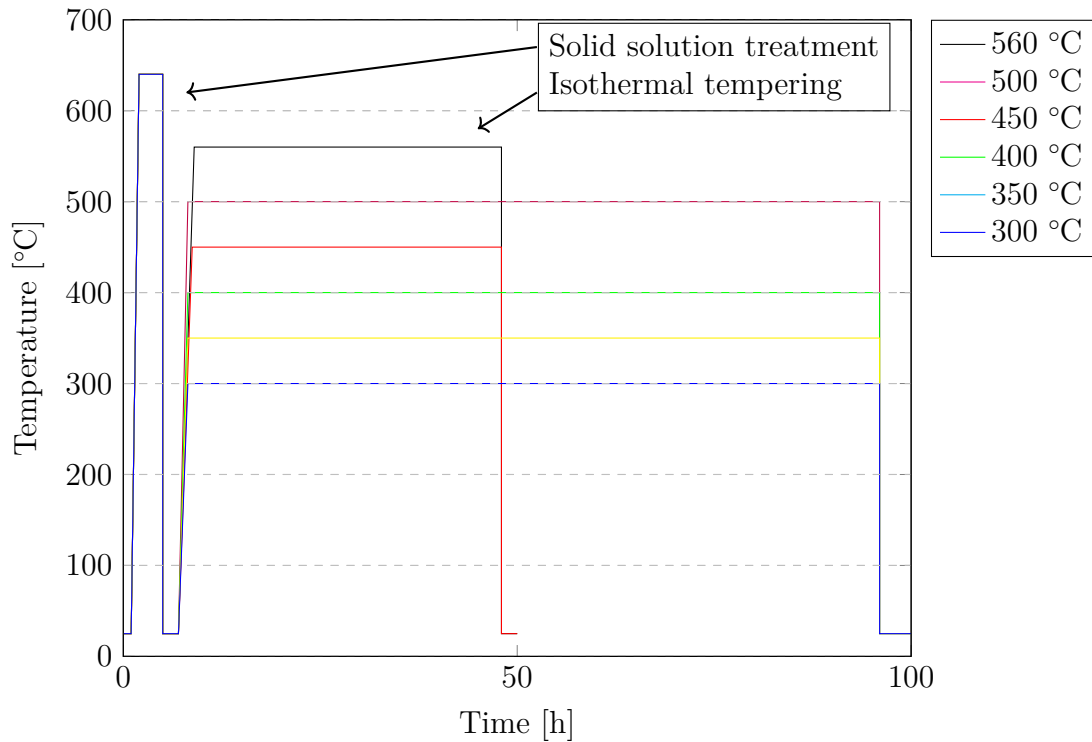
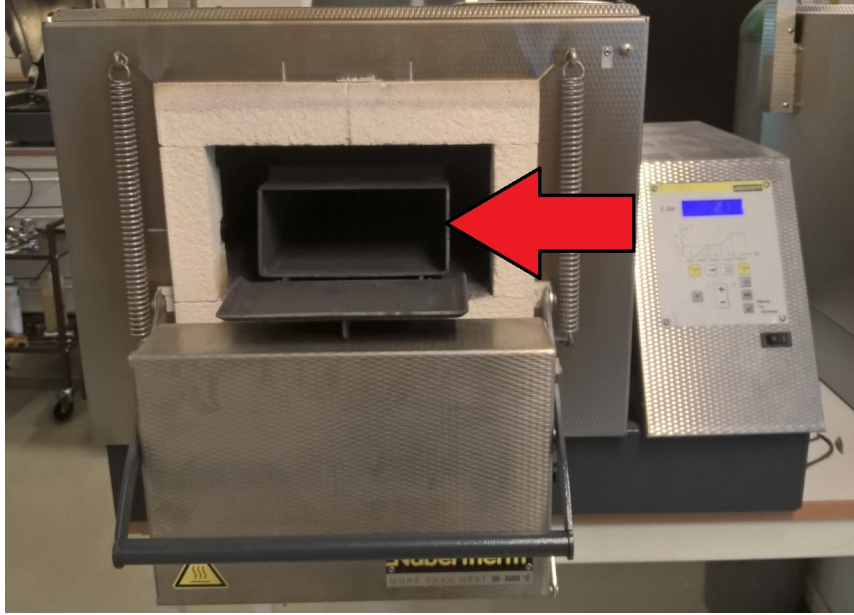


Figure 18: Solid solution treatment and isothermal tempering of drawn wire at different temperatures.



(a) Front. The open argon gas chamber is visible in the oven opening.



(b) Back. Argon gas connection through the blue hose is shown.

Figure 19: Nabertherm HR Chamber convection oven with argon gas connection.

3.5.3 Isothermal temper of screw extruded wire

The as screw extruded wire described in Section 3.1.2 was further tempered at 450 °C in a salt bath. The wire was then water quenched before conductivity and hardness were determined. This were done for five holding times; 0.5, 2, 8, 24 and 96 hours. Due to the small amount of accessible material, the same wire was used for all measuring points. The full time-temperature lapse for this experiment is shown in Figure 20.

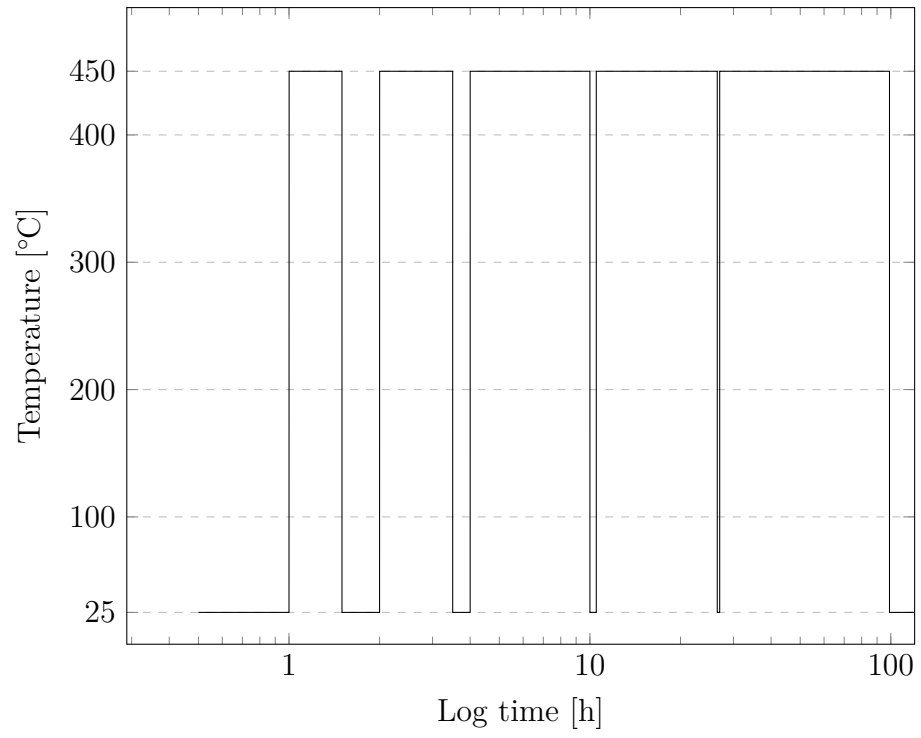


Figure 20: Tempering lapse for screw extruded wire at 450 °C.

4 Results

4.1 Drawn wire - 5 minutes temper

4.1.1 Electrical and mechanical properties

The effect of tempering cold drawn wire for five minutes on electrical conductivity and hardness is presented in Figure 21. The base material for this experiment, the untempered drawn wire, exhibits the lowest conductivity as well as the highest hardness. All samples show a tendency of compromising mechanical and electrical properties. Figure 21 indicates that recrystallization occurs in the range of 350-450 °C, illustrated by the sudden shift in hardness and conductivity.

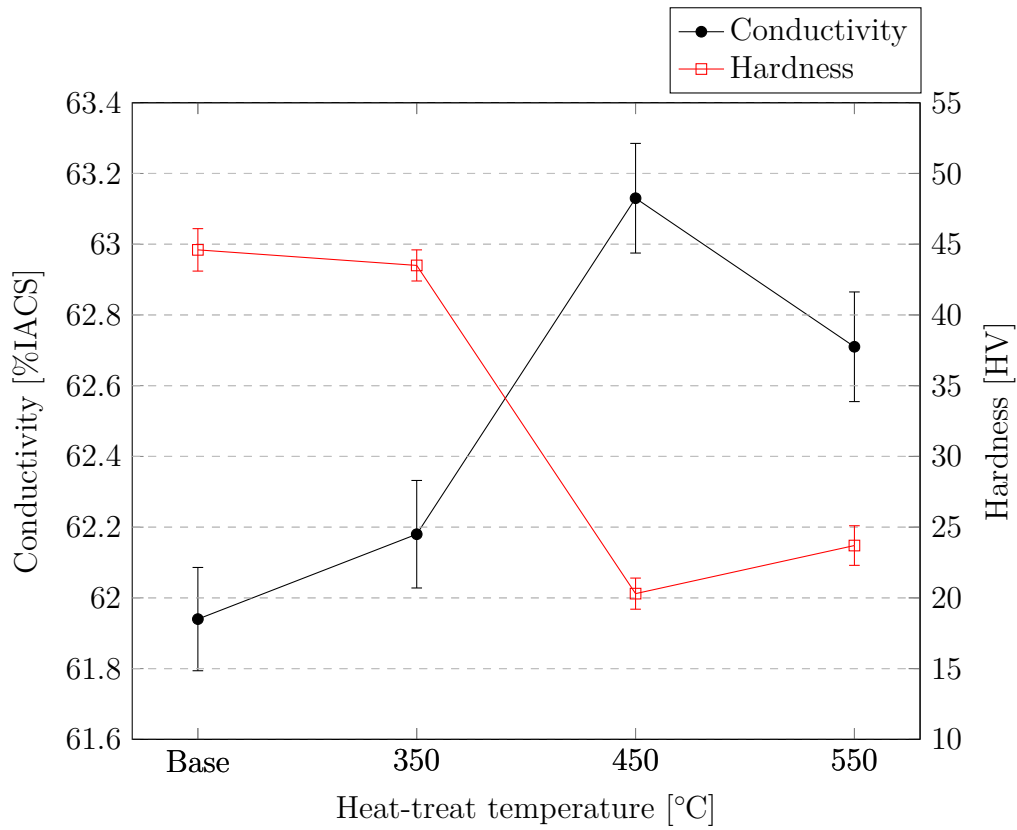


Figure 21: Effect of heat treatment for 5 min on hardness and electrical conductivity for drawn wire.

In order to better understand mechanical properties of the cold drawn wire, it was tensile tested until fracture. The results are presented in Figure 22, which indicated a low-ductile and fairly strong material. Summarized in numbers, the ultimate tensile strength exceeded 160 MPa and the ductility was roughly 2.5%. As shown in in Figure 23, all fractures are in the vicinity of the interface between wire and epoxy cast mounting. This indicates some weakness at this point, and especially the ductility results should be questioned based on this finding.

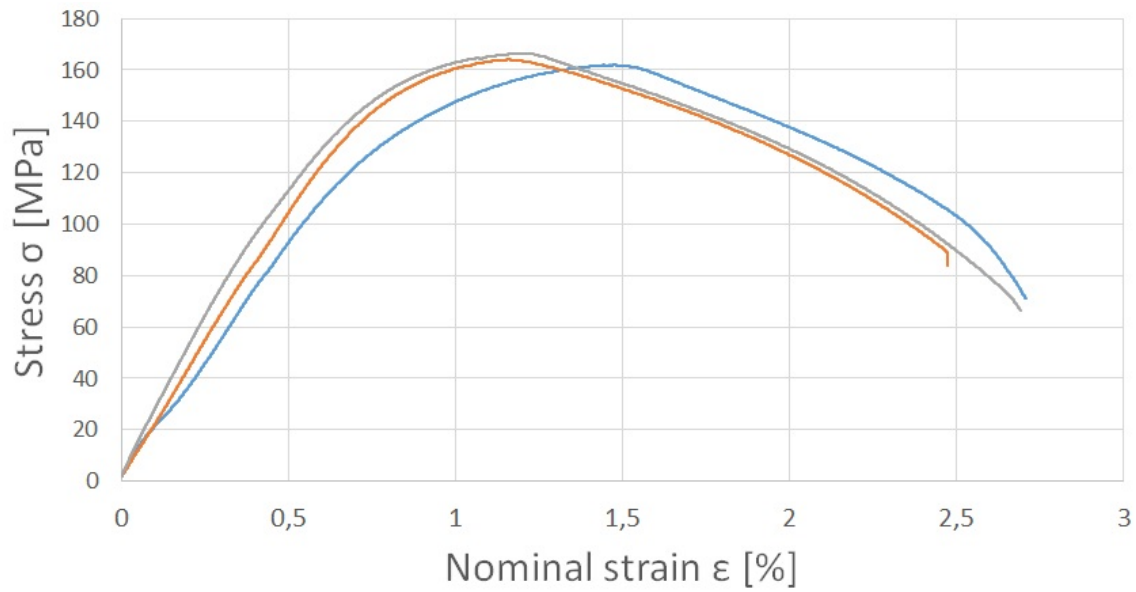


Figure 22: Stress-strain curves for untempered drawn wire.

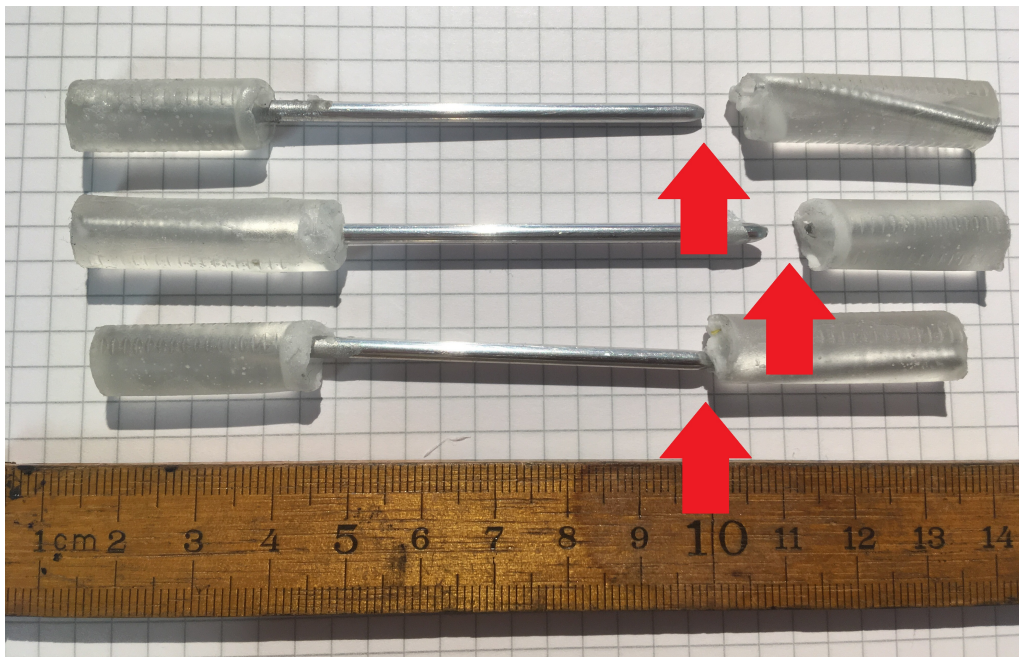
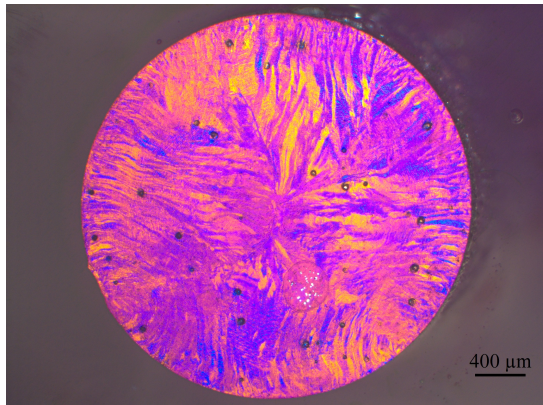


Figure 23: Tensile specimens of untempered drawn wire. All fractures are towards the mounting interface, indicated by red arrows.

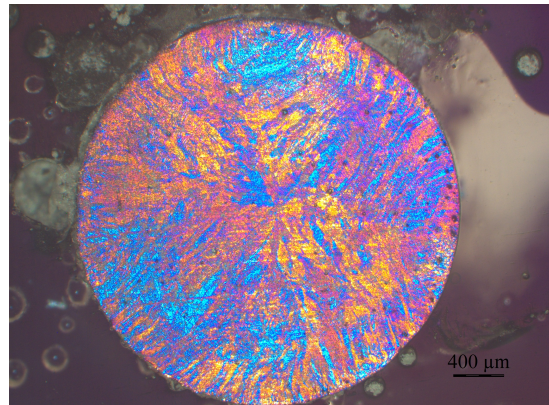
4.1.2 Microstructure

Wires tempered for 5 minutes were imaged in cross-section, Figure 24. The anodized microstructures exhibit the material evolution with increasing temperature. The base material was clearly deformed, and this structure diminished as the temperature was raised. After five minutes at 450 °C, the wire was completely recrystallized, fully in line with the hardness-conductivity curves in Figure 21. This was followed up by grain growth

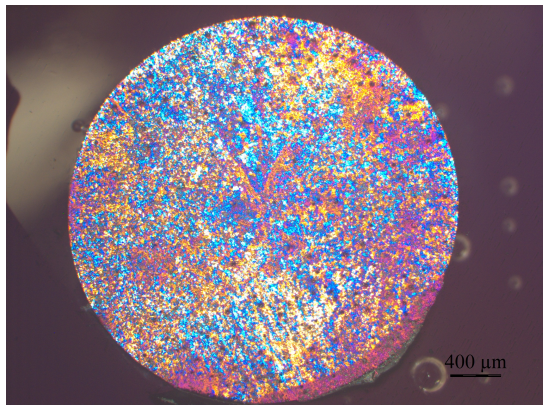
at 550 °C. For the recrystallized cases, it was evident that the grain size was larger in the central region than at the periphery. Data for this observation is displayed in Table 7.



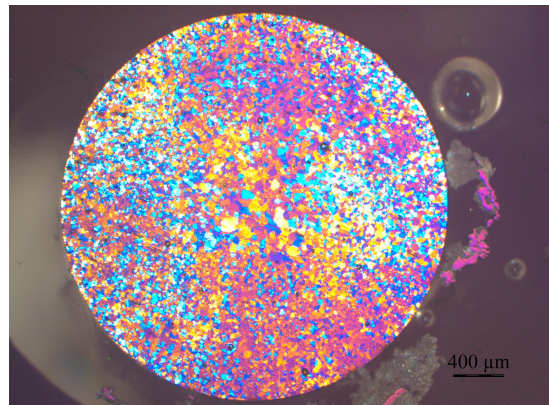
(a) Drawn wire. Deformed structure.



(b) 5 min at 350 °C. Recovered structure.



(c) 5 min at 450 °C. Recrystallized structure.



(d) 5 min at 550 °C. Grain growth.

Figure 24: Cross-section of anodized wires tempered for 5 min. Light optical micrograph, 25X magnification.

Table 7: Grain size of samples exposed to different tempering processes. Based on micrographs in Figure 24

Process	Temperature [°C]	Measure position	Grain size [μm]
None	Base	-	Fibrous
5 min-temper	350	-	Fibrous
5 min-temper	450	Edge	11
5 min-temper	450	Centre	21
5 min-temper	550	Edge	19
5 min-temper	550	Centre	40

4.2 Drawn wire - Isothermal temper

4.2.1 Electrical properties

The solid solution treatment at 640 °C for 1 hour followed by isothermal tempering described in Section 3.5.2 resulted in different conductivity progresses with changing temperatures, Figure 25. All measurements in time = 0 (i.e. after 1 hour at 640 °C) were fairly consistent, close to 62 %IACS. At the lowest temperature of 300 °C (—▲—), no conductivity evolution was seen the first 24 hours of tempering. At 96 hours of temper, this parallel showed a small, but significant, conductivity increase. By raising the temperature to 400 °C (—○—), the material experienced a remarkable conductivity increase. At peak point of 96 hours of tempering, the conductivity was close to the intrinsic properties of ultra pure aluminium. All conductivity results are reported in Appendix A.

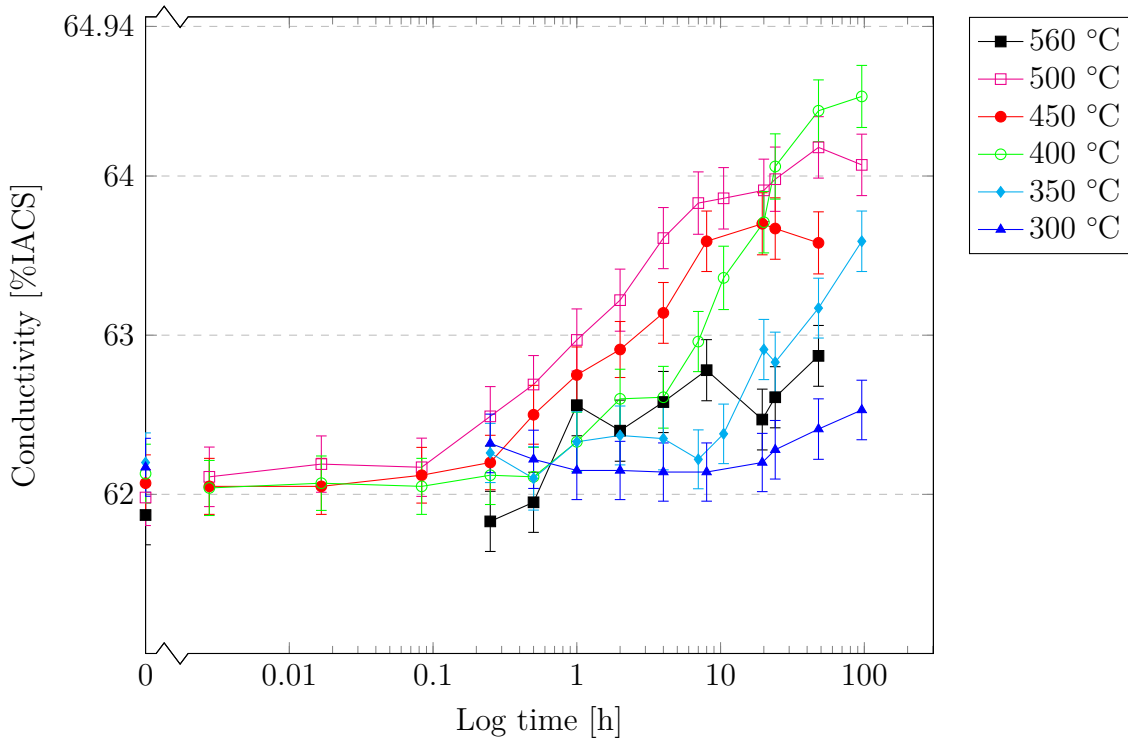


Figure 25: Electrical conductivity evolution with time at different temperatures for isothermal tempered wires.

4.2.2 Mechanical properties

After solid solution treatment of the drawn wire for 1 hour at 640 °C, the hardness dropped as expected from a value of 45 HV to 20-28 HV. Subsequent heating in the range of 300-560 °C did not seem to affect the materials' hardness, Figure 26. This was surprising, given that the conductivity increased with tempering time. The fact that the two most well-performing series in terms of conductivity (400 °C and 500 °C) also showed the highest hardness, was another unexpected result. All hardness data are tabulated in Appendix C

The hardness results seemed to be divided into two groups. One soft group, containing the blue, red and black line (\blacktriangle \bullet \blacksquare); and one harder group, with the cyan, green and magenta parallel (\blacklozenge \circ \square). The two groups of tempering series were prepared separately, which may indicate that the initial solid solution treatment at 640 °C and following quenching did not work identical for the two series.

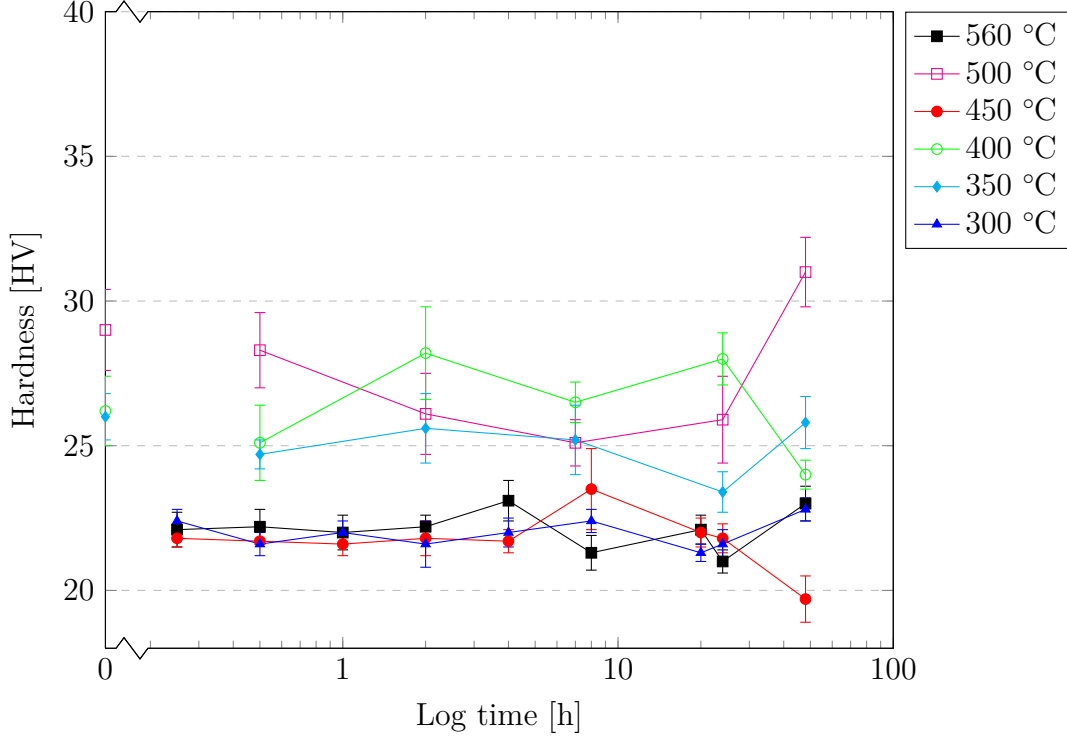
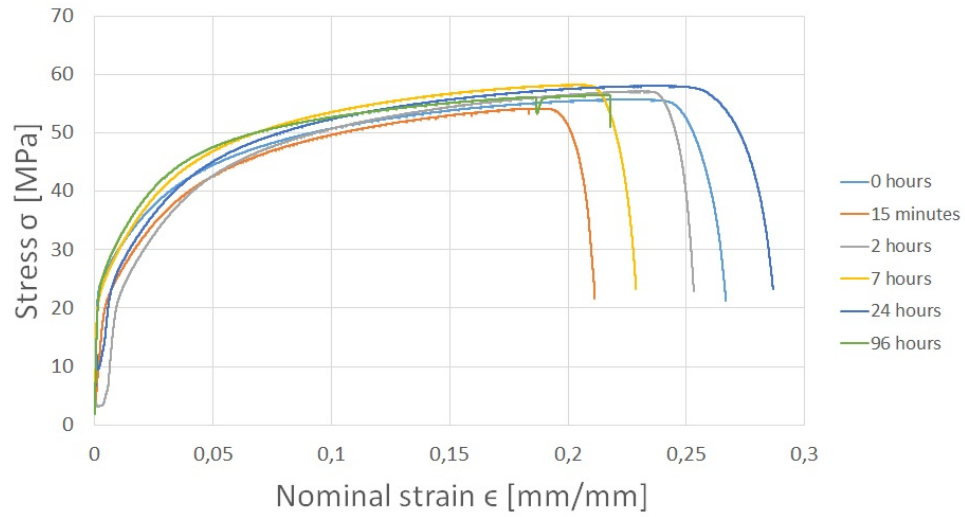
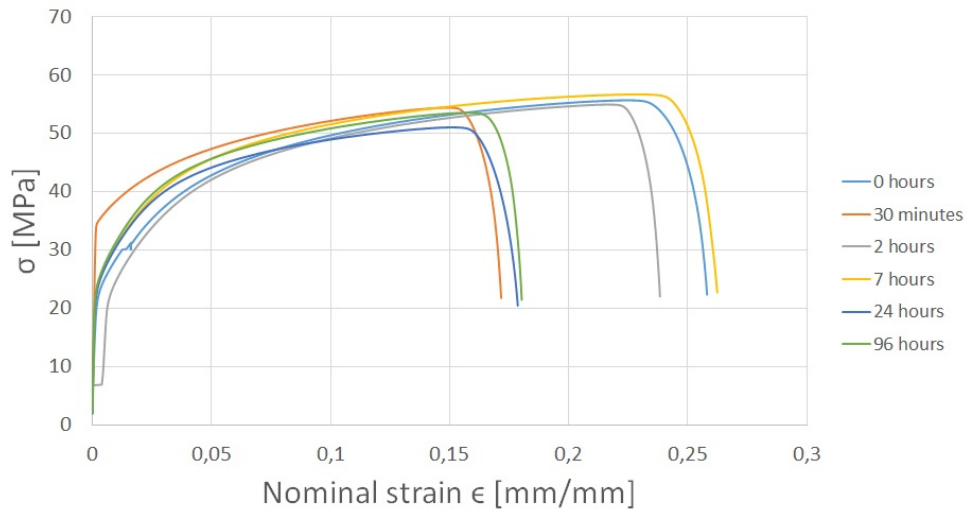


Figure 26: Hardness evolution with time for isothermal tempered wires.

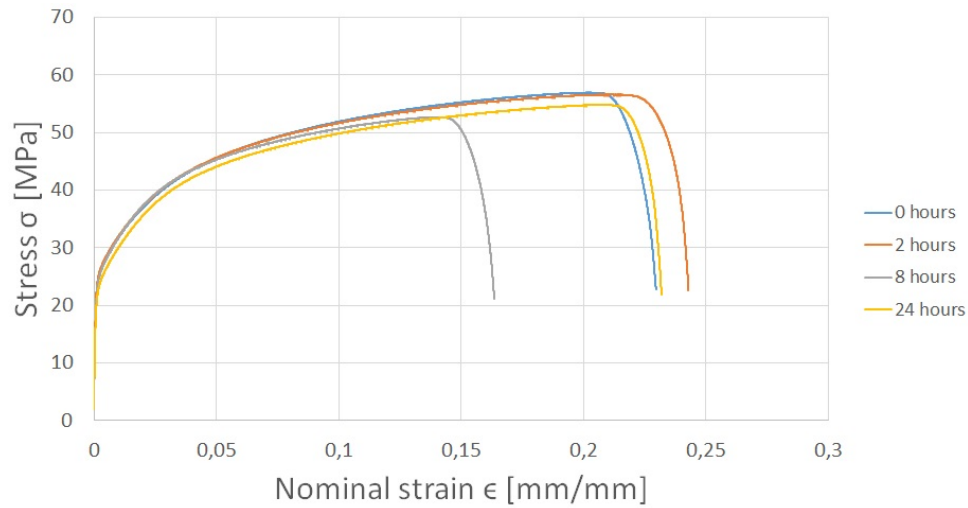
The lack of hardness evolution as a function of time made it desirable to perform tensile testing to further investigate the mechanical properties of isothermal tempered wires. From the stress-strain curves presented in Figure 27, a repeated pattern was clear. After yielding in the range of 20-25 MPa and following strain hardening, the sample fractured without any necking. This affected the determination of both tensile strength and ductility, as all fractures were to some degree premature. The data collection of ultimate tensile strength (UTS) and elongation at fracture (ϵ_f) as a function of time is shown in Figure 28. As these plots display, the UTS and ϵ_f followed each other. This is especially clear for the wire tempered at 450 °C for 8 hours (\bullet), where both quantities were low. Summarized, the tensile strength ranged from 51 to 58 MPa, elongation 16-29%.



(a) Wires tempered at 350 °C



(b) Wires tempered at 400 °C



(c) Wires tempered at 450 °C

Figure 27: Stress-strain curves for isothermal tempered wires.

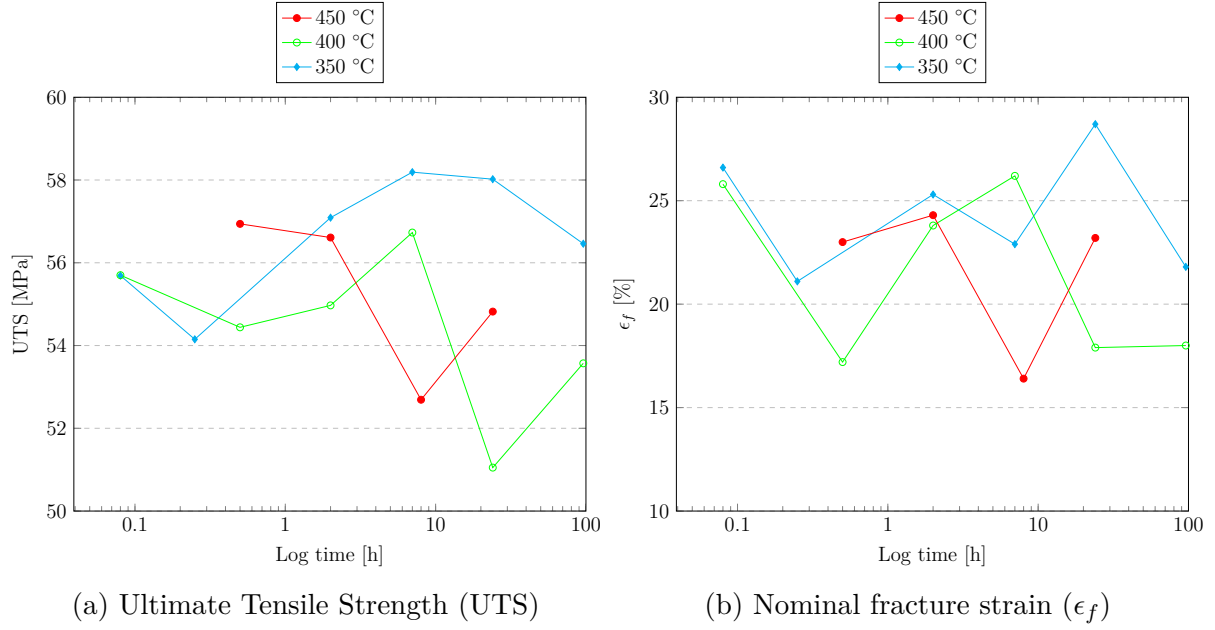
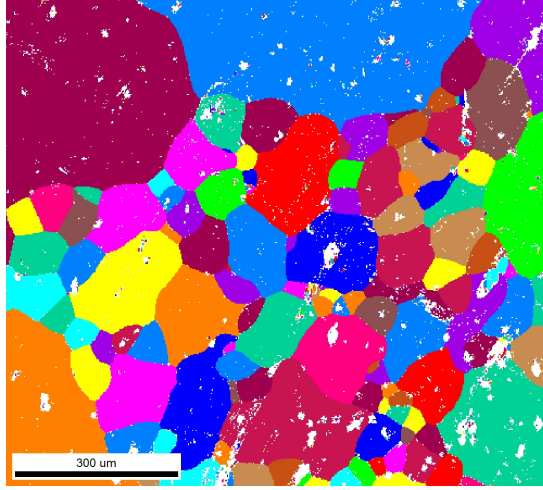


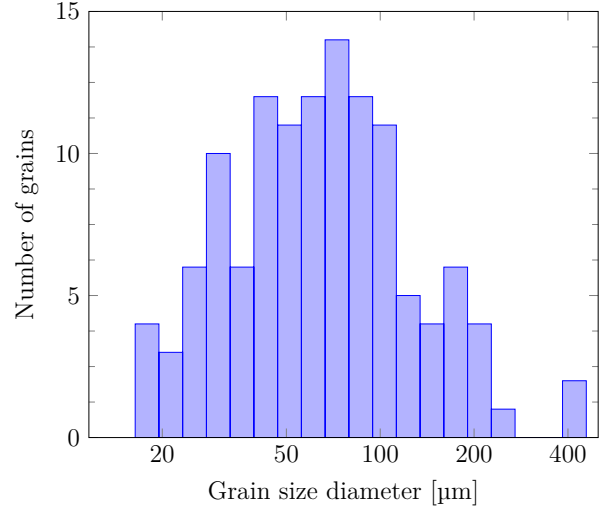
Figure 28: Tensile properties of tempered wires as function of time. Based on stress-strain curves in Figure 27.

4.2.3 Grain structure

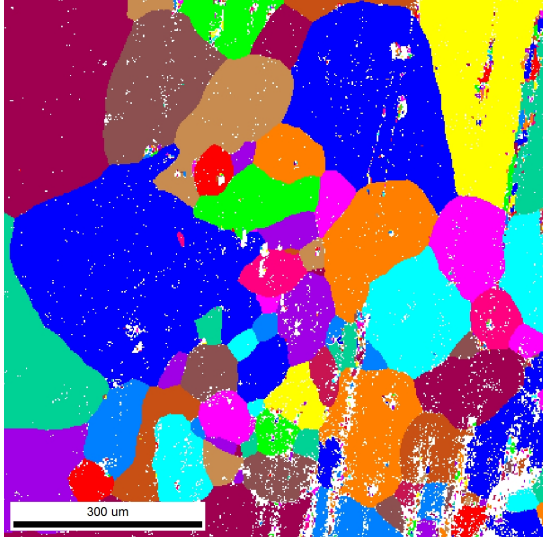
As shown in Figure 24 (a), the untempered drawn wire had a heavily deformed, fibrous microstructure. After solid solution treatment at 640 °C for 1 hour, the microstructure was completely altered. This is illustrated by EBSD grain maps of wires taken in cross-section at 100X magnification in Figure 29 (a)-(b). It shows that all grains were fully recrystallized, and some grew abnormally up to a diameter of 300 μm . The average grain size was measured to be 95 μm . The following isothermal tempering process is illustrated by holding time 20 hours at 450 °C in Figure 29 (c)-(d). The average grain size increased to 116 μm , due to growth of small grains. This shifted the distribution curve towards larger grain sizes in Figure 29 (d), and decreased the total number of grains per unit area. The largest grains were still in the range of 300 μm .



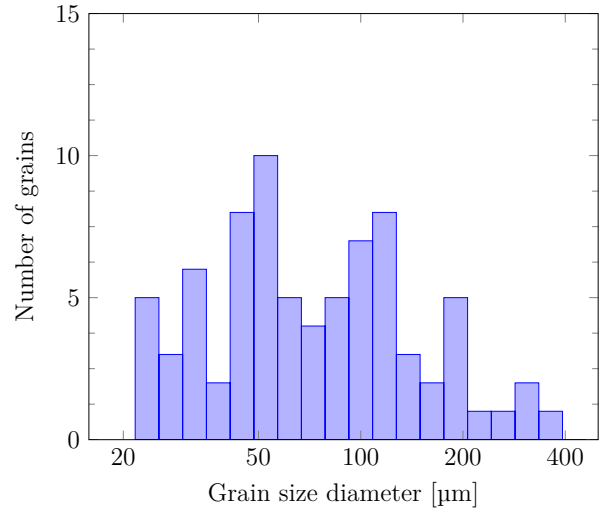
(a) 1 h at 640 °C



(b) 1 h at 640 °C



(c) 1 h at 640 °C + 20 h at 450 °C



(d) 1 h at 640 °C + 20 h at 450 °C

Figure 29: Cross-sectional microstructure of isothermal tempered wires. Left: EBSD grain map, magnification 100X. Right: Grain size diameter distribution.

4.2.4 Ferrous particles

When assuming an iron supersaturated material after 1 hour solid solution treatment at 640 °C with following quenching, deposition of ferrous particles is probable during subsequent isothermal temper. To investigate this, the particles area distribution were determined for two series, isothermally tempered at 400 and 450 °C. The results are presented in Figure 30. The figure shows the particle size evolution from the solid solution treatment at 640 °C to the time representing peak of electrical conductivity. If particles coarsened after tempering, the particle distribution peak of right-hand side plots (Figure 30 b,d) should be right-shifted to higher area values. This was not the case, as all plots show a peak in the range of 0.05-0.20 μm^2 . The diagram, however, do not quantify the number of particles per unit area, it only shows the internal distribution of particles sizes.

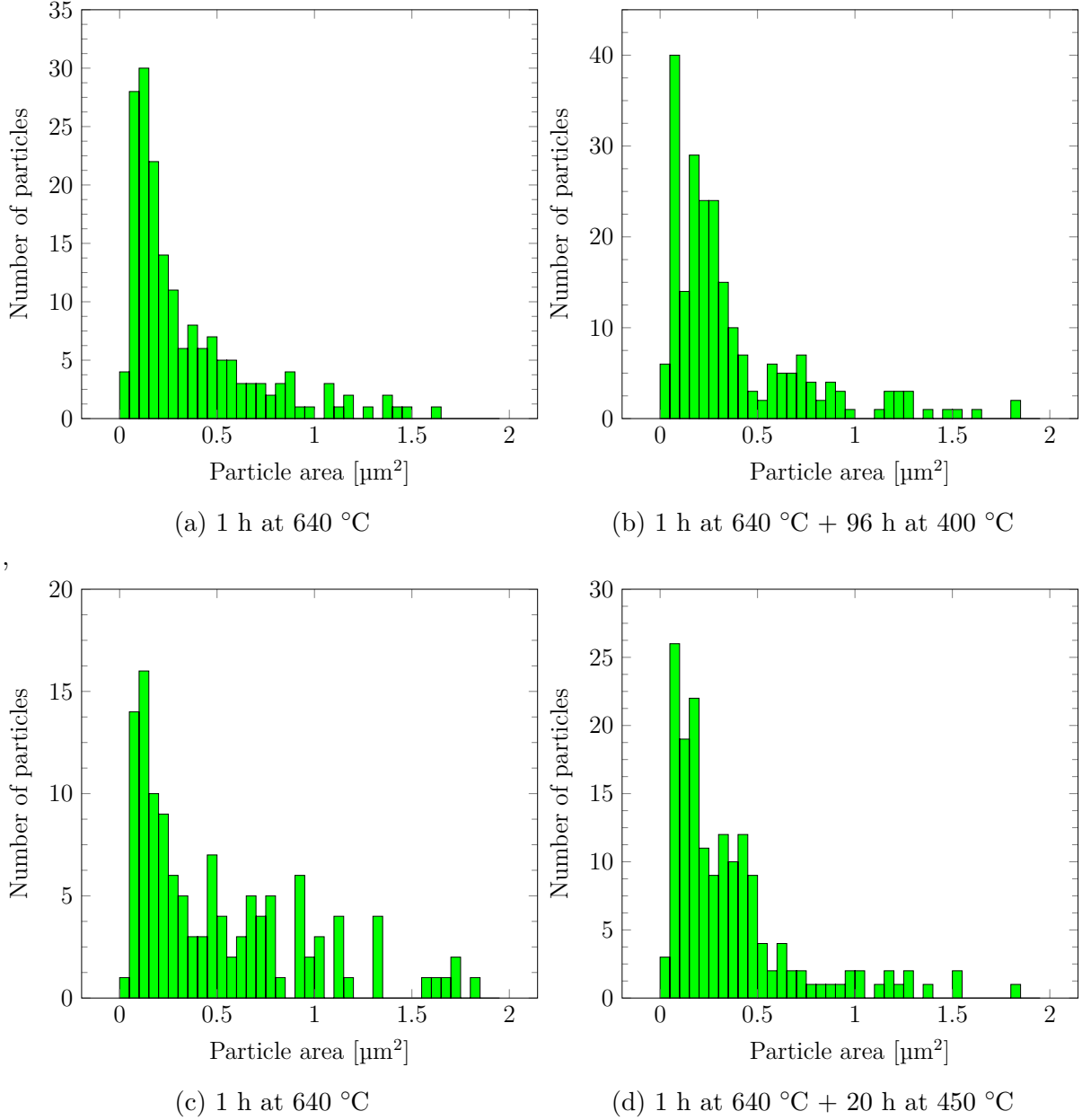


Figure 30: Particle area size distribution of isothermal tempered wires.
Left: After solid solution treatment. Right: After subsequent isothermal tempering.

As told in Section 3.2.2, the particle area distributions were determined by using the SEM software Feature. Two processed images showing the particle distribution in cross-section of tempered wires, are provided in Figure 31. The upper images (a)-(b) represent the wire after solid solution treatment at 640 °C; the lower images (c)-(d) show the wire after subsequent isothermal temper at 400 °C for 96 hours. It was clear that the amount of bright ferrous particles had significantly increased after 96 hours of tempering.

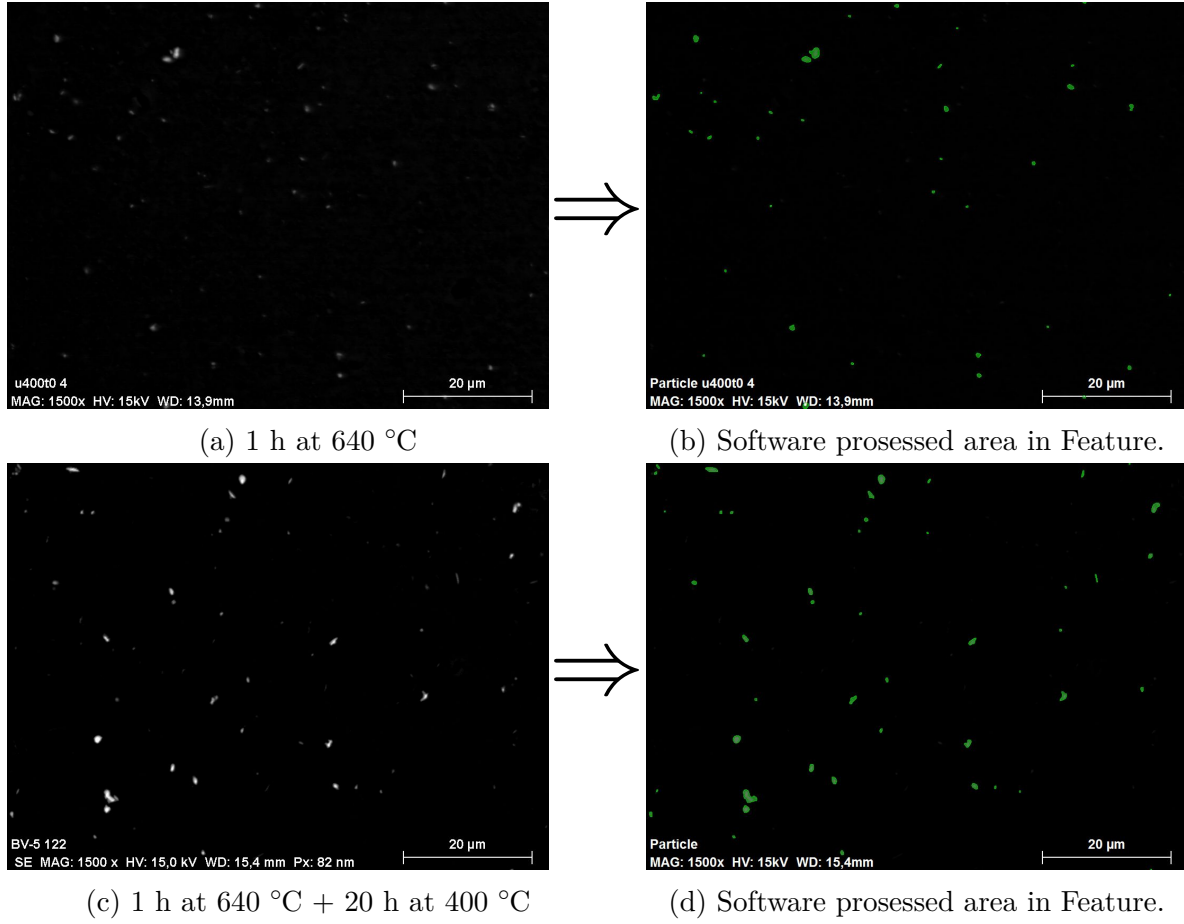


Figure 31: Ferrous particle size distribution of isothermal tempered wires in SEM BSE mode. Images show an increased number of particles after prolonged tempering.

To quantify the evolution of precipitated phases, the area fraction of particles detected by Feature has been calculated for two parallels and presented in Figure 32. Even though the standard deviation was large, there was an unambiguous trend of increasing fraction of particle area during tempering.

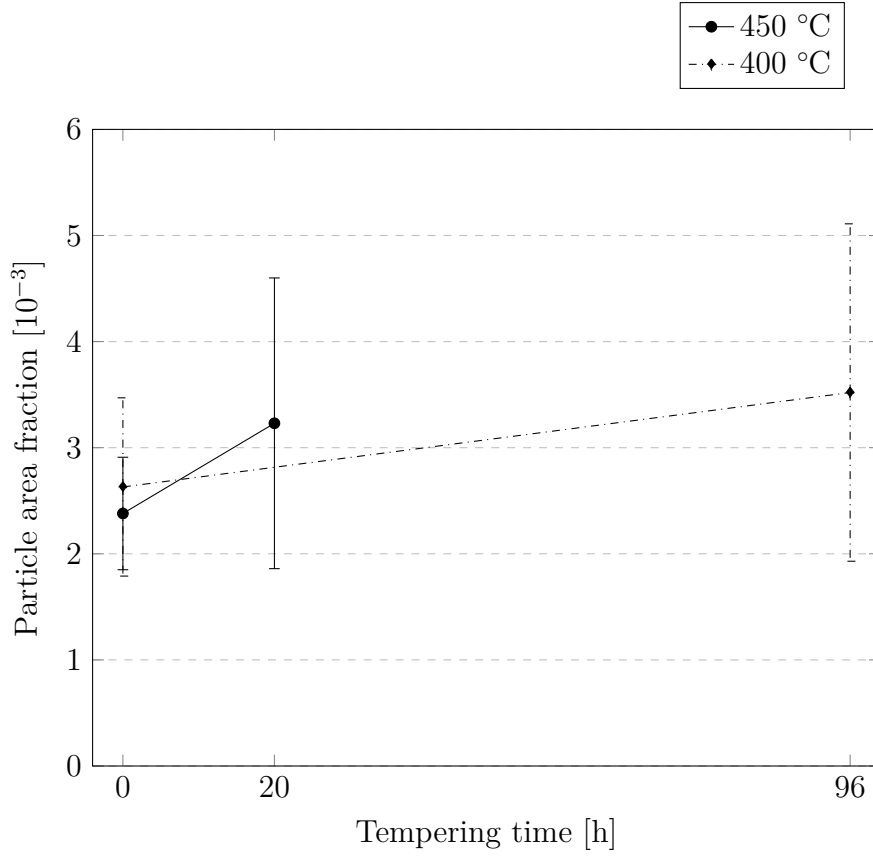


Figure 32: Area fraction of precipitated particles as a function of tempering time.

With clear indications that the amount of precipitated phases increased during tempering, it was desirable to demonstrate the element composition. EDS results of nearly 40 particles are presented in Figure 33. The histograms show the distribution of iron and silicon content in particles after solid solution treatment at 640 °C for 1 hour, and following tempering. For the case of iron in Figure 33 (a)-(b), it was shown an increased iron content in particles after isothermal tempering. For silicon, only one particle contained more than 1 wt% of Si, with an uncertainty of ± 43 wt%. It can with certainty be stated that practically no silicon was detected in examined particles.

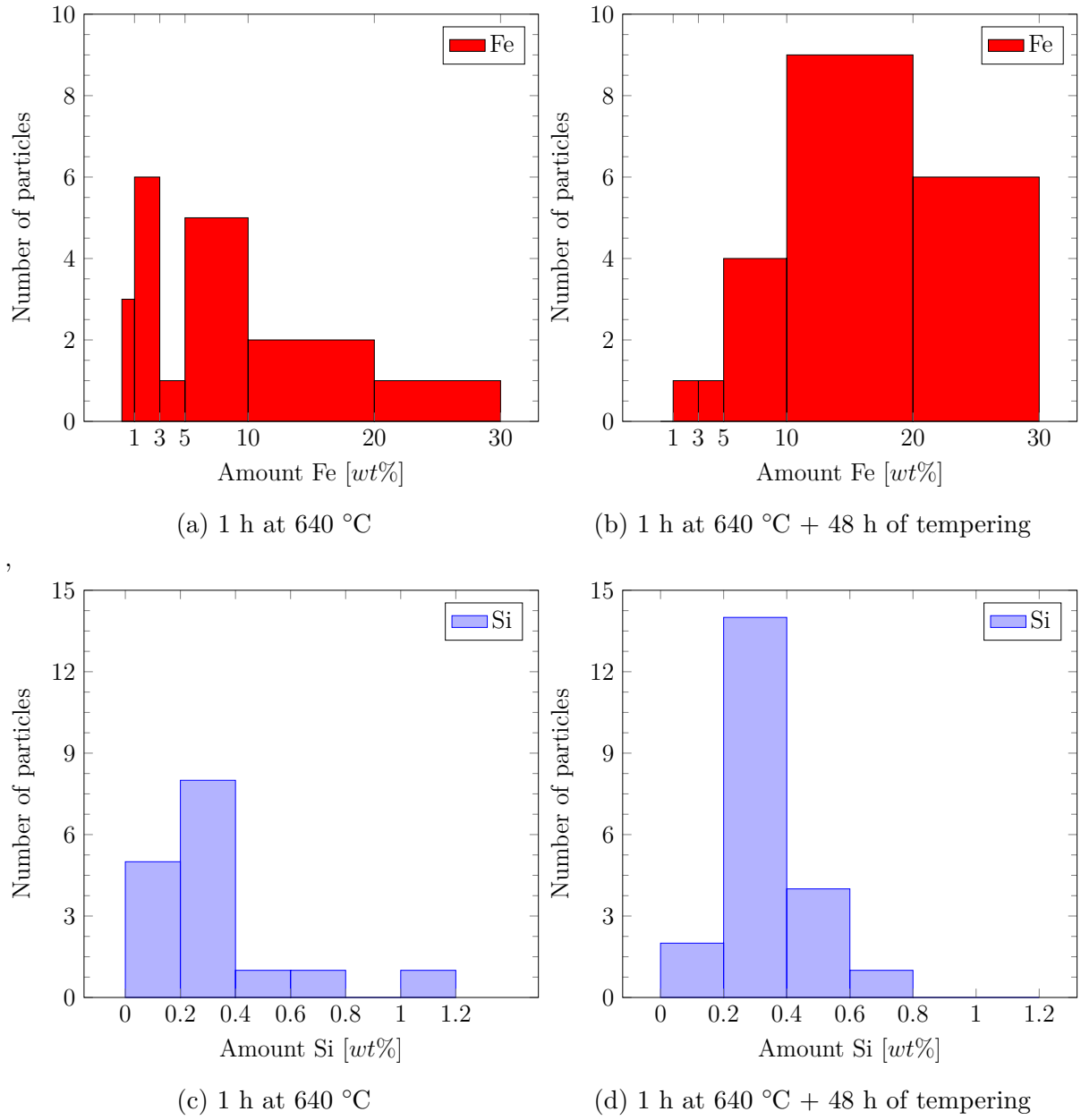


Figure 33: EDS analysis of deposited particles in isothermal tempered wires. Number of particles versus iron content in (a)-(b), silicon content in (c)-(d).

4.3 Screw extruded wire

The following section examines the electrical and mechanical properties, as well as the microstructure, of screw extruded wire made from drawn wire. The effect of tempering was also investigated. The temper was performed at the same temperature as under extrusion, i.e. 450 °C.

4.3.1 Electrical properties

The evolution of electrical conductivity as a function of tempering time is shown in Figure 34. Time = 0 represents the as-extruded wire without any subsequent temper. As tempering time increased, the conductivity slowly decreased. The material did not reach an equilibrium value after 96 hours, so a potential for further conductivity loss was present.

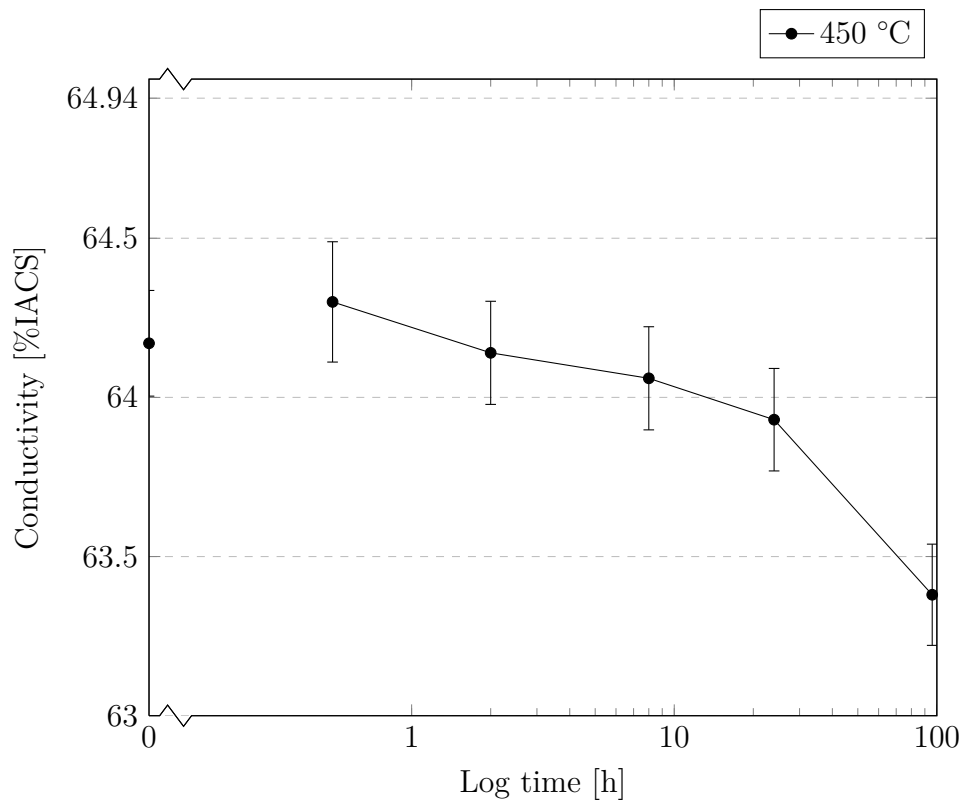


Figure 34: Electrical conductivity evolution with time for screw extruded wire during isothermal temper at 450 °C.

4.3.2 Mechanical properties

The hardness progress during tempering is presented in Figure 35. The plot indicated that the hardness was unaffected by tempering at 450 °C, although the electrical conductivity decreased. Hardness results are tabulated in Appendix C.

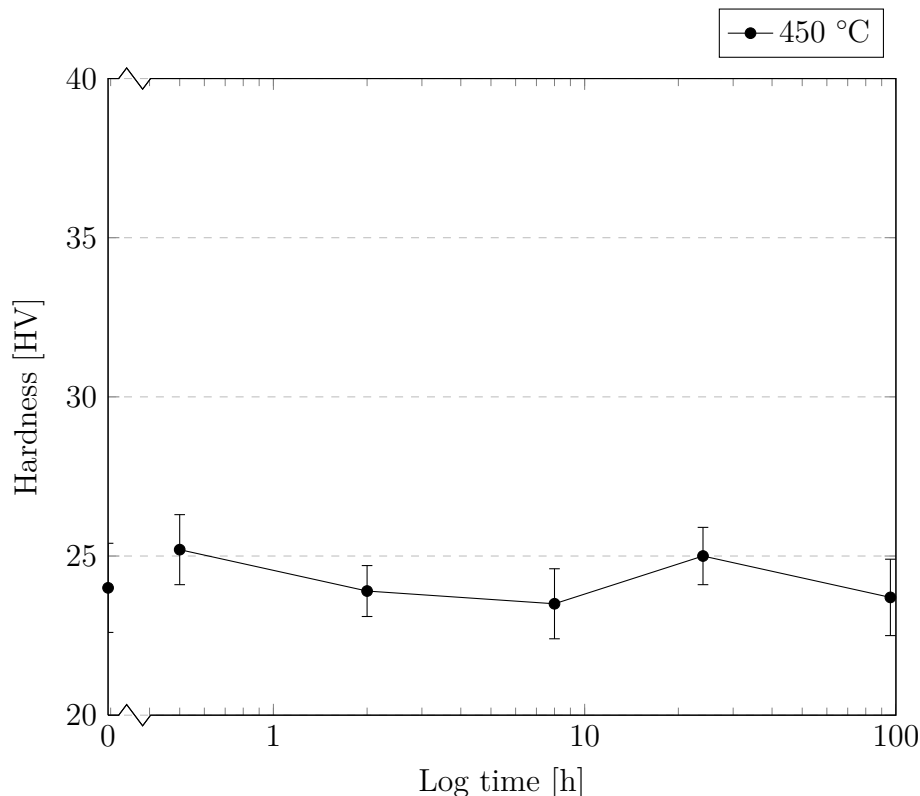
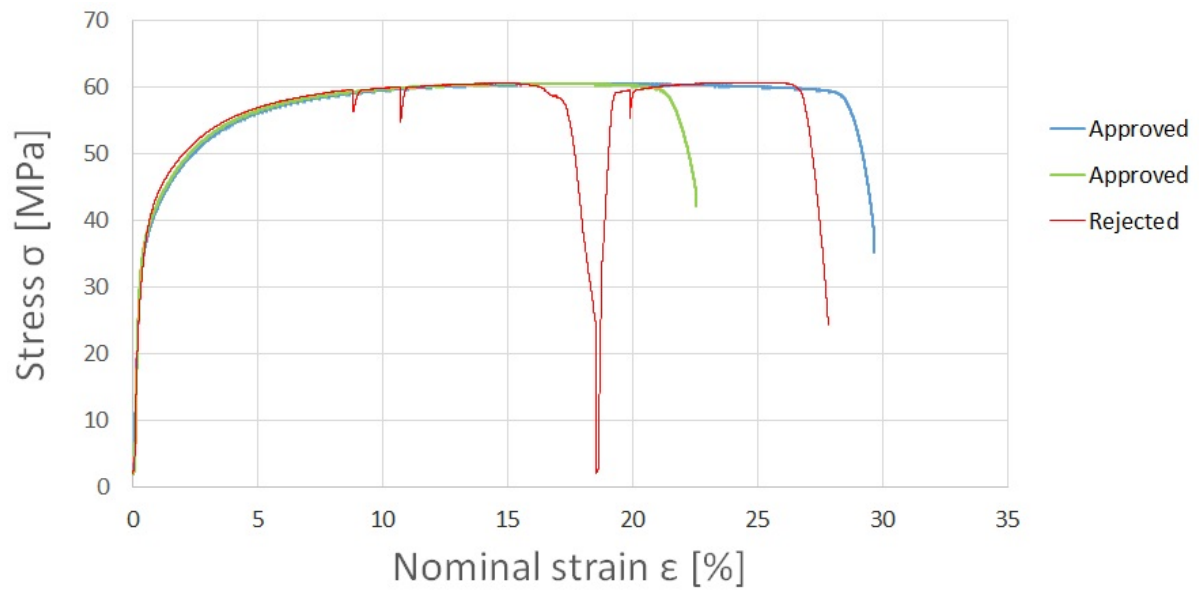


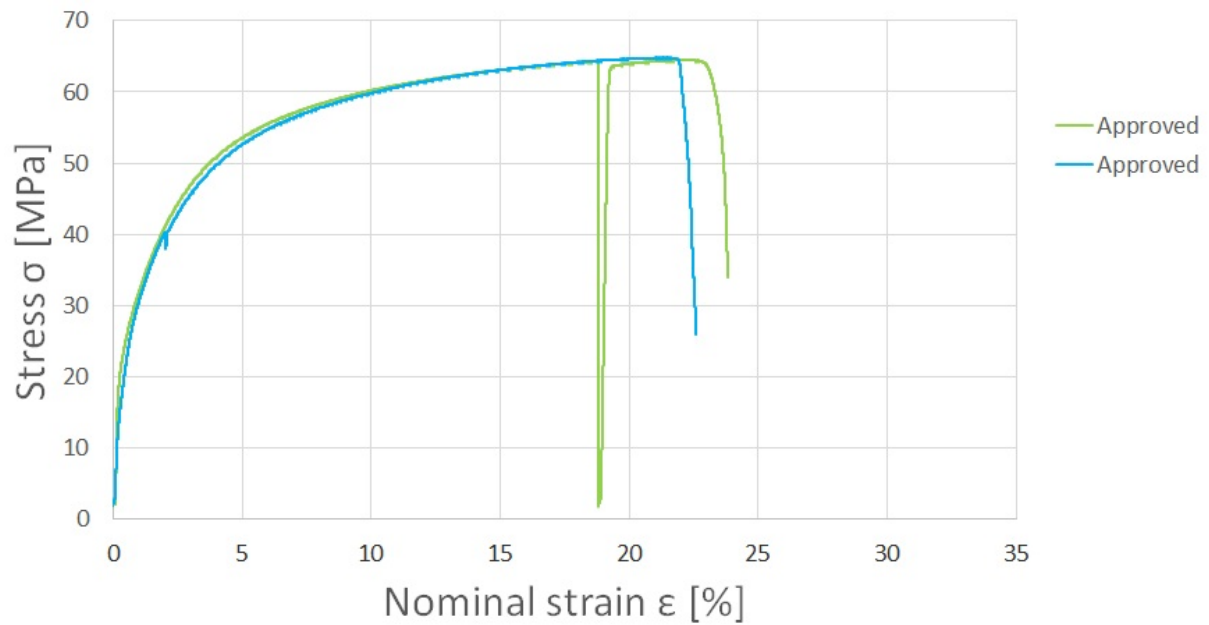
Figure 35: Effect of isothermal tempering at 450 °C on hardness for screw extruded wire.

As the hardness investigations did not show any time dependence, it was necessary to perform tensile testing. Two wires were examined; one at time = 0 (as-screw extruded), and one after 96 hours of tempering at 450 °C. The stress-strain curves are reported in Figure 36, which show quite consistent results for the ultimate tensile strength for both states. This is summarized in Figure 37, along with data on fracture strain. Elongation results showed a large standard deviation, especially for the as-extruded case. While all samples were strained over 20% before fracture occurred, every specimens could be characterized as ductile.

For the as-extruded case, a red curve is shown in the stress-strain plot in Figure 36 (a). This particular sample had probably been prone to slipping in the fastening point, as illustrated by small dips in the stress-strain curve. When the wire completely slips from the copper clamp, the applied force approaches zero at 18% straining. The wire was then fastened and tested again, with the same result of slipping. This specimen was not regarded when determining the tensile strength and elongation. The same procedure was performed with the green curve in Figure 36 (b). For this case, the specimen reached an approved fracture and was accounted for when determining mechanical properties of the tempered wire.



(a) As-extruded wire extruded at 450 °C.



(b) Screw extruded wire tempered for 96 h at 450 °C

Figure 36: Stress-strain curves for screw extruded wires prior and after tempering. Red curve was rejected due to slipping.

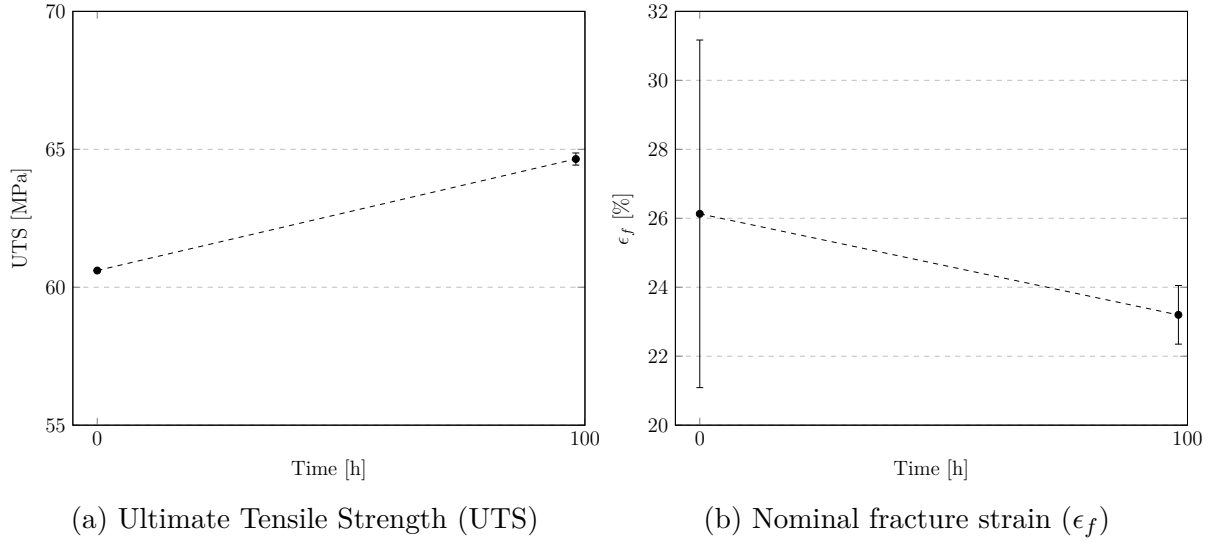


Figure 37: Tensile properties of screw extruded wires as a function of tempering time. Based on approved stress-strain curves in Figure 36.

To correlate mechanical properties to the polycrystalline structure, the Taylor factor distributions of the two examined wires have been determined. The calculations were done on the basis of EBSD results further highlighted in Section 4.3.3, and processed by TSL OIM Analysis 7. It was assumed an aluminium slip system of $\{111\}[\bar{1}10]$ and a deformation gradient \mathbf{F} corresponding to uniaxial tension in extrusion direction. The determination of \mathbf{F} is shown in Equation 10 below. The resulting Taylor factor distribution is shown in Figure 38. For the as-extruded wire, a distinct and narrowly distributed Taylor factor around 2.40 was calculated. After tempering for 96 hours at 450 °C, the Taylor factor distribution was more random, and right-shifted toward higher values. An weighted average of 3.28 was reported for the tempered wire.

$$\mathbf{F} = \begin{bmatrix} \frac{\partial u}{\partial x} & \frac{\partial u}{\partial y} & \frac{\partial u}{\partial z} \\ \frac{\partial v}{\partial x} & \frac{\partial v}{\partial y} & \frac{\partial v}{\partial z} \\ \frac{\partial w}{\partial x} & \frac{\partial w}{\partial y} & \frac{\partial w}{\partial z} \end{bmatrix} = \begin{bmatrix} 1 & 0 & 0 \\ 0 & -0.5 & 0 \\ 0 & 0 & -0.5 \end{bmatrix} \quad (10)$$

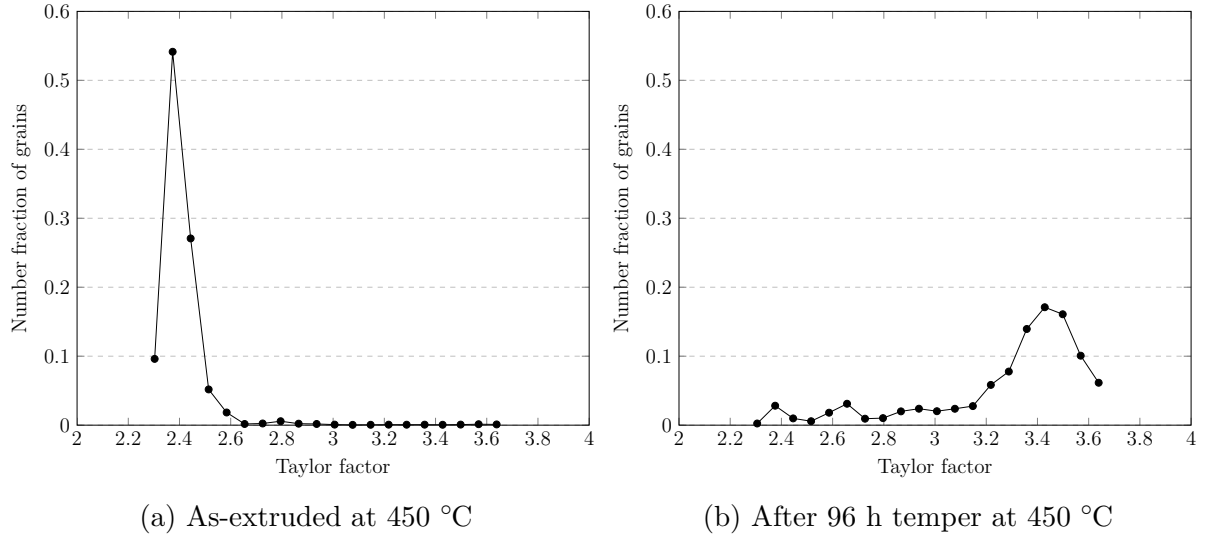
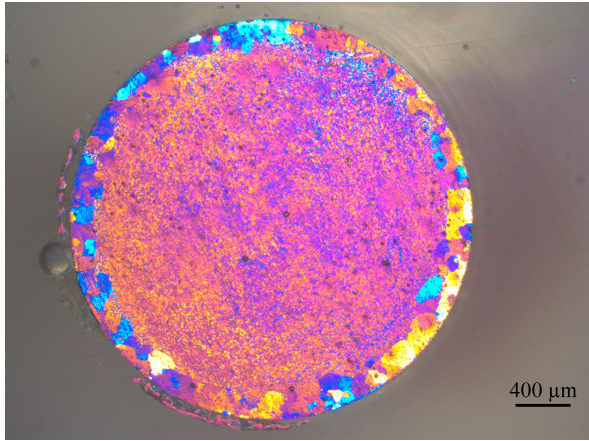


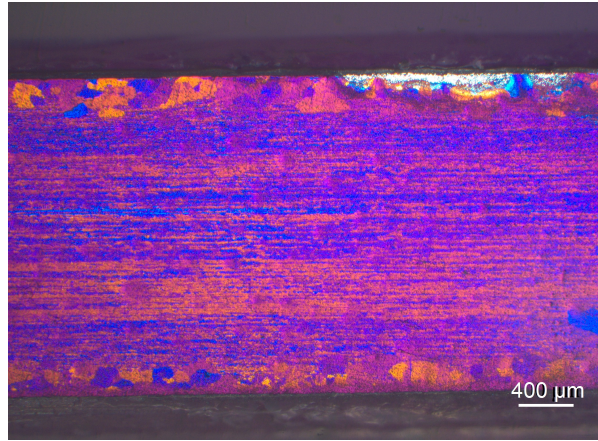
Figure 38: Taylor factor distribution for screw extruded wires examined by EBSD in cross-section.

4.3.3 Grain structure

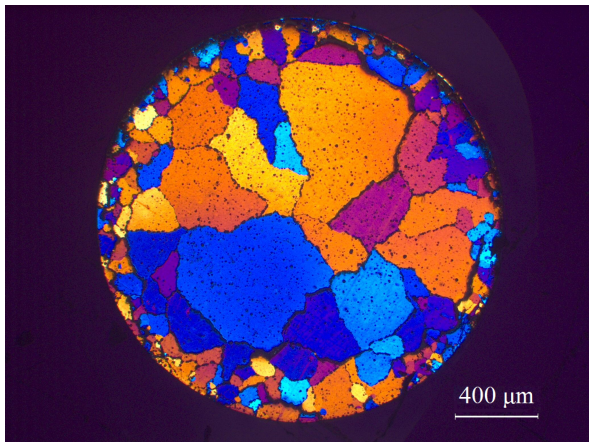
Figure 39 shows micrographs of anodized screw extruded wires, both in cross- and longitudinal section. The upper images (a)-(b) show the wire in its original state after screw extrusion. The lower images (c)-(d) show the same screw extruded wire after 96 hours of tempering at 450 °C. It was evident that the central area had undergone abnormal grain growth during tempering. The grains in the periphery did not grow substantially during tempering.



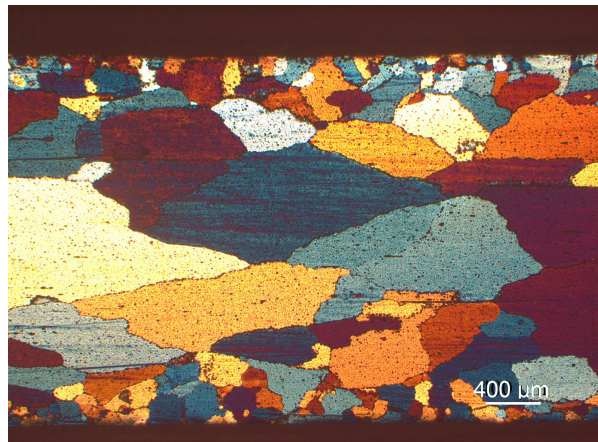
(a) As-screw extruded at 450 °C.
Cross-section.



(b) As-screw extruded at 450 °C.
Longitudinal section.



(c) After 96 h temper at 450 °C.
Cross-section.



(d) After 96 h temper at 450 °C.
Longitudinal section.

Figure 39: Light optical micrographs of anodized screw extruded wires before and after isothermal temper. Magnification 25X.

The as-extruded wire in cross-section shown in Figure 39 (a) exhibited small grains in the center. The lack of a distinct contrast between these grains made it necessary to perform EBSD mapping of the central area. This was also done for the tempered wire, and both results are displayed in Figure 40. The scanning area was based on the structures' grain size. The EBSD scanings are basis for results on the following paragraphs.

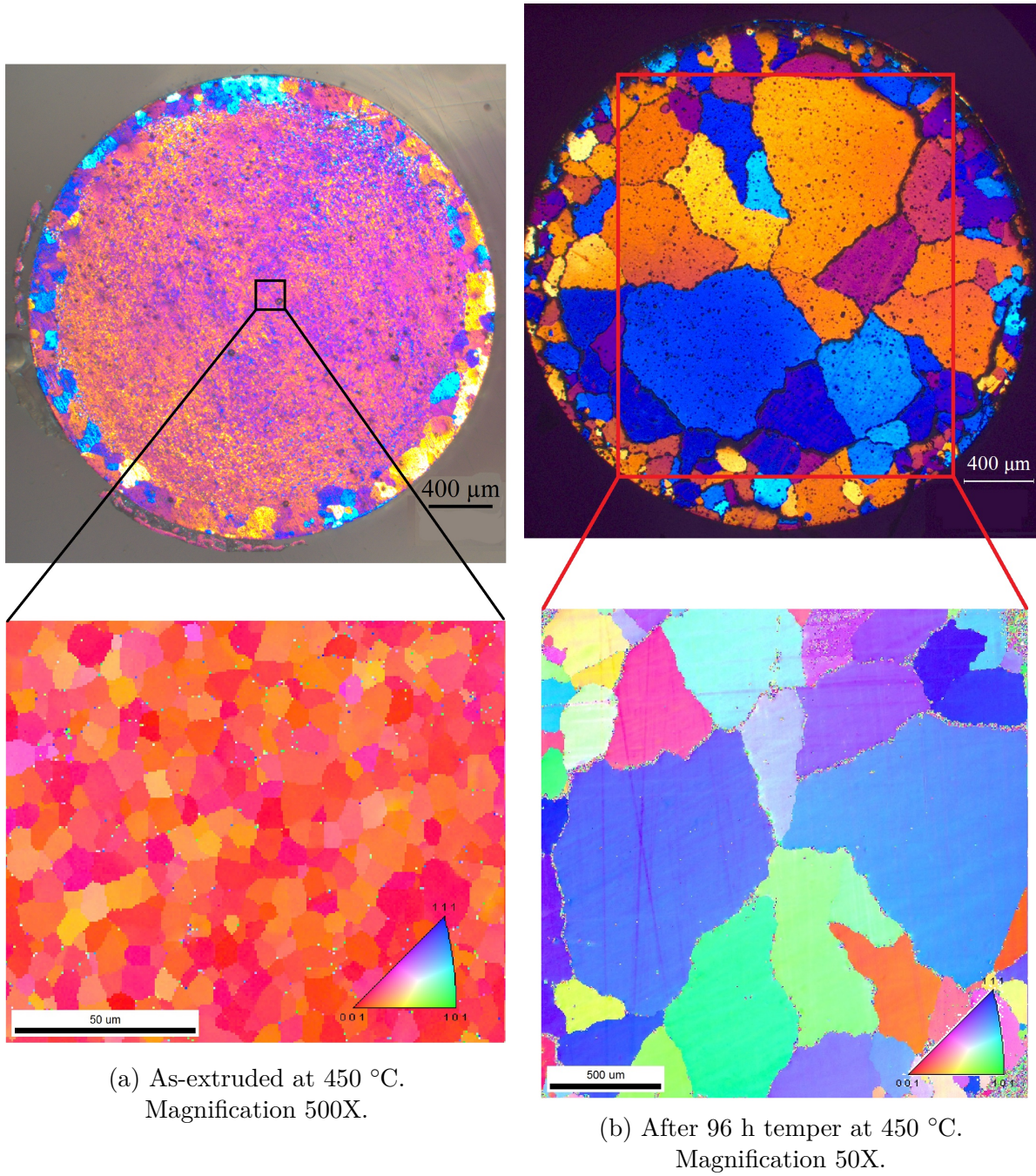


Figure 40: EBSD grain mapping of screw extruded wires in the cross-section. The area investigated is indicated. Please note that the upper micrographs are from light optical microscopy, whereas the lower are from subsequent electropolished samples investigated by EBSD.

The EBSD grain mappings in cross-section were further examined in terms of grain boundaries. The images in Figure 41 (b),(d) show the relative orientation difference between neighbouring grains. Low angle grain boundaries (LAGB) were drawn as red lines, high angle grain boundaries (HAGB) as blue. The as-extruded wire showed a high fraction of LAGB, where over 60% of the grain boundaries had an orientation difference equal or less than 15° relative to its neighbouring grain. After tempering at 450 °C for 96 hours and abnormal grain growth, virtually all LAGB disappeared. Over 90% of detected

boundaries were defined as high-angled, i.e. more than 15° oriental difference between neighbouring grains. Also note that the grain boundaries were several microns wide in the tempered case.

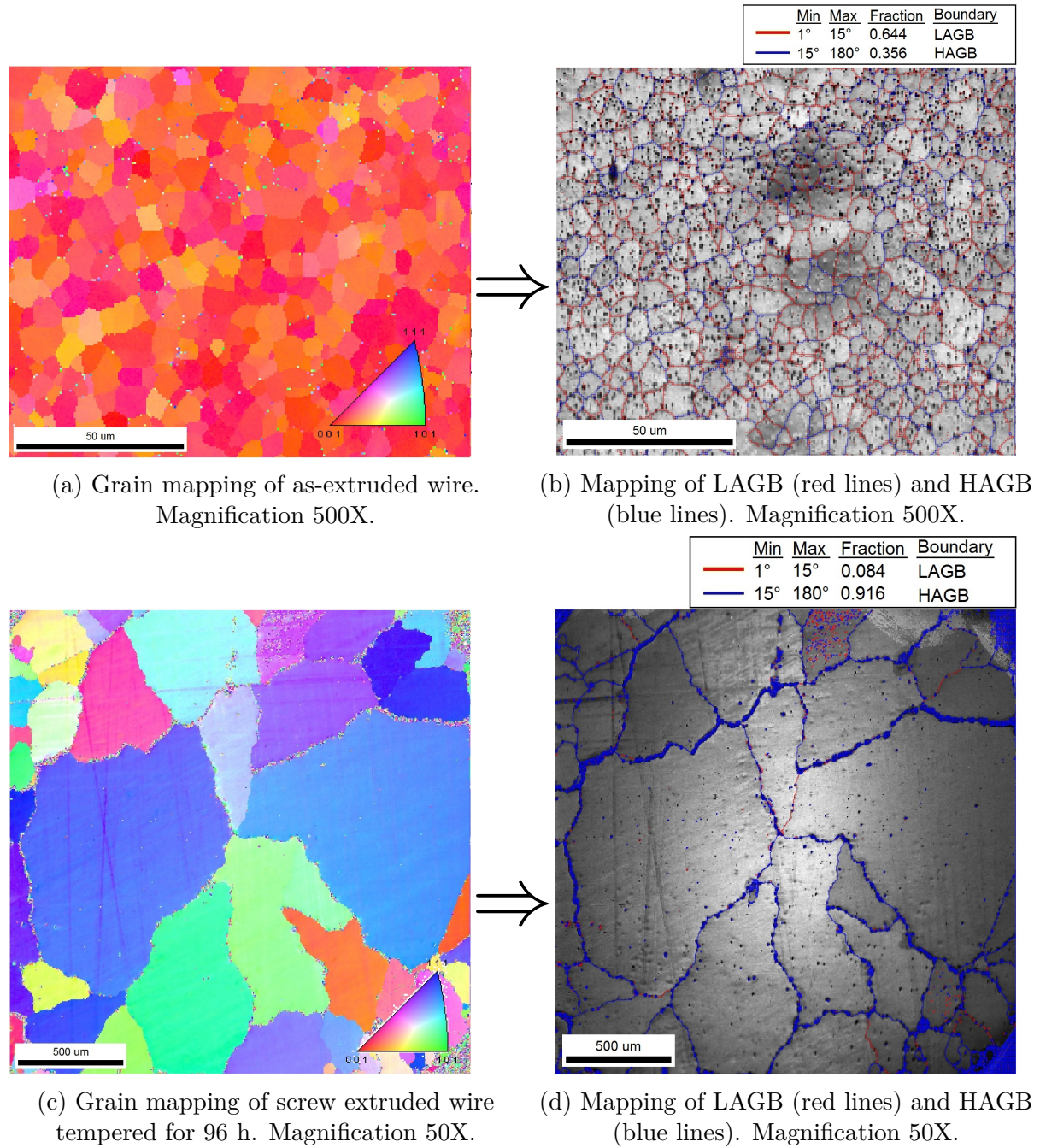


Figure 41: EBSD mapping of low- and high angle grain boundaries (LAGB/HAGB) in screw extruded wires in cross-section.

Based on the EBSD mappings in Figure 40, the grain size distribution for the wires in as-extruded state and after 96 hours tempering at 450°C have been determined. The results are presented in Figure 42. For the as-extruded wire, the grains were normal distributed around its mean at approximately $8\text{ }\mu\text{m}$. The grain size distribution for the tempered wire was, as expected, severely right-shifted. Grains large as $600\text{ }\mu\text{m}$ in diameter were

reported. Just 66 grains were examined in the tempered wire, which made it improper to determine the form of distribution for the grain diameter.

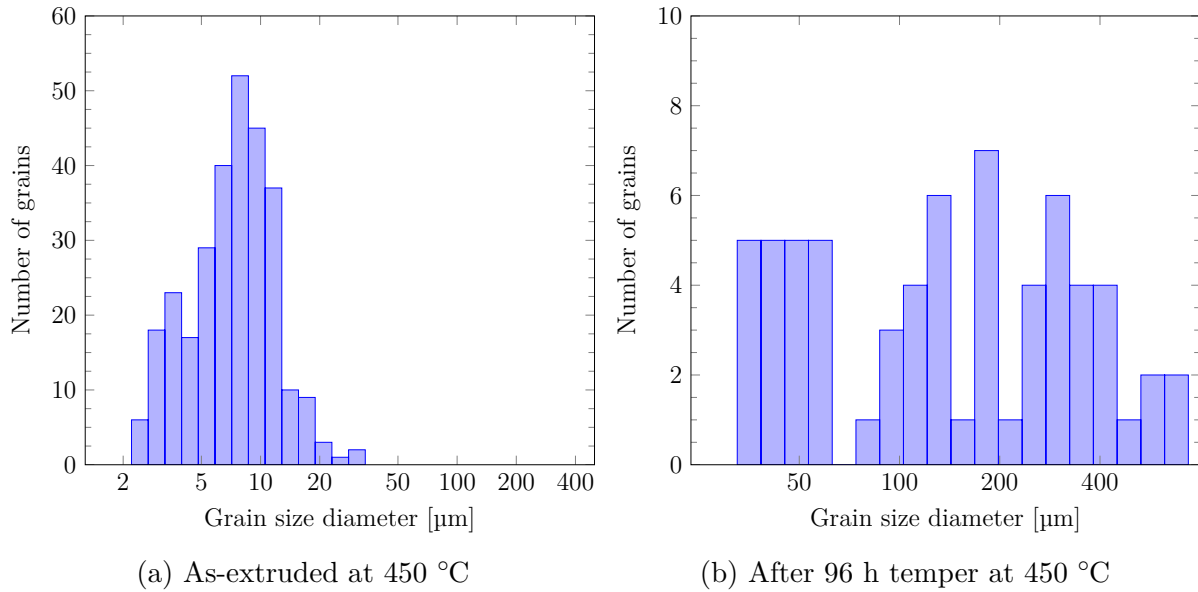
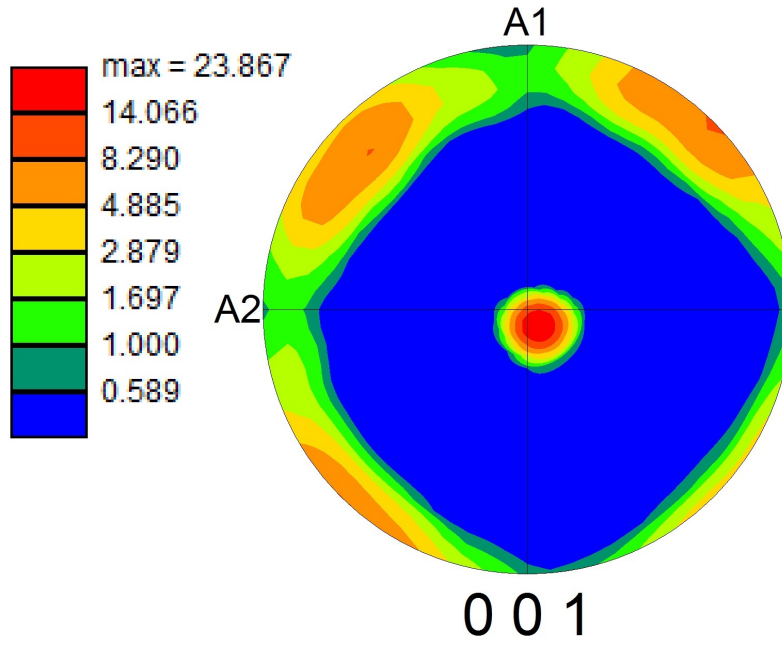
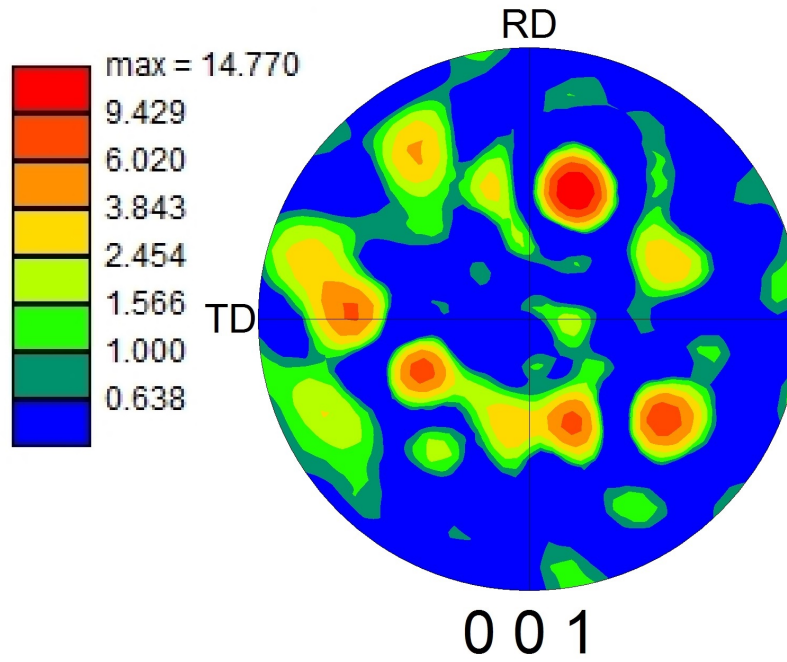


Figure 42: Grain size diameter distributions for screw extruded wires in cross-section. Distributions are based on EDSB grain maps in Figure 40.

Grain textures for the screw extruded wires before and after tempering are highlighted as pole figures projected in $[001]$ direction in Figure 43 (a)-(b). The upper image, representing as-extruded wire, has a strong cube $[001]$ texture. After 96 hours of tempering at 450 °C, the cube texture transformed to a more random character with elements of cube-, R- $\{123\}\langle 634 \rangle$ and B_s $\{011\}\langle 211 \rangle$ textures [46]. As the left-hand scale bars in Figure 43 show, the texture intensity decreased after tempering from approximately 24 to 15.



(a) As-extruded state. Indication of a slightly displaced, but strong cube texture.



(b) After 96 h temper at 450 °C. Random texture with elements of cube, R and B_s components.

Figure 43: Pole figures of screw extruded wires in cross-section projected in $[001]$ direction. Texture intensity is color graded by the left-hand scale bar.

4.3.4 Particle analysis

As-screw extruded wire extruded at 450 °C

When taking the EBSD grain mapping of the as-screw extruded wire into consideration, the grain boundaries are of particular interest. The left image of Figure 44 shows irregular indexing when crossing a grain boundary. Although the indexing failure can originate from the amorphous structure of boundaries, it may imply that nucleation and growth of particles were preferred on this site. The right-hand side image in Figure 44 shows the as-screw extruded specimen in bright field LOM. Black spots represent etching pits as a consequence of electropolishing. Due to the limited depth of field in the EBSD technique, corrosion cavities would not be properly indexed.

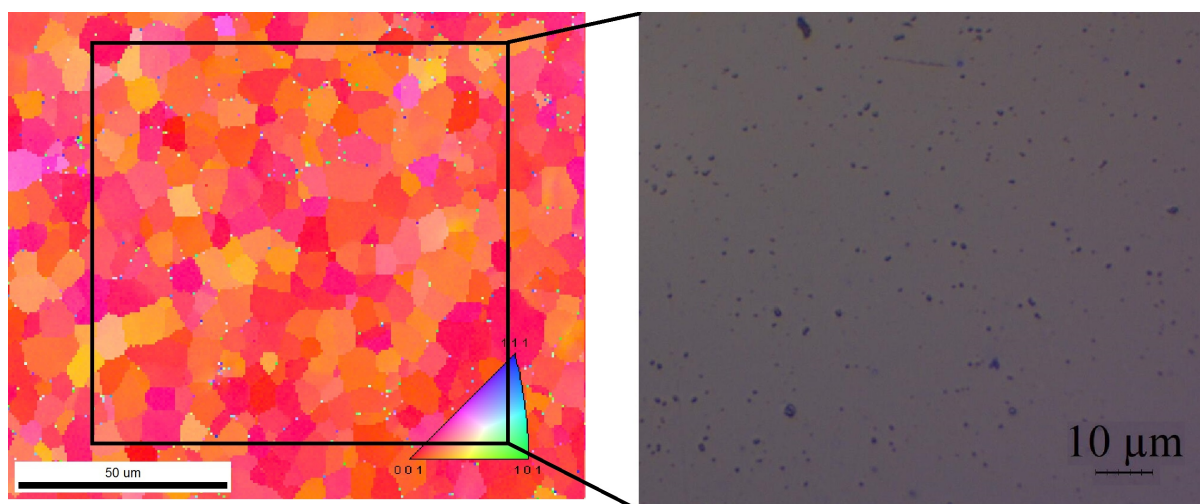


Figure 44: Cross-section of as-screw extruded wire imaged at magnification 500X.
Left: EBSD grain mapping showing irregular indexing over grain boundaries.
Right: LOM micrograph of electropolished surface. Black spots are corrosion pits.

The electropolish procedure involved using a strong ethanol based acid, which possibly resolved particles in the screw extruded material by corrosion. In order to obtain a scratch- and deformation free surface without use of strong etchants, the as-extruded wire was vibration polished for 10 hours. The resulting microstructure is presented in Figure 45 as an SEM backscatter image at 2000X magnification. The grain distinction was possible due to diffraction contrast, while particles were visible as a consequence of Z (element) contrast. As commonly known, heavier elements returns a brighter contrast in backscatter mode. On this basis it was shown by Langelandsvik, autumn 2016, that bright spots consisted of intermetallic phases between aluminium and iron [43]. Now, five darker spots were examined by EDS, as shown in Figure 45. The compositions detected are presented in Table 8, showing a great fraction of oxygen in all particles. The fourth EDS spot detected a small amount of silicon. All EDS spectra are provided in Appendix D.

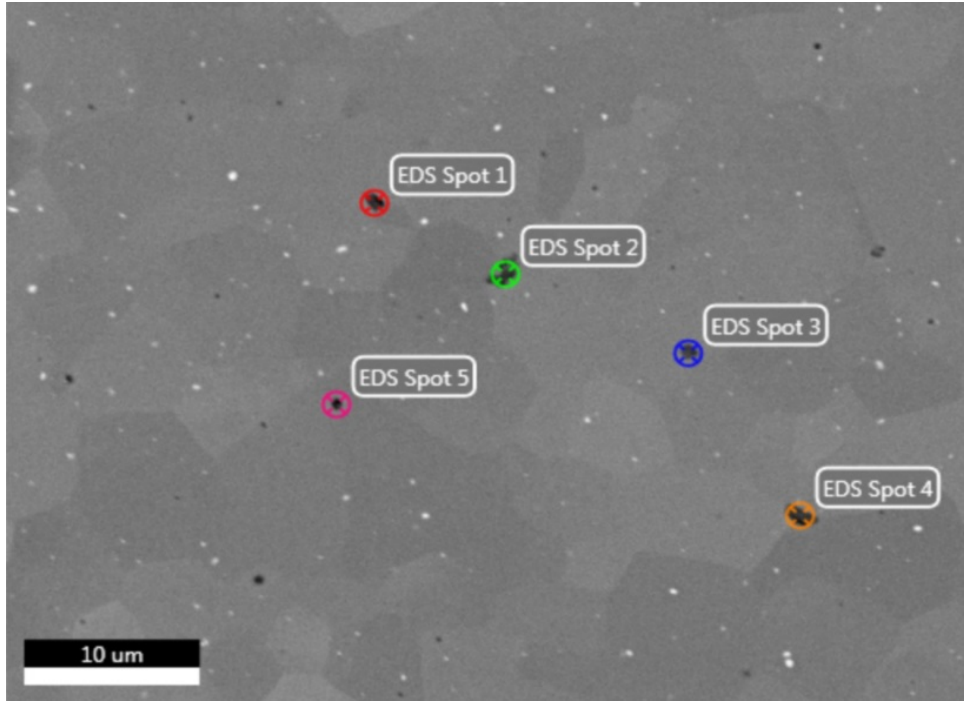
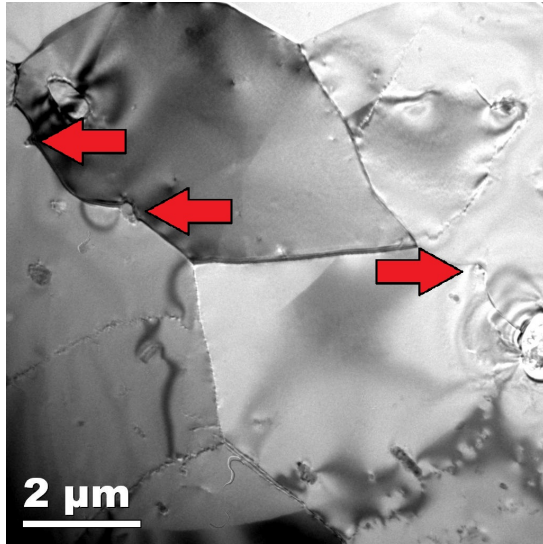


Figure 45: EDS examination of dark particles in as-screw extruded wire in SEM backscatter mode. Magnification 2000X.

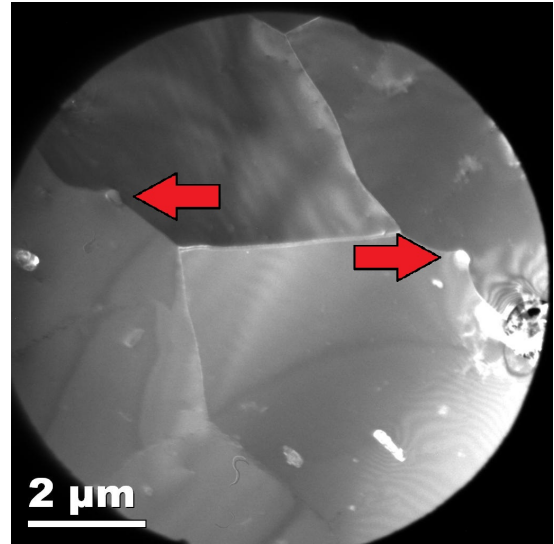
Table 8: Quantitative EDS results of as-screw extruded wire. Based on the EDS spots in Figure 45.

EDS spot #	Element	Content [wt%]	Error [wt%]
1	O	24.08	6.20
1	Al	75.92	2.58
2	O	32.46	5.85
2	Al	67.54	2.73
3	O	21.15	6.32
3	Al	78.85	2.52
4	O	30.33	5.97
4	Al	67.15	2.70
4	Si	2.52	5.66
5	O	3.99	7.39
5	Al	96.01	2.20

To further investigate the Al-Fe intermetallic phases and oxides, longitudinal sections of the as-extruded wire were examined by TEM. An overview at magnification 2000X is presented in Figure 48. Both images were taken from the same area, with bright- and dark field settings. Heavier elements turn bright at low magnification in TEM dark field mode. The bright spots in Figure 46 (b) could therefore consist of iron containing phases. Bright particles which were located at grain boundaries made the boundary bend around the particle, illustrated by red arrows. A more high-magnified bright field image illustrates the effect in Figure 47.



(a) Bright field, 2k magnification



(b) Dark field, 2k magnification

Figure 46: TEM micrographs of as-screw extruded wire in longitudinal section. Red arrows indicate ferrous particles pinning grain boundaries

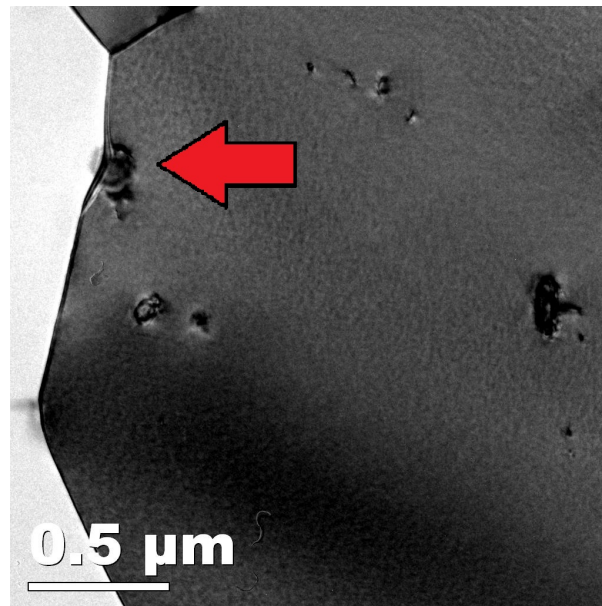
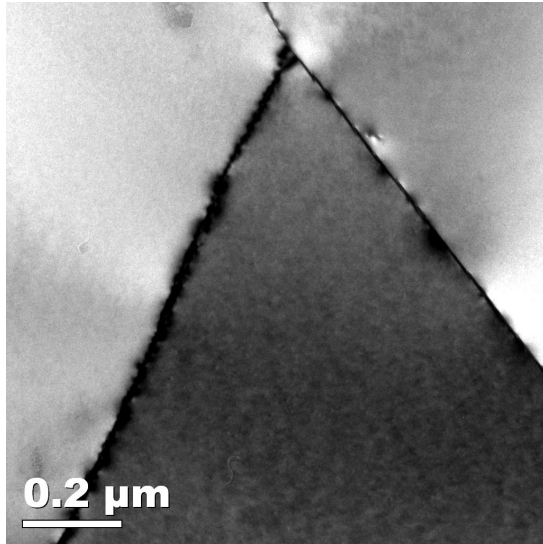
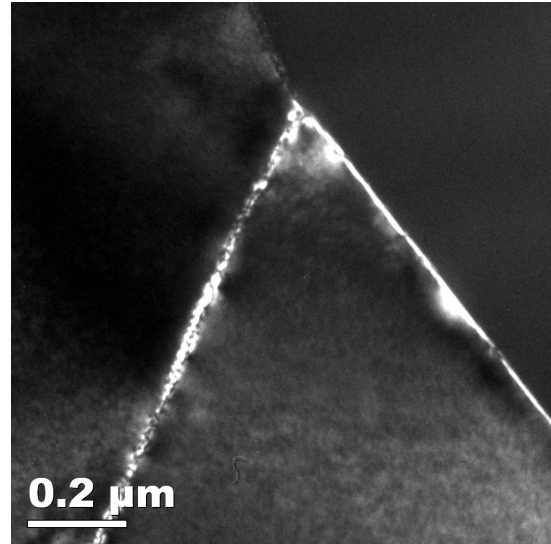


Figure 47: TEM micrograph of as-screw extruded wire in longitudinal section. A particle is pinning the grain boundary (see red arrow). Bright field, 10k magnification.

The TEM images in Figure 48 show a three-point grain boundary in the as-extruded wire, longitudinal section. Images were taken in both bright- and dark field mode. The boundary seems to be decorated by a small particles or other microstructural events. This effect will be further elaborated in the discussion section.



(a) Bright field, 20k magnification



(b) Dark field, 20k magnification

Figure 48: Triple junction boundary with distinct contrast. TEM micrographs of as-screw extruded wire in longitudinal section.

Screw extruded wire tempered for 96 hours

The microstructural effects of prolonged tempering on particles of the screw extruded wire will be explored on the following pages. Results are presented for the screw extruded wire which was tempered for 96 hours at 450 °C.

The electropolished sample mapped by EBSD was imaged in light optical microscope and presented in Figure 49. Both images are in cross-section, showing a characteristic shaped grain. The thick grain boundaries as seen in the left EBSD mapping was due to broad corrosion pits, arose from the electropolishing process. This finding suggests an accumulation of particles at this site, especially at three-point boundaries. As the eventual particles were corroded away, these images could not determine any composition.

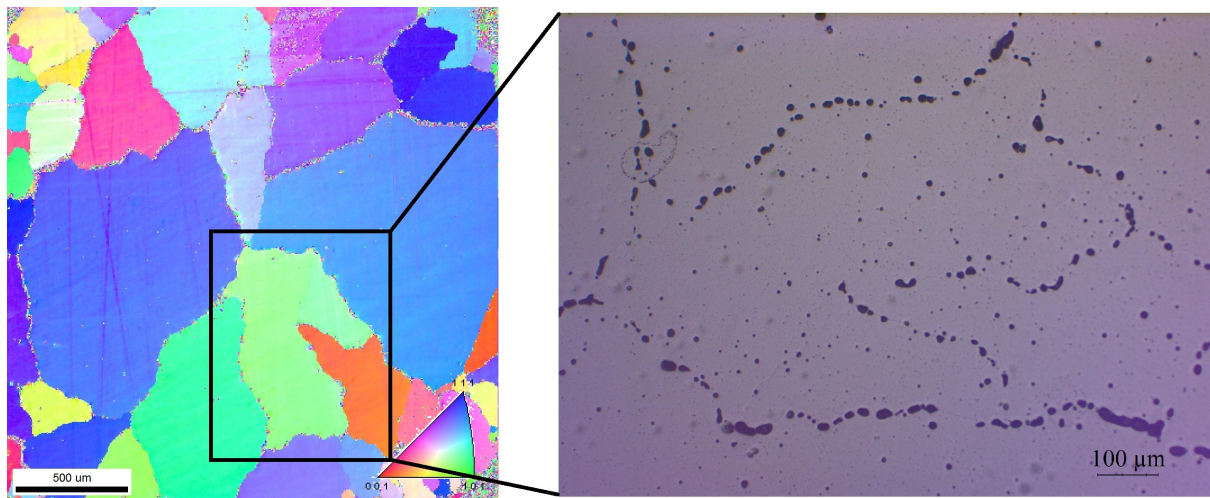


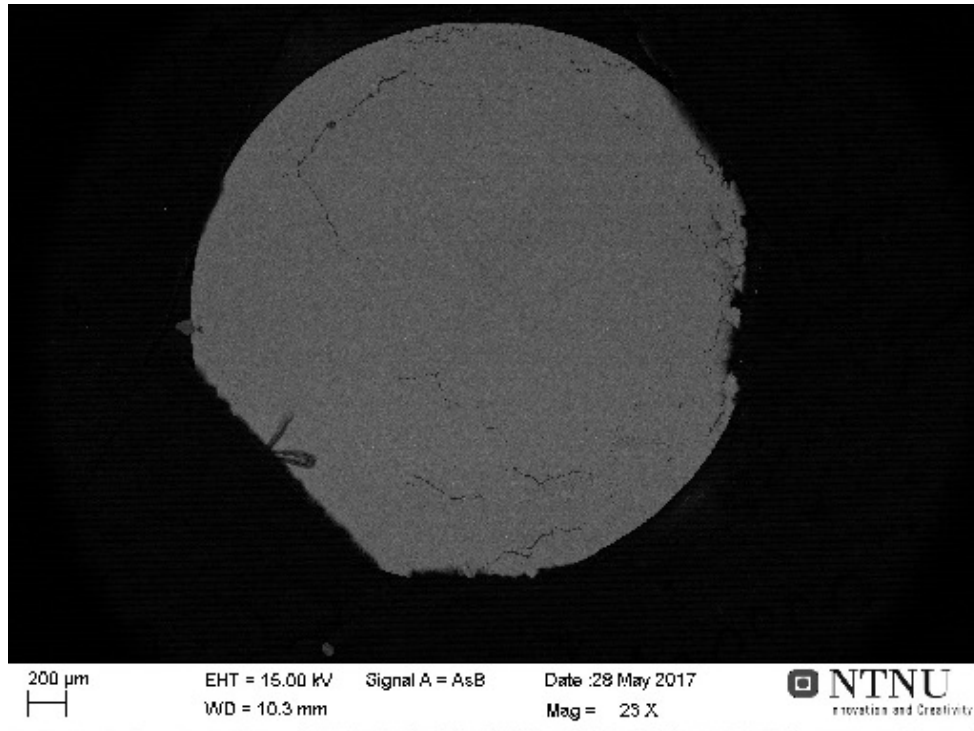
Figure 49: Cross-section of screw extruded wire tempered at 450 °C for 96 h. Left: EBSD grain mapping showing irregular indexing over grain boundaries. Right: LOM micrograph of electropolished surface showing corrosion pits.

In order to maintain the substance surrounding grain boundaries in the tempered wire, a vibration polished sample was examined in SEM backscatter mode. The cross-section at low magnification is shown in Figure 50 (a), where thin black sections are clearly visible. As already shown, the grain size for the tempered material was in the range of 150-600 μm in diameter. Thus, it is likely that the black sections shown in Figure 50 (a) are indeed surrounding grain boundaries.

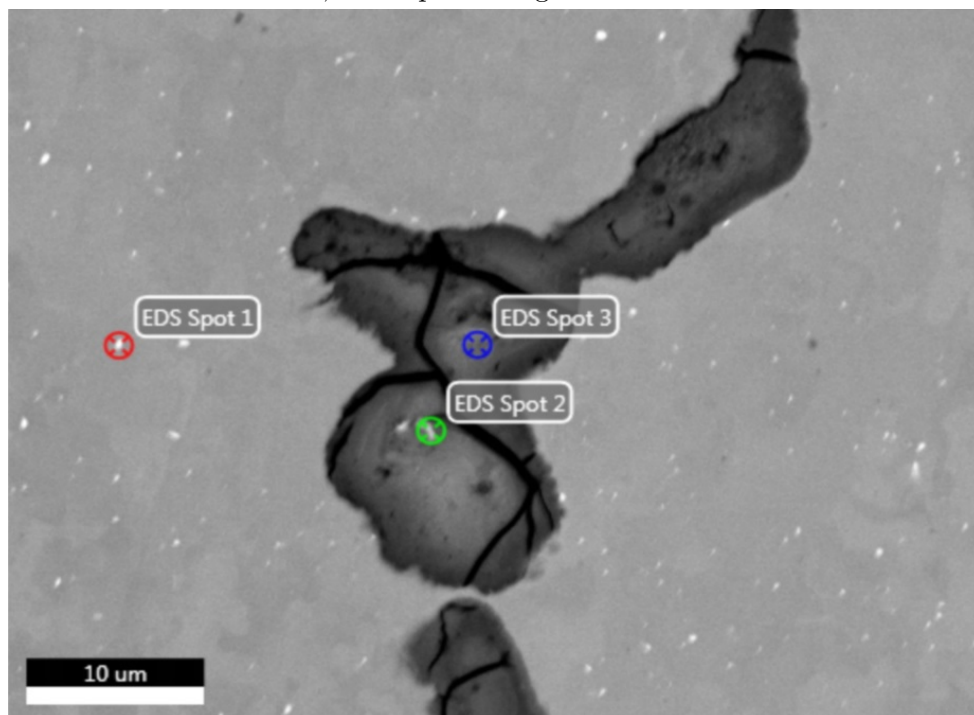
A higher magnified backscatter image of a dark grain boundary section is shown in Figure 50 (b). The dark contrast indicated a lighter element composition than the pure aluminium matrix. Three EDS spots were taken to determine the element composition. The first spot was taken as a reference at a bright, iron-containing particle. The second and third spot examined the dark, boundary particles. The results were summarized in Table 9, in addition to EDS spectra in Appendix D. The EDS analysis confirmed that bright particles contained iron, while the dark particles had a composition consisting of aluminium, oxygen and fluorine.

Table 9: Quantitative EDS results of screw extruded wire tempered for 96 h at 450 °C. Measuring spots are shown in Figure 50 (b).

EDS spot #	Element	Weight %	Error %
1	Al	95.24	2.36
1	Fe	4.76	2.90
2	O	33.65	4.87
2	F	23.93	7.04
2	Al	42.42	3.35
3	O	29.98	4.81
3	F	29.72	6.70
3	Al	40.30	3.43



(a) Overview of electropolished cross-section. Grain boundaries are decorated by small, dark spots. Magnification 23X.



(b) Grain boundary particle with EDS measuring spots. Magnification 2000X.

Figure 50: SEM backscatter images in cross-section of screw extruded wire tempered for 96 hours at 450 °C.

5 Discussion

5.1 Effects of 5 minute temper on drawn wire

As the hardness-conductivity plot in Figure 21 and corresponding microstructures in Figure 24 showed, the as-drawn wire was transformed within minutes during tempering. After five minutes at 450 °C, the cross-section was fully recrystallized. The average grain size at the periphery was 11 μm and increased towards the center to 21 μm . The mobility of grain boundary migration is less attainable towards the wire periphery, i.e. increasing the grain size towards center in all the examined wires in this thesis. Also, one can assume that deformation was higher towards the surface upon the wire drawing process. Thus, the stored energy was higher, giving more nuclei for recrystallization.

Tempering for 5 minutes displayed a sudden shift in hardness and conductivity when increasing the temperature from 350 to 450 °C. The increase in electrical conductivity and corresponding hardness drop is attributed to recrystallization. The drawn wire produced at room temperature has a severely deformed structure, involving a high dislocation density. This imposes a high driving force for recovery and recrystallization, and a rapid microstructural transformation.

Nucleation of new, deformation-free grains sharply diminished the dislocation density in tempered wires. Dislocations yield a strengthening effect, while the dislocation core serves as scattering points for conducting electrons in the crystal lattice. The sudden shift in hardness and conductivity in Figure 21 can thus be attributed to annihilation of dislocations.

When raising the short-temper temperature to 550 °C, the conductivity made a significant drop compared to the case of 450 °C. The explanation may be two-folded; a small increase in grain size decreased the conductivity, which is less likely; or an increased amount of in-quenched iron was present in solid solution after quenching from 550 °C, which seems more feasible.

5.2 Isothermal temper of drawn wire

5.2.1 Precipitation mechanisms

To investigate precipitation mechanisms and related kinetics in commercial pure aluminium, the drawn wire received a solid solution treatment at 640 °C for one hour followed by water quenching. It was assumed that the process supersaturated the material with iron in solid solution up to 0.052 *wt%*, as predicted by the binary Al-Fe phase diagram [11]. The quenching could also introduce a large number of single vacancies (Schottky defects) in the structure.

As shown in Figure 25, the electrical conductivity of solid solution treated wires increased as a consequence of subsequent isothermal tempering in the range of 300-560 °C. Both the grain size and dislocation density was shown to be quite constant throughout the tempering, Figure 29. Thus, contributions for increasing the conductivity are believed to consist of vacancy redistribution and iron precipitation.

Schottky defects are highly mobile in commercial pure aluminum. If the material was stored for several days, the defects could be annihilated out at room temperature [47]. No specimens with potential in-quenched vacancies were stored longer than three hours at room temperature in this thesis. If Schottky defects were present in the material after solid solution treatment at 640 °C, they should not be annihilated prior to isothermal tempering.

At elevated temperatures, the redistribution of vacancies was believed to happen rapidly, yielding a sudden increase in conductivity. This was not seen from the curves in Figure 25. A lack of conductivity enhancement may arise from the fact that isothermal tempered wires also were cooled by water quenching. This may introduce new Schottky defects, yielding the approximate same state as solid solution treated wire in terms of vacancies. It is hence two possible explanation; a rather constant number of vacancies in all examined wires, or that Schottky defects play a minor role governing conductivity in aluminium.

Figure 31 and 32 unambiguously showed an increasing amount of precipitated particles as a consequence of isothermal tempering. The particles consisted of Al-Fe intermetallic phases, confirmed by EDS analyzes in Figure 33. The conductivity evolution shown in tempered wires are hence explained by deposition of iron out of solid solution.

Tempering of wires in the range of 400-500 °C yielded the best electrical properties which could be attributed to the driving force for precipitation of ferrous intermetallic particles. When the balance of driving force and diffusion is optimized, the process starts at shorter tempering times. This is summarized in a time-temperature-transformation (TTT)-diagram, presented in Figure 51. The assessment was based on the conductivity-time curves in Figure 25. It was assumed that precipitation of iron started when the conductivity increase initiated. After prolonged tempering, the conductivity curve flattened out, indicating end of precipitation. With 0.058 wt% Si present in the material, the silicon could affect the precipitation mechanisms. The total number of Al-Fe-Si deposits were believed to be minor compared to Al-Fe phases. The contribution of silicon to precipitation was therefore considered to be limited.

The TTT nose peaked at 450 °C, where precipitation began after approximately one minute. As an effect of this, the precipitation ended rather quickly, after 20 hours. At 400 °C, precipitation was not completed after four days of tempering. This was explained by the non-existing solid solubility of iron and the sluggish diffusion at 400 °C.

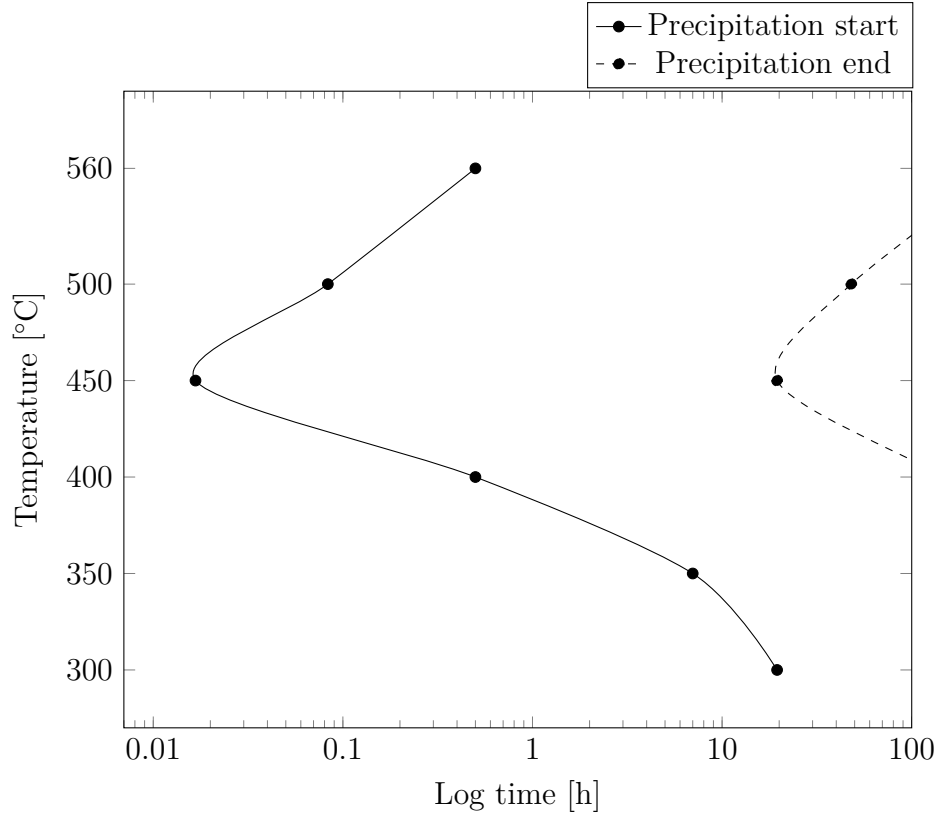


Figure 51: TTT-diagram showing start and end of precipitation of ferrous intermetallic phases during isothermal tempering. Specimens were solid solution treated at 640 °C for 1 hour prior to tempering.

The highest value of electrical conductivity was obtained by tempering the solid solution treated wire at 400 °C for 96 hours, Figure 25. The particular sample rose from an initial value of 62.13 %IACS after solid solution treatment to achieving a peak conductivity equal 64.50 %IACS. If assuming all alloying elements being solved in the aluminium matrix after solid solution treatment at 640 °C, it can be modelled the amount of remaining iron in solid solution after isothermal tempering. This has been done for the three predictions by Lok, Kutner and Karabay presented in Section 2.6.3 [32–34]. The results are plotted in Figure 52. The model of Lok (black, solid line) assumed all manganese and silicon in solid solution, while the two other also took titanium and vanadium into consideration.

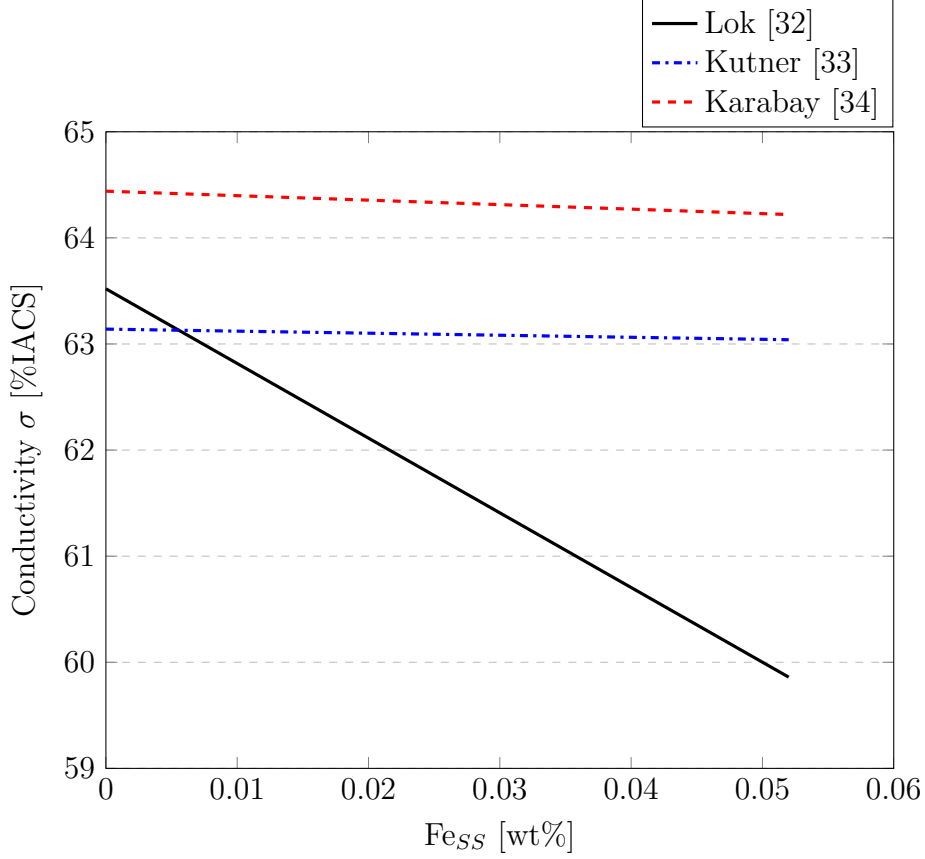


Figure 52: Theoretical models of the effect of iron in solid solution on electrical conductivity. Plot based on [32–34].

If assuming the conductivity ranging from 62.00 to 64.50 %IACS as a consequence of iron deposition, it was clear that both Kutner and Karabay undershot the effect of iron in solid solution (red and blue dotted line). Lok, on the other side, accounted for the effect of iron, but underestimated its intercept at 0 wt% of iron in solid solution, Fe_{SS} . Its intercept given in Equation 9 represented an intrinsic conductivity of ultra pure aluminium equal 64.57 %IACS. As stated in Section 2.7, the vertex should be 64.94 %IACS. The prediction given by Lok was therefore modified with a new intercept value corresponding the conductivity of ultra pure aluminium, and presented in Equation 11.

Equation 11 accounted only for the contributions of iron, manganese and silicon in solid solution ($Fe_{SS}\%$, $Mn_{SS}\%$ and $Si_{SS}\%$). Other elements like vanadium and titanium were not included in the model. Another limitation of the model was the assumption that electrical conductivity was independent of precipitated atoms, which is not the fact. As described by Olafsson, precipitates do contribute to the resulting conductivity [37].

$$\frac{1}{\sigma} = 0.0265 + 0.036Mn_{SS}\% + 0.032Fe_{SS}\% + 0.0068Si_{SS}\% \quad (11)$$

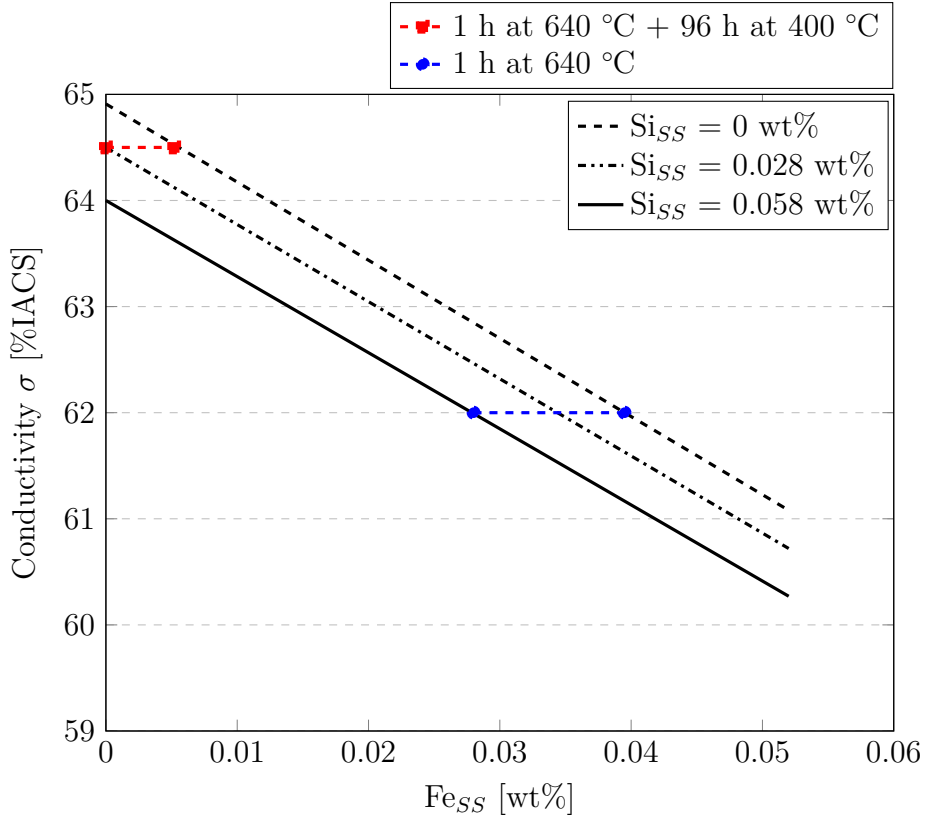


Figure 53: Modified Lok model predicting the effect of iron and silicon in solid solution. Plots based on Equation 11.

A graphical representation of the modified Lok equation was presented in Figure 53. It was assumed that all manganese was present in solid solution (0.001 wt%, Table 3). Three curves were drawn in Figure 53, each representing a constant amount of silicon in solid solution. The solid line denoted all present silicon to be in solid solution ($\text{Si}_{SS}\% = 0.058 \text{ wt}\%$), resulting in a maximum conductivity of 64.00 %IACS.

The wire tempered for 96 hours at 400 °C reached a conductivity equal 64.50 %IACS, plotted as a horizontal red line in Figure 53 (---). This value exceeded the maximum conductivity reached when assuming all silicon in solid solution. Thus, it is possible that a fraction of silicon had been forced out of solid solution. An iron-silicon relation in solid solution after 96 hours of tempering at 400 °C was hence present, lying on the red line. If every iron atom was forced out of solid solution, 0.028 wt% silicon are left in solid solution. Conversely, if all silicon was precipitated out, 0.005 wt% of iron could potentially be left in solid solution.

The plot in Figure 53 gave an indication of the degree of supersaturation of iron after solid solution treatment at 640 °C for 1 hour and following quenching. This was designated as a blue horizontal line at 62.00 %IACS (---). Dependent on the amount of silicon in solid solution, 0.03 to 0.04 wt% of iron was potentially locked in solid solution as a consequence of quenching.

EDS results cited in Figure 33 did not detect any significant amount of silicon in 39 examined particles. The ternary Al-Fe-Si phase diagram in Figure 5 supports this finding, based on the present silicon content. Nevertheless, a limited EDS sample and the pos-

sibility of examining the densest (thus, brightest) particles may explain why no silicon was detected in precipitated state. EDS results in Figure 33 are then considered to not be strong enough evidence to reject the claim of silicon in precipitated state.

5.2.2 Mechanical properties

The hardness measurements of isothermal tempered wires exhibited no significant evolution as a function of time. The materials were also extremely soft, yielding deep measuring indentations in the surface. At the surface, indentations were approximately 300 μm in diameter. If a hardness indentation approaches the grain size of the material, the grain boundary constraints the Vickers diamond tip. As a consequence, the hardness increases erroneously. This probably happened with the wire tempered for 96 hours at 500 $^{\circ}\text{C}$ in Figure 26, which exceeded 30 HV.

16 specimens of selected isothermal tempered wires were tensile tested and presented in Figure 27. All specimens experienced premature fracture without any significant degree of necking. This may arise from several factors. First, the initial treatment at 640 $^{\circ}\text{C}$ for one hour resulted in a severe grain growth. Grain sizes exceeding 300 μm in diameter are reported, Figure 29 (a)-(b). Large grains are prone to rapid crack growth, as the crack propagates without frequent change of slip system across grain boundaries. At the same time, a soft commercial pure aluminium alloy blunts growing cracks by work hardening to a high degree.

Second, the specimens for measuring conductivity and tensile properties were the same piece of material. This was done to ensure a consistent conductivity-strength relation of the examined wires. As described in Section 3.4, wires were grounded with coarse sandpaper prior to measuring conductivity. Scratches introduced from this preparation stage may serve as stress concentration points during tensile testing.

Nevertheless, the performed measures to determine mechanical properties of isothermal tempered wires yielded too unreliable results to conclude any strength related trends during isothermal temper.

5.3 Screw extruded wire

5.3.1 Mechanical properties

Tensile testing performed for the screw extruded wires before and after tempering resulted in consistent values for the ultimate tensile strength (UTS). The ductility was not determined with certainty, as the standard deviation was very high. The uncertainty arose from the use of laser extensometer, which was dependent of observing the concentrated plastic deformation prior to fracture. The laser covered 2-3 cm of the tensile specimen, while the specimen itself was about 10 cm long. The chance of not recording necking was hence likely, which produced uncertain straining results.

Screw extruded wires did not experience premature fracture during tensile testing. Unlike the isothermal tempered tensile specimens covered in Section 5.2.2, the screw extruded tensile specimens were not grounded with sand paper prior to testing. Hence, it is likely that sand paper grinding is detrimental for examining tensile wire bars.

The UTS of screw extruded wires increased by 4 MPa after 96 hours of tempering at 450 °C. The enhancement can be attributed to texture transformation from a strong cube component to a rather random texture. The cube texture yielded a low Taylor factor, a weighted average value equal 2.40. A lower value of Taylor factor means that macroscopic deformation requires a small slip shear stress to proceed deformation [48]. When the average Taylor factor value increased after tempering for 96 hours at 450 °C to an average equal 3.28, the strength also increased.

The average grain size changed during temper. As the grain size distributions in Figure 42 illustrated, prolonged tempering at 450 °C induced an intense grain growth. As mentioned, a large grain size was not favourable in terms of mechanical properties. To summarize, the resulting UTS of tempered screw extruded wires were governed by two factors which approximately cancelled each other out; strength gain through a favourable texture, and strength loss due to increased average grain size.

5.3.2 Microstructural evolution during screw extrusion

To assess the relation between microstructure and electrical conductivity of screw extruded wires, it is paramount to understand the evolution from granulated feedstock to final extrudate. The untempered drawn wire was used as feedstock for extrusion. The feedstock was thermally treated at 350 °C for 30 minutes prior to extrusion, Section 3.1.2. A corresponding time-temperature combination was sufficient to recrystallize the material. The material fed into the screw extruder is therefore believed to be rather soft.

When the freshly recrystallized granulates were transported forward by the screw in the extrusion chamber, it started compressing. The compression of granulates to a solid plug represented a high degree of deformation. Simultaneously, frictional forces and external heating tempered the material. It is probable that the material inside the extrusion chamber was exposed to a series of repeated deformations and recrystallizations, as shown in Figure 54. When the solid plug was extruded through the die as a wire, all deformations ceased to exist, and the material initiated an (eventual) grain growth. To inhibit this growth, the wire needed to be quenched as soon as it left the die.

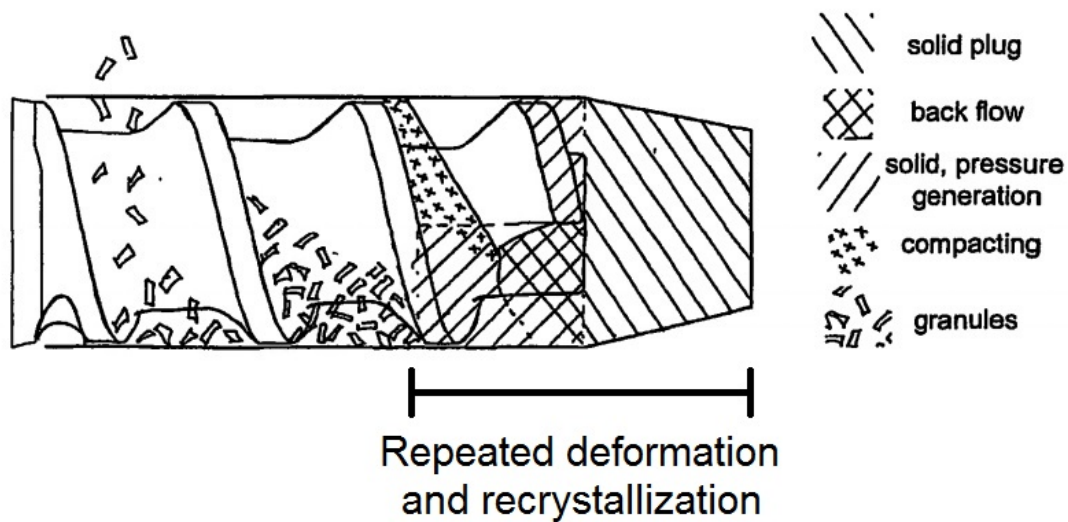


Figure 54: Sketch of screw extrusion chamber, indicating the area of iterative deformation and recrystallization of granulated feedstock. Modified figure from [6].

While the material was heated inside the extrusion chamber, the temperature approached 450 °C. As the TTT-diagram in Figure 51 suggested, the precipitation kinetics of iron in solid solution was optimized around this temperature. The possibility of concurrent precipitation of iron during compression is therefore likely. Precipitates hampers recrystallization, and a possible pinning effect hindered following grain growth. This is advantageous in terms of strength through the Hall-Petch effect. At the same time, heterogeneous precipitation at grain boundaries of foreign elements could increase the conductivity. The grain boundaries itself are reported to have a minimum effect on the resulting electrical conductivity.

With insight into the thermal history of the screw extruded wire, the final extrudate can be assessed. It was confirmed with highest certainty that the as-screw extruded wire mainly consisted of fiber grains aligned in the extrusion direction. A high fraction of low angle grain boundaries (LAGB) indicates a subgrain structure, which imply a partly recrystallized structure. Deformation forces connected to pushing the material through the die was responsible for producing fiber shaped grains. This microstructure was probably kept in place by the concurrent precipitation, hampering the grains from recrystallizing before the wire was water quenched. Grains at the wire periphery were recrystallized, probably due to a higher heat input at this position.

5.3.3 Ferrous particles

TEM micrographs of as-extruded wire in Figure 46-47 revealed particles pinning the grain boundaries. At the 2000X magnified bright field image in Figure 46, three such particles were shown. The pinning is believed to be highly potent, and occurring frequently in the extruded material. The dark field micrograph in Figure 46 (b) show a bright pinning particle, which imply a composition of heavier elements than the matrix. Thus, the pinning arised from Al-Fe intermetallic particles. As the grain boundary bends around Al-Fe particles, the particles contribute to increasing the energy required for migrating the boundary. Particles thus serve as a grain refining agent.

The proposed pinning effect of intermetallic particles could suggest an accumulation of iron at grain boundaries. The SEM backscatter image in Figure 45 rejected this suggestion, clearly showing a random distribution of iron precipitates throughout the matrix. Several reasons can explain this fine dispersion. First, the low solubility of iron means that a majority of the alloying element is present in precipitated state at all times. These iron depositions are randomly spread out in the matrix as the material gets deformed in the extrusion chamber. Secondly, it is assumed that precipitation do take place during compression in the screw extruder. At the same time, grains recrystallize and gets deformed in a repetitive manner. If iron particles precipitate at grain boundaries, boundaries will disappear as a consequence of deformation. Thus, the resulting microstructure would consist of particles randomly dispersed in the matrix.

TEM micrographs in Figure 48 showed a triple junction boundary of as-screw extruded wire in longitudinal direction. Both bright and dark field mode indicated some sort of substance occupying the whole boundary. A bright contrast in dark field mode eventually express a heavier element present, e.g. iron intermetallic phases. It is known that Fe-Al intermetallic phases do precipitate heterogeneously on grain boundaries [21]. Another explanation is particle straining which distorts the lattice at the boundary, fulfilling Bragg condition which results in a bright contrast in dark field.

However, a dense ferrous particle assemble was not seen in any other samples than the one showed in Figure 48, neither in SEM nor TEM. An explanation to this artifact is called Moiré fringing [49]. Moiré fringing arises by interference of two overlapping low-angle misfit planes. If imaging in longitudinal section of a fiber-structured wire with strong cube texture intensity, low-angled interference is probable. This can in turn produce a bright edge around the boundary in TEM dark field.

5.3.4 Oxides

EDS examination revealed that oxides were present in the screw extruded matrix. These were introduced during extrusion, both in form of surface oxides on the feedstock granulates, and as air pockets inside the extruder. Aluminium oxide, Al_2O_3 , is a very stable phase, thus easily created at elevated temperatures. The EDS examination also confirmed that oxides drives silicon out of solid solution.

An approximate 3:1, Al to O ratio, was reported by the EDS analysis. Al_2O_3 has, obviously, a 2:3 ratio. The source of error is connected to the emission depth of reflected X-rays. At 10 keV, the theory predicts an emission depth of 1.3 μm [50]. With oxide particles being sub one micron, the detected amount of aluminium will be artificially high.

5.3.5 Effect of isothermal tempering on screw extruded wire

Prolonged tempering of the screw extruded wire at 450 °C had big influences on final microstructure and properties. As the wire was partly recrystallized after extrusion, tempering completed the recrystallization, producing a random orientation of the new grains. As the tempering continued, grain boundaries started to migrate in the central area, resulting in abnormal large grains.

Oxides in the tempered wire encircled grain boundaries. Compared to the oxides in as-extruded wire, the coarsening was beyond all imagination. From being circular sub one micron particles, the resulting phase grew to a width of 10 μm and several hundred microns long, Figure 50.

The screw extruded wire was made of granulated material, which probably contained a hydroxide on the surface [44]. This included hydrogen or other contaminants from the extrusion chamber could cause internal cracking of the material under subsequent tempering, as showed by Ringstad [51]. SiC slurry from the final stages of metallographic polishing could then adhere in cracks and oxidize in contact with air. For the examined screw extruded and tempered specimen, Diapro NAP B1 and MasterMet 2 were used as polishing agents. Investigations of the actual safety data sheets revealed that Diapro NAP B1 could contain fluorine-containing additives, explaining the high amount of fluorine detected by EDS and reported in Table 9 [52, 53].

5.3.6 Conductivity evolution

As seen in Figure 34, the conductivity fell for screw extruded wire with increased tempering time. Factors affecting the final conductivity are discussed in the following paragraphs.

Most prominent was the loss of texture as a consequence of tempering. The as-extruded wire with low-angled fiber grains in extrusion direction may represent an advantageous texture in terms of conductivity. Fiber grains can act as electron channels, which lead to unimpeded flow in the direction of current. A low angle ($<15^\circ$) between channel terminals represent a minimum scattering of electrons, as the lattice misorientation is small.

It was already shown that recrystallization happened in the range of 5 minutes for isothermal tempering at 450 $^\circ\text{C}$. The majority of the favourable cube texture would hence be gone in minutes after tempering. As the conductivity curve in Figure 34 showed, a significant conductivity decrease was not reached before 8 hours of tempering. Thus, the texture transformation can not alone explain the decrease of electrical conductivity during tempering.

Particles or cracks introduced under tempering do not serve as a proper conductor. Its size and frequent appearance in the material made it a significant contributor to lowering electrical conductivity. The formation kinetics of these structures are not known, but could possibly take several hours to develop. This will if so explain the constant drop in conductivity in Figure 34.

5.4 Strength-conductivity relation for electrical conductors

As the theoretical presentation in Section 2.6 states, strength and conductivity are compromising properties in aluminium. To illustrate the inverse relation between these properties, ultimate tensile strength (UTS) is plotted against electrical conductivity in Figure 55. The plot was based on results in this master's thesis and from other literature. Different aluminium series, production methods, tempering lapses and special alloying treatments (e.g. boron treatment [34,54,55]) were included.

An approximate linear dependence is shown in Figure 55, which illustrates the compromise of properties very well. The linear regressed red trend line acts as a threshold for electrical conductors; those lying above being more well-performing. The objective is to produce a conductor lying in the upper right quadrant, optimizing the strength without losing conductivity redundantly.

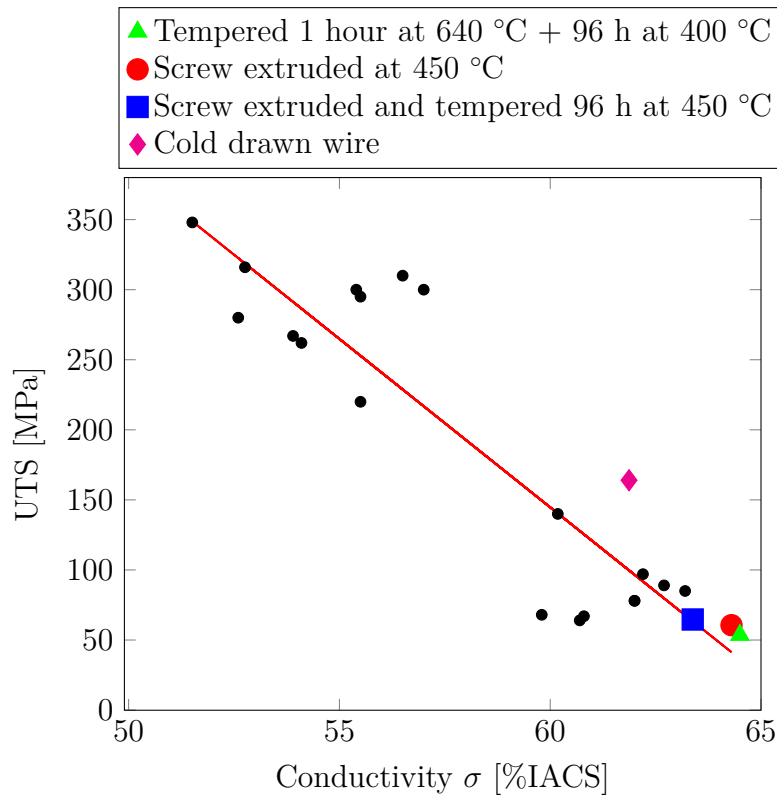


Figure 55: Tensile strength-conductivity relation between different aluminium alloys. The red trend line is linear regressed from black points based on [34,43,54–61]. Screw extruded wire (●) exhibits a very high conductivity, while being soft. Cold drawn wire (◆) is stronger, but with poorer electrical properties.

This thesis has examined three solutions to obtain a well-performing electrical conducting wire; isothermal tempering from solid solution treated drawn wire (▲), screw extrusion (●) and screw extrusion followed by isothermal tempering (■). All wires exhibited an extremely high electrical conductivity, due to a recrystallized and highly precipitated structure. On the other hand, the microstructural state made them very soft. The best combination of strength and conductivity was exhibited by the as-screw extruded wire produced at 450 °C (●).

To compare with the base material, cold drawn wire (◆), this material has a better optimization of properties. Wire drawing at room temperature introduces a higher degree of straining, thus a stronger material. At the same time, electrical conductivity is fairly high. As a consequence, the material becomes low-ductile, showed in Figure 22.

The produced screw extruded wire described in this thesis was outrun by the untempered drawn wire. To obtain a screw extruded product with the same or better properties, a lower extrusion temperature may be the key. This will inhibit the recrystallization process, producing a harder material. The possibility of producing nano-sized severe plastic deformed (SPD) structures opens the opportunity of novel properties in terms of the strength-conductivity relation.

6 Conclusion

This study has primarily assessed the effect of alloying elements on electrical conductivity in commercial pure aluminium. The effect of tempering on screw extruded wires was also explored. Key findings are summarized and presented in this section.

- The effects of iron, silicon and manganese in solid solution versus precipitated state on electrical properties have been evaluated by a modified empirical equation based on the work of Lok [32]. Measurements show that electrical conductivity can be greatly enhanced by precipitation of iron.
- A newly assessed time-temperature-transformation diagram on precipitation kinetics of ferrous intermetallic particles in aluminium revealed deposition of iron to be swiftest around 450 °C.
- A linear strength-conductivity relation has been determined for aluminium, independent of production method, alloying content and heat-treatment. The relation describes the compromise of tensile strength and electrical conductivity with fairly good precision.
- Screw extruded wire produced at 450 °C showed a good combination of mechanical and electrical properties. Subsequent tempering resulted in a degraded material with internal cracking, probably arising from hydrogen contamination.
- The screw extruded wire underachieved in terms of the strength-conductivity relation, compared to a commercial cold drawn wire. The screw extruded solution is therefore not considered to be competitive as an electrical conductor at present. It is believed that a lower extrusion temperature can optimize these desired properties.

References

- [1] Siemens AG. White paper: Aluminum versus copper conductors. Technical report, Siemens AG Building Technologies Division, Gubelstrasse 22, 6301 Zug, Switzerland, Sep 2014.
- [2] F Lambiase and A Di Ilio. A parametric study on residual stresses and loads in drawing process with idle rolls. *Materials & Design*, 32(10):4832–4838, 2011.
- [3] J R Wilcox. The wire drawing process, Aug 2010. Available at <https://core.materials.ac.uk/search/detail.php?id=3672>.
- [4] A El-Domiaty and S Z Kassab. Temperature rise in wire-drawing. *Journal of Materials Processing Technology*, 83(1):72–83, 1998.
- [5] I Samajdar and S K Varma. The effect of wire drawing speed on the dislocation cell size and yield strength in pure aluminum. *Materials Science and Engineering: A*, 141(2):L1–L3, 1991.
- [6] J C Werenskiold et.al. Screw extruder for continuous extrusion of materials with high viscosity, 2009. International patent number EP2086697B1 WO2008 06307. Patent reference JP-A-2004 035 961, US-A-2 787 022.
- [7] K Ortrud. *Iron—Binary phase diagrams*, volume 1. Springer Science & Business Media, Berlin Heidelberg, 1982. ISBN 978-3-662-08024-5.
- [8] U R Kattner and B P Burton. Phase diagrams of binary iron alloys. *Okamoto, ASM International, Materials Park, OH*, pages 12–28, 1992.
- [9] U Burkhardt, M Ellner, J Grin, H Ipser, K Richter, J Schuster, and F Weitzer. Aluminium transition metal phase diagrams. *Iron-Aluminium*, pages 54–58, 1998.
- [10] M Turchanin, N Kolchugina, A Watson, and A Kroupa. Al-Fe binary phase diagram evaluation. *MSI Eureka*, 2013.
- [11] X Li, A Scherf, M Heilmaier, and F Stein. The Al-rich part of the Fe-Al phase diagram. *Journal of Phase Equilibria and Diffusion*, 37(2):162–173, 2016.
- [12] N A Belov, A A Aksenov, and D G Eskin. *Iron in aluminium alloys: impurity and alloying element*. Taylor & Francis, 11 New Fetter Lane, London EC4P 4EE, first edition, 2002. ISBN 0-415-27352-8.
- [13] K Ito, R Musick, and K Lücke. The influence of iron content and annealing temperature on the recrystallization textures of high-purity aluminium-iron alloys. *Acta Metallurgica*, 31(12):2137–2149, 1983.
- [14] P Skjerpe. Intermetallic phases formed during DC-casting of an Al- 0.25 wt pct Fe- 0.13 wt pct Si alloy. *Metallurgical and Materials Transactions A*, 18(2):189–200, 1987.
- [15] V Raghavan. Al-Fe-Si (aluminum-iron-silicon). *Journal of phase equilibria*, 23(4):362–366, 2002.

- [16] J Grin, U Burkhardt, M Ellner, and K Peters. Refinement of the Fe₄Al₁₃ structure and its relationship to the quasihomological homeotypical structures. *Zeitschrift fuer Kristallographie*, 209(6):479–487, 1994.
- [17] L K Walford. The structure of the intermetallic phase FeAl₆. *Acta Crystallographica*, 18(2):287–291, 1965.
- [18] Y Liu, B Al-Matar, and G Newaz. An investigation on the interface in a niti short-fiber-reinforced 6061 aluminum composite by transmission electron microscope. *Metallurgical and Materials Transactions A*, 39(11):2749–2759, 2008.
- [19] Q Zhao, Z Qian, X Cui, Y Wu, and X Liu. Optimizing microstructures of dilute Al–Fe–Si alloys designed with enhanced electrical conductivity and tensile strength. *Journal of Alloys and Compounds*, 650:768–776, 2015.
- [20] W Khalifa, F H Samuel, and J E Gruzleski. Iron intermetallic phases in the Al corner of the Al–Si–Fe system. *Metallurgical and Materials Transactions A*, 34(3):807–825, 2003.
- [21] O N Senkov, F H Froes, V V Stolyarov, R Z Valiev, and J Liu. Microstructure and microhardness of an Al Fe alloy subjected to severe plastic deformation and aging. *Nanostructured materials*, 10(5):691–698, 1998.
- [22] J K Solberg. Teknologiske metaller og legeringer. Tapir forlag, NTNU, 2010.
- [23] J G Morris and W C Liu. Al alloys: The influence of concurrent precipitation on recrystallization behavior, kinetics, and texture. *JOM*, 57(11):44, 2005.
- [24] R JD Tilley. *Understanding solids: the science of materials*. John Wiley & Sons, The Atrirum, Southern Gate, Chichester, West Sussex PO19 8SQ, England, second edition, 2004. ISBN 0-470-85276-5.
- [25] P Kuiper. Emergent behavior in crystalline solids, 2007. Available at <https://www.learner.org/courses/physics/visual/visual.html?shortname=bands>.
- [26] C Kittel. *Introduction to Solid State Physics*. John Wiley & Sons, 111 River Street, Hoboken, NJ 07030-5774, eight edition, 2005. ISBN 978-0-471-41526-8.
- [27] C R Nave. Microscopic view of ohm’s law, 2016. Available at <http://hyperphysics.phy-astr.gsu.edu/hbase/electric/ohmmic.htmlc1>.
- [28] C Jacoboni. *Theory of Electron Transport in Semiconductors: A Pathway from Elementary Physics to Nonequilibrium Green Functions*, volume 165. Springer Science & Business Media, Berlin Heidelberg, 2010. ISBN 978-3-642-10586-9.
- [29] The-Crankshaft Publishing. Electrical properties of materials, Mar 2017. Available at <http://what-when-how.com/electronic-properties-of-materials/electrical-conduction-in-metals-and-alloys-electrical-properties-of-materials-part-2/>.
- [30] J Schrank, M Zehetbauer, W Pfeiler, and L Trieb. Effect of high deformation of electrical resistivity in pure aluminium. *Scripta Metallurgica*, 14(10):1125–1128, 1980.
- [31] Y Miyajima, S Komatsu, M Mitsuhashi, S Hata, H Nakashima, and N Tsuji. Change in electrical resistivity of commercial purity aluminium severely plastic deformed. *Philosophical Magazine*, 90(34):4475–4488, 2010.

- [32] Z J Lok. High temperature plastic deformation and related solute effects in aluminium based alloys. *The Netherlands Inst. Met. Res.*, 2001.
- [33] F Kutner. Aluminum conductor materials. *Aluminium-Verlag GmbH*, pages 15–27, 1981.
- [34] S Karabay. Influence of AlB₂ compound on elimination of incoherent precipitation in artificial aging of wires drawn from redraw rod extruded from billets cast of alloy AA-6101 by vertical direct chill casting. *Materials & Design*, 29(7):1364–1375, 2008.
- [35] G Wang, S Liu, H Gao, W Zhou, C Li, and Q Gao. Effects of boron on the electrical conductivities of commercial aluminum. *Acta Metallurgica Sinica - Chinese Edition*, 36(6):597–601, 2000.
- [36] A R Eivani, H Ahmed, J Zhou, and J Duszczek. Correlation between electrical resistivity, particle dissolution, precipitation of dispersoids, and recrystallization behavior of AA7020 aluminum alloy. *Metallurgical and Materials Transactions A*, 40(10):2435–2446, 2009.
- [37] P Olafsson, R Sandstrom, and Å Karlsson. Comparison of experimental, calculated and observed values for electrical and thermal conductivity of aluminium alloys. *Journal of materials science*, 32(16):4383–4390, 1997.
- [38] X Sauvage, E V Bobruk, M Y Murashkin, Y Nasedkina, N A Enikeev, and R Z Valiev. Optimization of electrical conductivity and strength combination by structure design at the nanoscale in Al–Mg–Si alloys. *Acta Materialia*, 98:355–366, 2015.
- [39] S W Stratton. Copper wire tables. Technical Report 31, Circular of the Bureau of Standards, Oct 1914.
- [40] W F Gale and T C Totemeier. *Smithells metals reference book*. Elsevier Butterworth-Heinemann, The Boulevard, Langford Lane, Kidlington, Oxford, OX5 1GB, eight edition, 2004. ISBN 0-7506-7509-8.
- [41] J R Davids. ASM specialty handbook, aluminium and aluminum alloys. ASM International, ASM World Headquarters, 9639 Kinsman Road, Materials Park, OH 44073-0002, 1993. ISBN 978-0-87170-496-2.
- [42] L H Ebbesen. Utvikling av elektrisk leder i aluminium produsert ved skruuekstrudering. Master’s thesis, NTNU, IMT, Dec 2015.
- [43] G Langelandsvik. Electrical conductivity in commercial pure aluminium. Technical report, NTNU, IMT, Dec 2016.
- [44] A Bilsbak. Mikrostruktur og mekaniske egenskaper for skruuekstrudert aluminium: Karakterisering av skruuekstrudert aluminium etter ulike rensmetoder av råmateriale. Master’s thesis, NTNU, IMT, Jun 2012.
- [45] A Vorup. Safety data sheet, electrolyte A2-I, Jan 2016. Available at http://www.struers.com/Content/Documents/SDS/ELECTROLYTE%20A2-I/ELECTROLYTE%20A2-I_US_EN_M0010_16.0_27-01-2016.pdf.
- [46] B Hutchinson. Lecture - metals and textures – 4 non-ferrous metals. Corrosion and Metals Research Institute (KIMAB). Available at http://www.3me.tudelft.nl/fileadmin/Faculteit/3mE/Over_de_faculteit/Afdelingen/

- [47] F R Fickett. Aluminum—1. a review of resistive mechanisms in aluminum. *Cryogenics*, 11(5):349–367, 1971.
- [48] S Wronski, K Wierzbanski, M Jędrychowski, J Tarasiuk, M Wronski, A Baczmanski, and B Bacroix. Microstructure evolution of titanium after tensile test. *Materials Science and Engineering: A*, 656:1–11, 2016.
- [49] C B Carter and D B Williams. *Transmission electron microscopy*. Springer-Verlag US, 233 Spring Street, New York, NY 10013-1578, USA, 3 edition, 2009. ISBN 978-0-387-76501-3.
- [50] J Hjelen. Scanning elektron-mikroskopi. Kompendium, Tapir forlag, Nardovegen 12, 7032 Trondheim, Norway, 1986.
- [51] R H Ringstad. Karakterisering av aluminium ekstrudert med ulike skruegeometrier. Master’s thesis, NTNU, IMT, Jun 2010.
- [52] A Vorup. Safety data sheet, Diapro NAP B1, Nov 2015. Available at https://e-shop.struers.com/FI/EN/documents/40600373_Msds_FI_Swedish_9234c481c42ed1b1345774566bfe226b.aspx.
- [53] Buehler. Safety data sheet, MasterMet 2, Mar 2012. Available at https://shop.buehler.com/sites/default/files/resources/9109295_2.pdf.
- [54] X Cui, Y Wu, X Liu, Q Zhao, and G Zhang. Effects of grain refinement and boron treatment on electrical conductivity and mechanical properties of AA1070 aluminum. *Materials & Design*, 86:397–403, 2015.
- [55] S Karabay. Modification of AA-6201 alloy for manufacturing of high conductivity and extra high conductivity wires with property of high tensile stress after artificial aging heat treatment for all-aluminium alloy conductors. *Materials & design*, 27(10):821–832, 2006.
- [56] F Pan, D V Edmonds, S Zhou, and P Ding. Effects of rare earth metals on electrical conductivity and mechanical properties of commercial purity aluminium. *Materials science and technology*, 10(11):933–935, 1994.
- [57] M H Mulazimoglu, A Zaluska, F Paray, and J E Gruzleski. The effect of strontium on the Mg₂Si precipitation process in 6201 aluminum alloy. *Metallurgical and Materials Transactions A*, 28(6):1289–1295, 1997.
- [58] F Wang. Effect of Cu on mechanical properties and electrical conductivity of hot-extruded AlMgSi alloy. *Journal of Shenyang University of Technology*, 37, 2015.
- [59] W Yuan and Z Liang. Effect of Zr addition on properties of Al–Mg–Si aluminum alloy used for all aluminum alloy conductor. *Materials & Design*, 32(8):4195–4200, 2011.
- [60] W Yuan, Z Liang, C Zhang, and L Wei. Effects of La addition on the mechanical properties and thermal-resistant properties of Al–Mg–Si–Zr alloys based on AA 6201. *Materials & Design*, 34:788–792, 2012.

- [61] C Lü, H Liao, Y Liu, and Q Wang. Effect of Ce on castability, mechanical properties and electric conductivity of commercial purity aluminum. *China Foundry*, 12(4), 2015.

Appendices

A Conversion from resistance to conductivity

Table 11 through 16 provide data for converting resistance results obtained by AIOP OM21 microohmmeter to electrical conductivity for all wires examined in this thesis. Conductivity σ is given in both the form of MS/m and %IACS. The basis for the resistance conversion is Equation 12, where σ is electrical conductivity; L is the distance between measuring points in mm; l is the specimen bar length in mm, R the resistance in Ω ; ρ is the material density in g/mm³ determined by the chemical composition in Table 3; and m is the specimen bar mass in g. Table 10 shows the uncertainties of the different input parameters. These are the base for determining the total conductivity uncertainty $\Delta\sigma$ by Gauss law for error propagation.

$$\sigma = \frac{Ll}{R\rho m} \quad (12)$$

Table 10: Uncertainties for input parameters for determining conductivity uncertainty $\Delta\sigma$.

Parameter	Uncertainty
ΔL [mm]	0.05
Δl [mm]	0.5
$\Delta \rho$ [g/mm ³]	0.000001
ΔR [m Ω]	0.00069
Δm [g]	0.0001

Table 11: Isothermal tempered wires at 300 and 350 °C.
The number in parenthesis represents tempering time in hours.

Parameter	300(0)	300(0.25)	300(0.5)	300(1)	300(2)	300(4)	300(8)	300(18)	300(24)	300(48)	300(96)
L [mm]	98.45	98.45	98.45	98.45	98.45	98.45	98.45	98.45	98.45	98.45	98.45
l [mm]	224	221	222	222	221	222	221.5	222	222	210.5	218
m [g]	4.3030	4.2435	4.2499	4.2655	4.2362	4.2684	4.2437	4.2636	4.2663	4.0319	4.1851
ρ [g/mm ³]	0.002709	0.002709	0.002709	0.002709	0.002709	0.002709	0.002709	0.002709	0.002709	0.002709	0.002709
Area [mm ²]	7.09	7.09	7.07	7.09	7.08	7.10	7.07	7.09	7.09	7.07	7.09
Radius [mm]	1.50	1.50	1.50	1.50	1.50	1.50	1.50	1.50	1.50	1.50	1.50
Diameter [mm]	3.00	3.00	3.00	3.01	3.00	3.01	3.00	3.00	3.01	3.00	3.00
R [mΩ]	0.385	0.384	0.386	0.385	0.386	0.385	0.386	0.385	0.384	0.385	0.383
σ [MS/m]	36.06	36.15	36.09	36.05	36.05	36.04	36.04	36.08	36.12	36.20	36.27
$\Delta\sigma$ [MS/m]	0.106	0.107	0.106	0.106	0.106	0.106	0.106	0.106	0.107	0.110	0.108
σ [%IACS]	62.17	62.32	62.22	62.15	62.15	62.14	62.14	62.20	62.28	62.41	62.53
$\Delta\sigma$ [%IACS]	0.182	0.184	0.183	0.183	0.183	0.183	0.183	0.183	0.184	0.190	0.187

Parameter	350(0)	350(0.25)	350(0.5)	350(1)	350(2)	350(4)	350(7)	350(10.5)	350(20)	350(24)	350(48)	350(96)
L [mm]	98.45	98.45	98.45	98.45	98.45	98.45	98.45	98.45	98.45	98.45	98.45	98.45
l [mm]	216	217	193	212	219	200.5	218	215	216	216	219	219.5
m [g]	4.1443	4.1604	3.7009	4.0677	4.2117	3.8473	4.1902	4.1209	4.1319	4.1331	4.1942	4.2227
ρ [g/mm ³]	0.002709	0.002709	0.002709	0.002709	0.002709	0.002709	0.002709	0.002709	0.002709	0.002709	0.002709	0.002709
Area [mm ²]	7.08	7.08	7.08	7.08	7.10	7.08	7.10	7.08	7.06	7.06	7.07	7.10
Radius [mm]	1.50	1.50	1.50	1.50	1.50	1.50	1.50	1.50	1.50	1.50	1.50	1.50
Diameter [mm]	3.00	3.00	3.00	3.00	3.01	3.00	3.01	3.00	3.00	3.00	3.00	3.01
R [mΩ]	0.385	0.385	0.386	0.385	0.383	0.384	0.385	0.385	0.382	0.383	0.380	0.376
σ [MS/m]	36.08	36.11	36.02	36.15	36.17	36.17	36.09	36.18	36.49	36.44	36.64	36.88
$\Delta\sigma$ [MS/m]	0.108	0.108	0.116	0.110	0.108	0.113	0.108	0.109	0.110	0.109	0.109	0.110
σ [%IACS]	62.20	62.26	62.10	62.33	62.37	62.35	62.22	62.38	62.91	62.83	63.17	63.59
$\Delta\sigma$ [%IACS]	0.186	0.186	0.199	0.189	0.185	0.196	0.185	0.187	0.189	0.189	0.188	0.190

Table 12: Isothermal tempered wires at 400 °C.
The number in parenthesis represents tempering time in hours.

Parameter	400(0)	U400(3e-3)	U400(2e-2)	U400(8e-2)	U400(.25)	400(0.5)	400(1)	400(2)
L [mm]	98.45	98.45	98.45	98.45	98.45	98.45	98.45	98.45
l [mm]	218	244	249.5	237	220.5	218	218	219
m [g]	4.1771	4.6942	4.7876	4.5501	4.2318	4.1811	4.1806	4.1924
ρ [g/mm ³]	0.002709	0.002709	0.002709	0.002709	0.002709	0.002709	0.002709	0.002709
Area [mm ²]	7.07	7.10	7.08	7.09	7.08	7.08	7.08	7.07
Radius [mm]	1.50	1.50	1.50	1.50	1.50	1.50	1.50	1.50
Diameter [mm]	3.00	3.01	3.00	3.00	3.00	3.00	3.00	3.00
R [mΩ]	0.386	0.385	0.386	0.386	0.386	0.386	0.385	0.384
σ [MS/m]	36.04	35.98	36.00	35.99	36.03	36.02	36.15	36.31
$\Delta\sigma$ [MS/m]	0.107	0.101	0.099	0.102	0.107	0.107	0.108	0.108
σ [%IACS]	62.13	62.04	62.07	62.05	62.12	62.11	62.33	62.60
$\Delta\sigma$ [%IACS]	0.185	0.173	0.171	0.176	0.184	0.185	0.186	0.186

Parameter	400(4)	400(7)	400(10.5)	400(20)	400(24)	400(48)	400(96)
L [mm]	98.45	98.45	98.45	98.45	98.45	98.45	98.45
l [mm]	204	217	201.5	215	197	217.5	217
m [g]	3.9104	4.1593	3.8671	4.1257	3.7814	4.1729	4.1431
ρ [g/mm ³]	0.002709	0.002709	0.002709	0.002709	0.002709	0.002709	0.002709
Area [mm ²]	7.08	7.08	7.08	7.08	7.09	7.08	7.05
Radius [mm]	1.50	1.50	1.50	1.50	1.50	1.50	1.50
Diameter [mm]	3.00	3.00	3.00	3.00	3.00	3.00	3.00
R [mΩ]	0.383	0.381	0.378	0.376	0.374	0.372	0.373
σ [MS/m]	36.32	36.51	36.75	36.95	37.16	37.36	37.41
$\Delta\sigma$ [MS/m]	0.113	0.109	0.116	0.112	0.119	0.113	0.113
σ [%IACS]	62.61	62.96	63.36	63.71	64.06	64.41	64.50
$\Delta\sigma$ [%IACS]	0.194	0.189	0.199	0.193	0.205	0.194	0.195

Table 13: Isothermal tempered wires at 450 °C.
The number in parenthesis represents tempering time in hours.

Parameter	400(0)	U400(3e-3)	U400(2e-2)	U400(8e-2)	U400(.25)	400(0.5)	400(1)
L [mm]	98.45	98.45	98.45	98.45	98.45	98.45	98.45
l [mm]	218	244	249.5	237	220.5	218	218
m [g]	4.1771	4.6942	4.7876	4.5501	4.2318	4.1811	4.1806
ρ [g/mm ³]	0.002709	0.002709	0.002709	0.002709	0.002709	0.002709	0.002709
Area [mm ²]	7.07	7.10	7.08	7.09	7.08	7.08	7.08
Radius [mm]	1.50	1.50	1.50	1.50	1.50	1.50	1.50
Diameter [mm]	3.00	3.01	3.00	3.00	3.00	3.00	3.00
R [mΩ]	0.386	0.385	0.386	0.386	0.386	0.386	0.385
σ [MS/m]	36.04	35.98	36.00	35.99	36.03	36.02	36.15
$\Delta\sigma$ [MS/m]	0.107	0.101	0.099	0.102	0.107	0.107	0.108
σ [%IACS]	62.13	62.04	62.07	62.05	62.12	62.11	62.33
$\Delta\sigma$ [%IACS]	0.185	0.173	0.171	0.176	0.184	0.185	0.186

Parameter	400(2)	400(4)	400(7)	400(10.5)	400(20)	400(24)	400(48)	400(96)
L [mm]	98.45	98.45	98.45	98.45	98.45	98.45	98.45	98.45
l [mm]	219	204	217	201.5	215	197	217.5	217
m [g]	4.1924	3.9104	4.1593	3.8671	4.1257	3.7814	4.1729	4.1431
ρ [g/mm ³]	0.002709	0.002709	0.002709	0.002709	0.002709	0.002709	0.002709	0.002709
Area [mm ²]	7.07	7.08	7.08	7.08	7.08	7.09	7.08	7.05
Radius [mm]	1.50	1.50	1.50	1.50	1.50	1.50	1.50	1.50
Diameter [mm]	3.00	3.00	3.00	3.00	3.00	3.00	3.00	3.00
R [mΩ]	0.384	0.383	0.381	0.378	0.376	0.374	0.372	0.373
σ [MS/m]	36.31	36.32	36.51	36.75	36.95	37.16	37.36	37.41
$\Delta\sigma$ [MS/m]	0.108	0.113	0.109	0.116	0.112	0.119	0.113	0.113
σ [%IACS]	62.60	62.61	62.96	63.36	63.71	64.06	64.41	64.50
$\Delta\sigma$ [%IACS]	0.186	0.194	0.189	0.199	0.193	0.205	0.194	0.195

Table 14: Isothermal tempered wires at 500 °C.
The number in parenthesis represents tempering time in hours.

Parameter	U500(0)	U500(3e-3)	U500(2e-2)	U500(8e-2)	U500(.25)	500(0.5)	500(1)	500(2)
L [mm]	98.45	98.45	98.45	98.45	98.45	98.45	98.45	98.45
l [mm]	236	236	223	219	226	217.5	206	207
m [g]	4.5349	4.5302	4.2733	4.2006	4.3370	4.1584	3.9497	3.9719
ρ [g/mm ³]	0.002709	0.002709	0.002709	0.002709	0.002709	0.002709	0.002709	0.002709
Area [mm ²]	7.09	7.09	7.07	7.08	7.08	7.04	7.08	7.08
Radius [mm]	1.50	1.50	1.50	1.50	1.50	1.50	1.50	1.50
Diameter [mm]	3.01	3.00	3.00	3.00	3.00	2.99	3.00	3.00
R [mΩ]	0.386	0.386	0.386	0.386	0.385	0.384	0.381	0.379
σ [MS/m]	35.95	36.02	36.07	36.06	36.12	36.36	36.52	36.67
$\Delta\sigma$ [MS/m]	0.102	0.102	0.106	0.107	0.105	0.109	0.113	0.113
σ [%IACS]	61.98	62.11	62.19	62.17	62.27	62.69	62.97	63.22
$\Delta\sigma$ [%IACS]	0.176	0.177	0.183	0.185	0.182	0.188	0.195	0.195

Parameter	500(4)	500(7)	500(10.5)	500(20)	500(24)	500(48)	500(96)
L [mm]	98.45	98.45	98.45	98.45	98.45	98.45	98.45
l [mm]	215.5	210.5	217	211	201	219	218
m [g]	4.1214	4.0369	4.1658	4.0512	3.8520	4.1917	4.1823
ρ [g/mm ³]	0.002709	0.002709	0.002709	0.002709	0.002709	0.002709	0.002709
Area [mm ²]	7.06	7.08	7.09	7.09	7.07	7.07	7.08
Radius [mm]	1.50	1.50	1.50	1.50	1.50	1.50	1.50
Diameter [mm]	3.00	3.00	3.00	3.00	3.00	3.00	3.00
R [mΩ]	0.378	0.376	0.375	0.375	0.375	0.374	0.374
σ [MS/m]	36.89	37.02	37.04	37.07	37.11	37.23	37.16
$\Delta\sigma$ [MS/m]	0.111	0.114	0.112	0.114	0.117	0.112	0.112
σ [%IACS]	63.61	63.83	63.86	63.91	63.98	64.18	64.07
$\Delta\sigma$ [%IACS]	0.192	0.196	0.193	0.196	0.202	0.193	0.193

Table 15: Isothermal tempered wires at 560 °C.
The number in parenthesis represents tempering time in hours.

Parameter	560(0)	560(0.25)	560(0.5)	560(1)	560(2)	560(4)	560(8)	560(19.5)	560(24)	560(48)
L [mm]	98.45	98.45	98.45	98.45	98.45	98.45	98.45	98.45	98.45	98.45
l [mm]	211	210	209	208	208	209	212	209	211	210
m [g]	4.0384	4.0714	3.9926	3.9935	4.0038	4.0300	4.0973	4.0546	4.0722	4.0415
ρ [g/mm ³]	0.002709	0.002709	0.002709	0.002709	0.002709	0.002709	0.002709	0.002709	0.002709	0.002709
Area [mm ²]	7.0651	7.1567	7.0518	7.0873	7.1056	7.1179	7.1343	7.1613	7.1242	7.1042
Radius [mm]	1.50	1.51	1.50	1.50	1.50	1.51	1.51	1.51	1.51	1.50
Diameter [mm]	3.00	3.02	3.00	3.00	3.01	3.01	3.01	3.02	3.01	3.01
R [mΩ]	0.388	0.384	0.389	0.383	0.383	0.381	0.379	0.379	0.381	0.380
σ [MS/m]	35.89	35.86	35.93	36.29	36.19	36.30	36.41	36.23	36.31	36.46
$\Delta\sigma$ [MS/m]	0.11	0.11	0.11	0.11	0.11	0.11	0.11	0.11	0.11	0.11
σ [%IACS]	61.87	61.83	61.95	62.56	62.40	62.58	62.78	62.47	62.61	62.87
$\Delta\sigma$ [%IACS]	0.187	0.189	0.189	0.192	0.192	0.192	0.191	0.192	0.191	0.192

Table 16: Screw extruded wire (450Q) isothermally tempered at 450 °C.
The number in parenthesis represents tempering time in hours.

Parameter	450Q(0)	450Q(0.5)	450Q(2)	450Q(8)	450Q(24)	450Q(96)
L [mm]	98.45	98.45	98.45	98.45	98.45	98.45
l [mm]	272	285.5	285.5	285.5	285.5	285.5
m [g]	4.8003	5.0374	5.0374	5.0374	5.0374	5.0374
ρ [g/mm ³]	0.002709	0.002709	0.002709	0.002709	0.002709	0.002709
Area [mm ²]	6.51	6.51	6.51	6.51	6.51	6.51
Radius [mm]	1.44	1.44	1.44	1.44	1.44	1.44
Diameter [mm]	2.88	2.88	2.88	2.88	2.88	2.88
R [m Ω]	0.406	0.405	0.406	0.407	0.408	0.411
σ [MS/m]	37.22	37.29	37.20	37.16	37.08	36.76
$\Delta\sigma$ [MS/m]	0.096	0.094	0.094	0.094	0.093	0.092
σ [%IACS]	64.17	64.30	64.14	64.06	63.93	63.38
$\Delta\sigma$ [%IACS]	0.166	0.162	0.162	0.161	0.161	0.159

B Calibration of AOIP OM21

The calibration results from Vigeland metal are provided in Table 17. The uncertainty is determined by calculating the standard deviation for all measurements.

Table 17: Resistance results in $m\Omega m$ for Vigeland metal.

Test [m Ω m] / T[$^{\circ}$ C]	20.1	20.6	22.0
1	0.277	0.276	0.278
2	0.276	0.276	0.277
3	0.276	0.277	0.276
4	0.276	0.278	0.277
5	0.277	0.277	0.276
6	0.277	0.276	0.276
7	0.277	0.278	0.276
8	0.277	0.277	0.276
9	0.278	0.276	
10	0.276	0.276	
11	0.277	0.276	
12	0.277	0.277	
13	0.277	0.276	
14	0.277	0.276	
15	0.278	0.277	
16	0.277	0.276	
Average	0.2766	0.2769	0.2765
Standard deviation	0.000619	0.000727	0.000756

C Hardness measurements

Hardness measurement of all samples are provided in Table 18 through 25. All values are given in Hardness Vickers, HV.

Table 18: Hardness results for wires tempered for 5 minutes.
Temperature is indicated in the first row.

Sample	350 °C	450 °C	550 °C
1	44.1	20	25.2
2	43.6	18.6	23.6
3	44.5	19.5	22.2
4	41.8	21.2	23.4
5	42.5	21.5	22.3
6	44.4	21.1	25.6
Average	43.5	20.3	23.7
STD	1.10	1.14	1.43

Table 19: Hardness results for screw extruded wires (450Q).
The number in parenthesis represents tempering time in hours.

Sample	450Q(.5)	450Q(2)	450Q(8)	450Q(24)	450Q(96)
1	25	23.9	22.4	24.4	22.3
2	26.3	23.1	23	25.9	23.7
3	26.3	24.7	25.6	24	24
4	24.7	24.6	23.8	24.2	25.1
5	23.5	22.9	22.8	25.5	22.2
6	25.6	24.2	23.5	26	24.9
Average	25.2	23.9	23.5	25.0	23.7
STD	1.1	0.8	1.1	0.9	1.2

Table 20: Hardness results for isothermal tempered wires at 300 °C.
The number in parenthesis represents tempering time in hours.

Sample	300(.25)	300(.5)	300(1)	300(2)	300(4)	300(8)	300(20)	300(24)	300(48)
1	21.9	22	21.3	21.6	21.2	22.9	21.1	20.9	22.5
2	22.6	21.7	21.8	20.7	22.3	22.5	21.7	22.1	23.1
3	22.9	21.9	22.5	22.2	21.9	21.9	21.8	21.1	23
4	22.2	21.7	22.2	22.7	22	22.6	21	22.3	22.5
5	21.9	21.1	22.1	20.8	22.2	22.6	21.1	21.5	23.1
6	22.8	21	22.3	21.4	22.6	22.1	21.2	21.6	22.3
Average	22.4	21.6	22.0	21.6	22.0	22.4	21.3	21.6	22.8
STD	0.4	0.4	0.4	0.8	0.5	0.4	0.3	0.5	0.4

Table 21: Hardness results for isothermal tempered wires at 350 °C.
The number in parenthesis represents tempering time in hours.

Sample	350(0)	350(.5)	350(2)	350(7)	350(24)	350(96)
1	26.4	24.7	27.2	26.7	22.8	26.3
2	27	25.1	26.4	25.6	23.5	25.4
3	26.1	23.8	23.9	24.4	22.5	25.1
4	26.4	24.5	26.3	24.2	24.6	26.9
5	25	25	25.1	26.5	23.7	24.6
6	24.9	25.2	24.9	23.8	23.4	26.6
Average	26.0	24.7	25.6	25.2	23.4	25.8
STD	0.8	0.5	1.2	1.2	0.7	0.9

Table 22: Hardness results for isothermal tempered wires at 400 °C.
The number in parenthesis represents tempering time in hours.

Sample	400(0)	400(.5)	400(2)	400(7)	400(24)	400(96)
1	26.4	25.4	30	26	27.9	23.3
2	25.4	23.4	28.3	25.9	29	23.6
3	25.1	26.2	30	25.7	26.8	24.6
4	28	26.8	26.4	26.7	27.6	23.9
5	27	25	26.7	27.1	29.1	24.5
6	25	23.8	29.5	27.5	27.5	24.2
Average	26.2	25.1	28.5	26.5	28.0	24.0
STD	1.2	1.3	1.6	0.7	0.9	0.5

Table 23: Hardness results for isothermal tempered wires at 450 °C.
The number in parenthesis represents tempering time in hours.

Sample	450(.25)	450(.5)	450(1)	450(2)	450(4)	450(8)	450(20)	450(24)	450(48)
1	21.7	21.5	21.2	22.5	22.2	23.4	21.7	22.6	20.4
2	21.2	21.7	21.2	22	21.3	22.7	22.4	21.7	19.3
3	22.1	21.8	21.8	21.7	21.7	24.5	21.2	21.7	20
4	22.1	21.7	21.3	20.9	21.2	22.1	21.9	21.9	18.6
5	21.9	21.6	21.6	21.5	22.1	22.4	22.2	21.1	19.3
6	22	21.8	22.2	22.1	21.8	25.7	22.5	21.5	20.6
Average	21.8	21.7	21.6	21.8	21.7	23.5	22.0	21.8	19.7
STD	0.3	0.1	0.4	0.6	0.4	1.4	0.5	0.5	0.8

Table 24: Hardness results for isothermal tempered wires at 500 °C.
The number in parenthesis represents tempering time in hours.

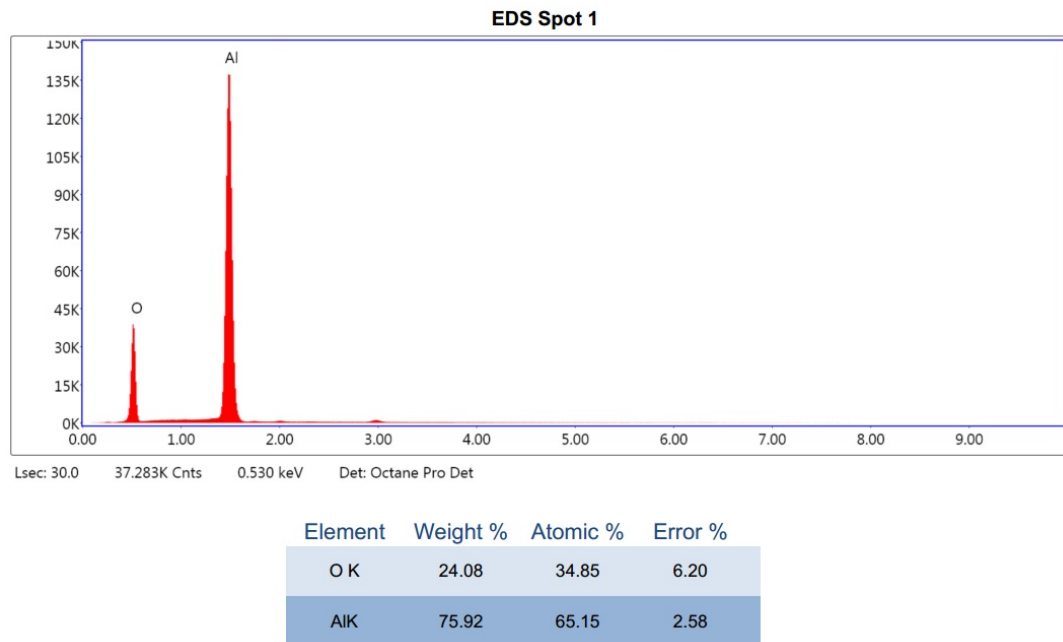
Sample	500(0)	500(.5)	500(2)	500(7)	500(24)	500(96)
1	29.4	29.1	25.3	24.8	27.8	32.5
2	26.7	27.3	25.6	24.9	24.8	30.2
3	30.2	30.3	25.6	25.3	25.2	32.4
4	27.9	28.5	27.1	26.4	23.7	31.1
5	29.7	26.7	28.4	23.8	27	30.2
6	30	28.1	24.6	25.1	26.7	29.5
Average	29.0	28.3	26.1	25.1	25.9	31.0
STD	1.4	1.3	1.4	0.8	1.5	1.2

Table 25: Hardness results for isothermal tempered wires at 560 °C.
The number in parenthesis represents tempering time in hours.

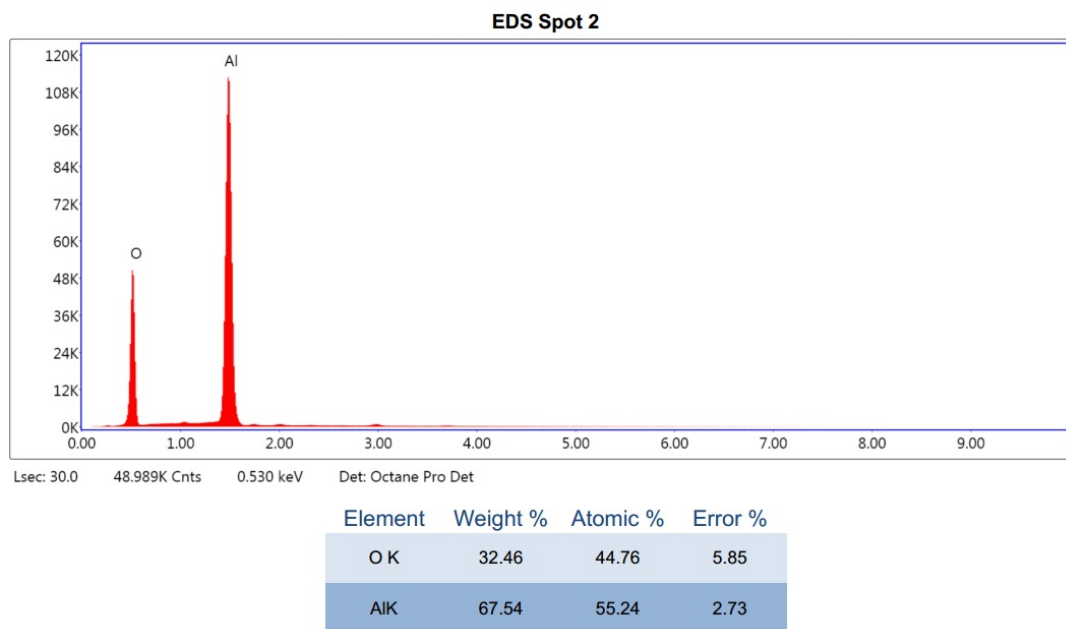
Sample	560(.25)	560(.5)	560(1)	560(2)	560(4)	560(8)	560(19.5)	560(24)	560(48)
1	21.9	22.6	23	22	23	22	21.2	21.2	22.9
2	21	21.3	21.3	21.9	22.7	21	22.5	20.9	23.8
3	22.3	21.8	22.3	21.6	22.9	20.2	22.1	21.5	22.6
4	22.3	22	21.5	22.6	24.4	21.6	22.2	20.8	22.6
5	22.9	22.5	21.9	22.6	23.4	21.6	22	21.4	22.4
6	22.4	23	21.8	22.2	22.2	21.3	22.3	20.4	23.6
Average	22.1	22.2	22.0	22.2	23.1	21.3	22.1	21.0	23.0
STD	0.6	0.6	0.6	0.4	0.7	0.6	0.5	0.4	0.6

D EDS spectra

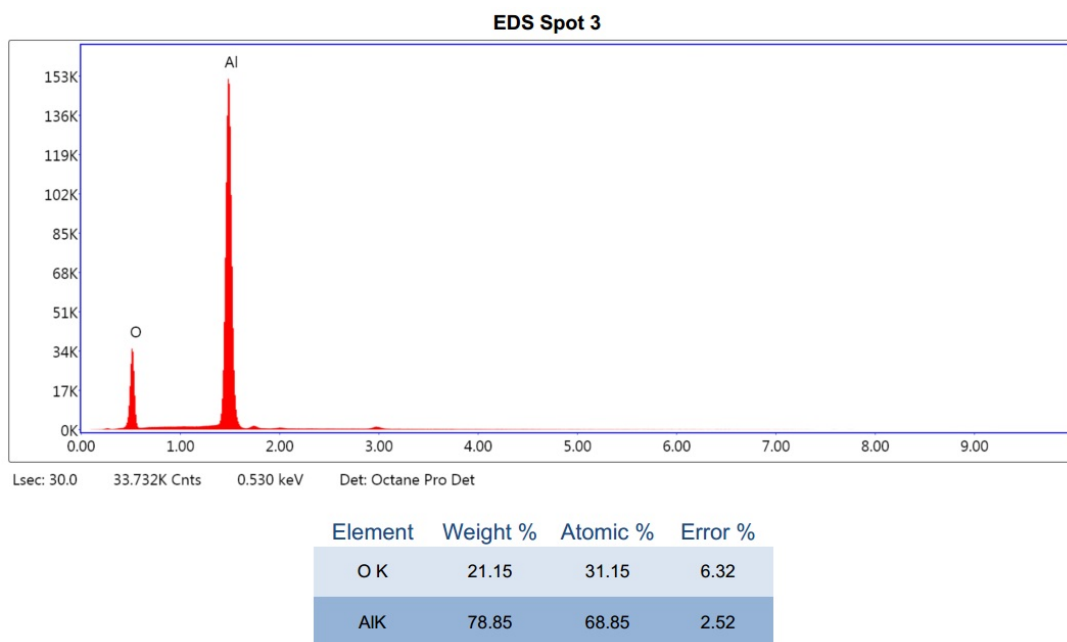
Figure 56 (a)-(e) provides EDS spectra of as-screw extruded wire, examining oxide-containing particles. Figure 57 show the spectra for screw extruded wire after 96 hours of tempering in particles surrounding grain boundaries.



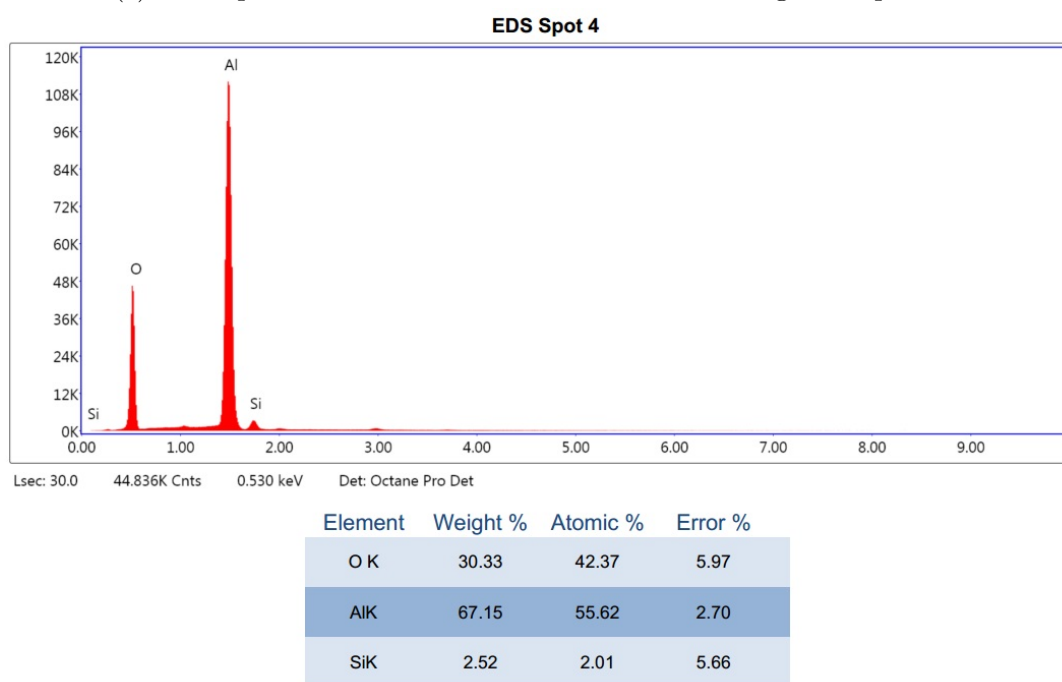
(a) EDS spot 1 for as-screw extruded wire examining oxide particle.



(b) EDS spot 2 for as-screw extruded wire examining oxide particle.

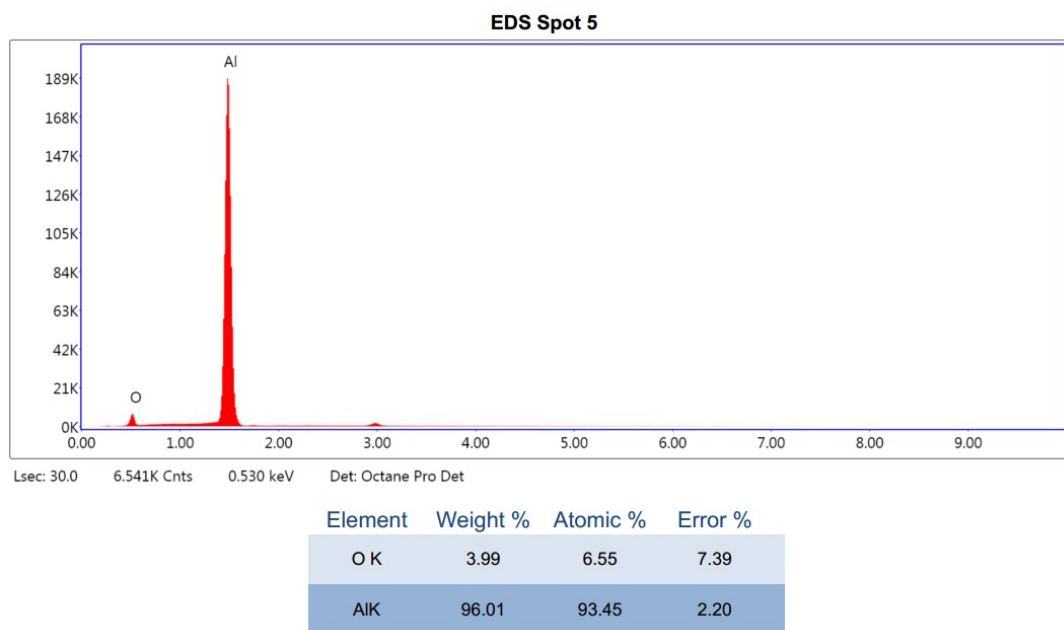


(c) EDS spot 3 for as-screw extruded wire examining oxide particle.



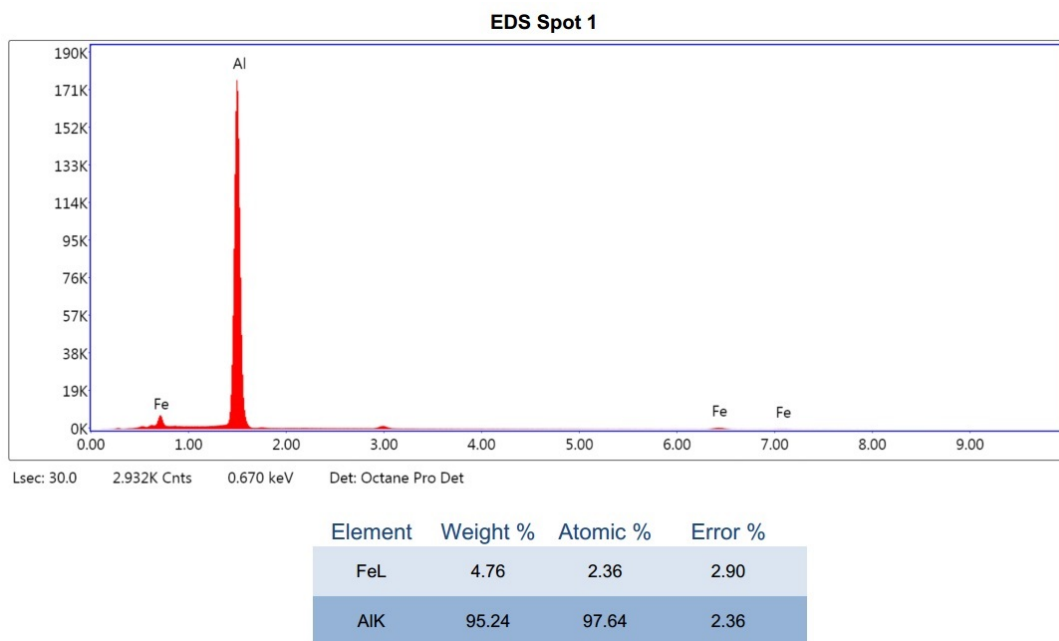
(d) As-extruded at 450 °C.
Longitudinal section.

Figure 56: EDS spot 4 for as-screw extruded wire examining oxide particle.

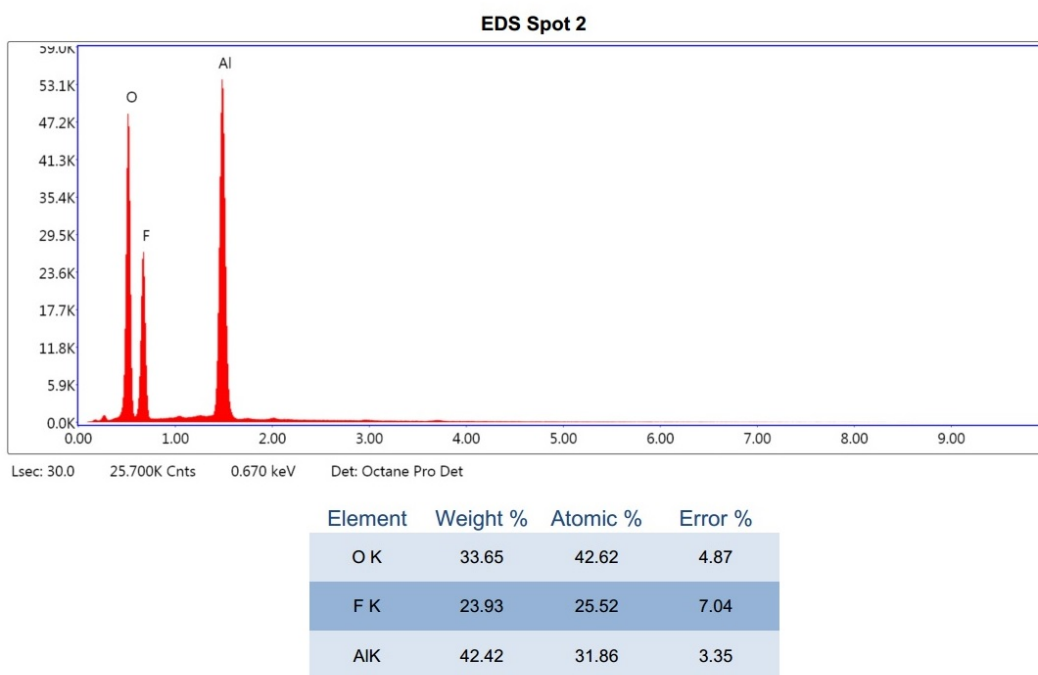


(e) EDS spot 5 for as-screw extruded wire examining oxide particle.

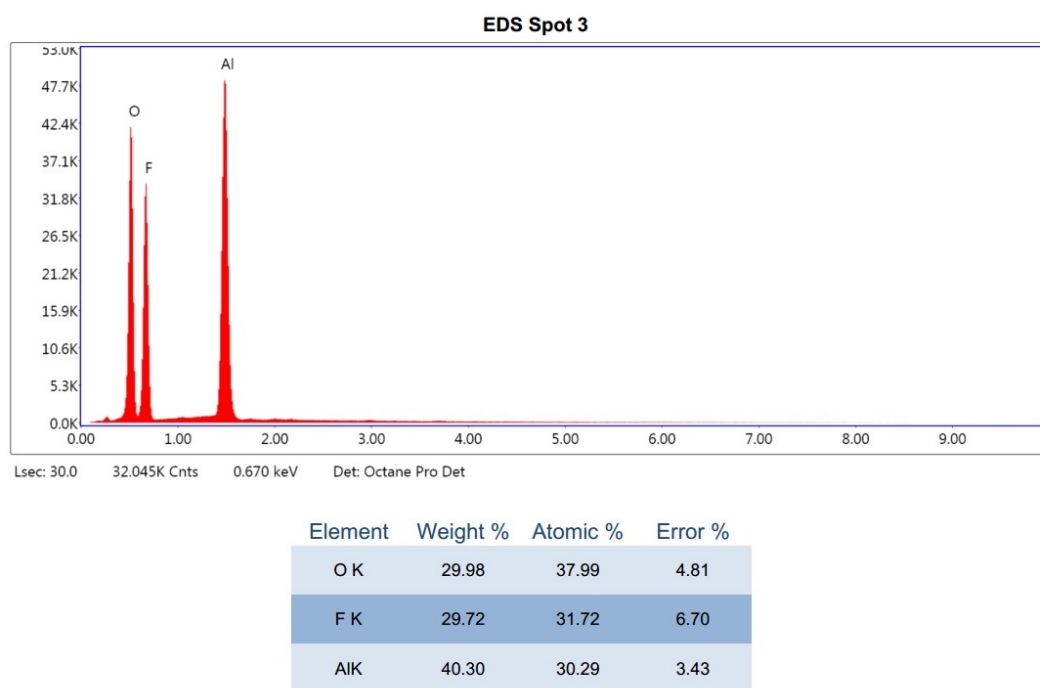
Figure 56: EDS spectra of as-screw extruded wire.



(a) EDS spot 1 for tempered screw extruded wire examining ferrous particle.



(b) EDS spot 2 for tempered screw extruded wire examining oxide particle.



(c) EDS spot 3 for tempered screw extruded wire examining oxide particle.

Figure 57: EDS spectra of screw extruded wire tempered for 96 hours at 450 °C.

E Risk assessment

The risk assessment for this project work, prepared in Riskmanager 4, is provided on the following pages.



ID	16803	Status	Date
Risk Area	Risikovurdering: Helse, miljø og sikkerhet (HMS)	Created	05.01.2017
Created by	Geir Langelandsvik	Assessment started	05.01.2017
Responsible	Geir Langelandsvik	Actions decided	
		Closed	

Master student, 2017, Geir Langelandsvik

Valid from-to date:

-

Location:

3 - Gløshaugen / 304 - Metallurgi / 1050 - 5. etasje

Goal / purpose

Assess the influence of screw extrusion on mechanical and electrical properties.

Background

This project contribute to the examination of the applicability of screw extruded aluminium as electrical conductors.

Description and limitations

Processing of samples by extrusion. Microstructural and mechanical testing. Sample preparation for LM, SEM and TEM

Prerequisites, assumptions and simplifications

Assume changes in the risk assessment as the work gets carried out.

Attachments

[Ingen registreringer]

References

[Ingen registreringer]

**Summary, result and final evaluation**

The summary presents an overview of hazards and incidents, in addition to risk result for each consequence area.

Hazard: Sample preparation**Incident: Eye contact****Consequence area:** HelseRisk before actions:  Risiko after actions: **Incident: Skin contact****Consequence area:** HelseRisk before actions:  Risiko after actions: **Incident: Gas exposure****Consequence area:** HelseRisk before actions:  Risiko after actions: **Incident: Skin contact with epoxy****Consequence area:** Helse
Ytre miljøRisk before actions:  Risiko after actions: 
Risk before actions:  Risiko after actions: **Incident: Finger cutting****Consequence area:** HelseRisk before actions:  Risiko after actions: **Incident: Use of band saw****Consequence area:** HelseRisk before actions:  Risiko after actions: **Incident: Liquid Nitrogen****Consequence area:** HelseRisk before actions:  Risiko after actions: 



Hazard: **Stress testing**

Incident: **Finger pinching**

Consequence area: Helse

Risk before actions:  Risiko after actions: 

Hazard: **Extrusion**

Incident: **Hot work**

Consequence area: Helse

Risk before actions:  Risiko after actions: 

Incident: **Falling objects.**

Consequence area: Helse

Risk before actions:  Risiko after actions: 

Final evaluation

**Units this risk assessment spans**

- NTNU

Participants

Hans Jørgen Roven

Johannes Ofstad

Readers

[Ingen registreringer]

Others involved/stakeholders

Trond Furu

Oddvin Reiso

The following accept criteria have been decided for the risk area Risikovurdering: Helse, miljø og sikkerhet (HMS):

Helse**Materielle verdier****Omdømme****Ytre miljø**

**Overview of existing relevant measures which have been taken into account for this risk assessment**

The table below presents existing measures which have been taken into account when assessing the likelihood and consequence of relevant incidents.

Hazard	Incident	Measures taken into account
Sample preparation	Eye contact	Gloves, labcoat, safety goggles
	Eye contact	Fume cupboard
	Skin contact	Gloves, labcoat, safety goggles
	Gas exposure	Fume cupboard
	Skin contact with epoxy	Gloves, labcoat, safety goggles
	Skin contact with epoxy	Waste handling
	Finger cutting	Gloves, labcoat, safety goggles
	Use of band saw	Face shield
	Use of band saw	Ear protection
	Liquid Nitrogen	Gloves, labcoat, safety goggles
Stress testing	Finger pinching	Gloves, labcoat, safety goggles
	Finger pinching	Supervision with operator
Extrusion	Hot work	Gloves, labcoat, safety goggles
	Hot work	Ear protection
	Hot work	Heat resistant gloves
	Falling objects.	Gloves, labcoat, safety goggles
	Falling objects.	Ear protection
	Falling objects.	Heat resistant gloves
	Falling objects.	Protective footwear

Existing relevant measures with descriptions:**Gloves, labcoat, safety goggles**

To prevent burning damage from operating salt bath.
To prevent skin contact with acids and bases during sample preparation.

Fume cupboard

To prevent gas exposure when handling acids and bases during sample preparation.

Supervision with operator

Tutorial and supervision when handling equipment.

Face shield

To protect from heat and warm liquids

Waste handling

Dispose waste in accordance with local regulation to prevent damage on outside environment.

Ear protection

Ear plug or hearing protection.



Heat resistant gloves

[Ingen registreringer]

Protective footwear

Steel reinforced shoes

Risk analysis with evaluation of likelihood and consequence

This part of the report presents detailed documentation of hazards, incidents and causes which have been evaluated. A summary of hazards and associated incidents is listed at the beginning.

The following hazards and incidents has been evaluated in this risk assessment:

- **Sample preparation**
 - Eye contact
 - Skin contact
 - Gas exposure
 - Skin contact with epoxy
 - Finger cutting
 - Use of band saw
 - Liquid Nitrogen
- **Stress testing**
 - Finger pinching
- **Extrusion**
 - Hot work
 - Falling objects.

Overview of risk mitigating actions which have been decided, with description:

**Sample preparation (hazard)**

Preparing materials for experiments or examination.

Sample preparation/Eye contact (incident)

Use of several chemicals for etching of samples:

Hydrochloric acid (HCl), CAS 7647-01-0:

H290 Kan være etsende for metaller.

H314 Gir alvorlige etseskader på hud og øyne.

H335 Kan forårsake irritasjon av luftveiene.

Sodium hydroxide (NaOH), CAS 1310-73-2:

H290 Kan være etsende for metaller.

H314 Gir alvorlige etseskader på hud og øyne.

Oxalic acid, CAS 144-62-7:

H302 + H312 Farlig ved svelging eller hudkontakt.

H318 Gir alvorlig øyeskade.

Acetone, CAS 67-64-1:

H319 Gir alvorlig øyeirritasjon.

H336 Kan forårsake døsighet eller svimmelhet.

Overall assessed likelihood of the incident:

Unlikely (1)

Comment to likelihood assessment:

Use under cupboard, physical barrier from eyes.
Goggles must be used

Assessment of risk for the consequence area: Helse

Assessed likelihood (common for incident):

Unlikely (1)

Assessed consequence:

Large (3)

Comment to consequence assessment:

May cause blindness.



**Sample preparation/Skin contact (incident)**

Use of several chemicals for etching of samples:

Hydrochloric acid (HCl), CAS 7647-01-0:

H290 Kan være etsende for metaller.

H314 Gir alvorlige etseskader på hud og øyne.

H335 Kan forårsake irritasjon av luftveiene.

Sodium hydroxide (NaOH), CAS 1310-73-2:

H290 Kan være etsende for metaller.

H314 Gir alvorlige etseskader på hud og øyne.

Oxalic acid, CAS 144-62-7:

H302 + H312 Farlig ved svelging eller hudkontakt.

H318 Gir alvorlig øyeskade.

Overall assessed likelihood of the incident:

Less likely (2)

Comment to likelihood assessment:

Use of gloves and lab coat

Assessment of risk for the consequence area: Helse

Assessed likelihood (common for incident):

Less likely (2)

Assessed consequence:

Small (1)

Comment to consequence assessment:

Only minor etch damages

**Sample preparation/Gas exposure (incident)**

Use of several chemicals for etching of samples:

Hydrochloric acid (HCl), CAS 7647-01-0:

H290 Kan være etsende for metaller.

H314 Gir alvorlige etseskader på hud og øyne.

H335 Kan forårsake irritasjon av luftveiene.

Acetone, CAS 67-64-1:

H319 Gir alvorlig øyeyritasjon.

H336 Kan forårsake døsighet eller svimmelhet.

Overall assessed likelihood of the incident:

Less likely (2)

Comment to likelihood assessment:

Use of fume cupboard

Assessment of risk for the consequence area: Helse

Assessed likelihood (common for incident):

Less likely (2)

Assessed consequence:

Medium (2)

Comment to consequence assessment:

Irritation in nose, throat and lungs



**Sample preparation/Skin contact with epoxy (incident)**

Use two components in a mixture to cast samples.

Epofix resin, CAS -:

H315 Irriterer huden.

H317 Kan utløse en allergisk hudreaksjon.

H319 Gir alvorlig øyeirritasjon.

H411 Giftig, med langtidsvirkning, for liv i vann.

Epofix hardener, CAS 112-24-3:

H312 Farlig ved hudkontakt.

H314 Gir alvorlige etseskader på hud og øyne.

H317 Kan utløse en allergisk hudreaksjon.

H412 Skadelig, med langtidsvirkning, for liv i vann.

Overall assessed likelihood of the incident: Less likely (2)

Comment to likelihood assessment:

Use of gloves

Assessment of risk for the consequence area: Helse

Assessed likelihood (common for incident): Less likely (2)

Assessed consequence: Medium (2)

Comment to consequence assessment:

Minor allergic reaction

**Sample preparation/Finger cutting (incident)**

Damaging and cutting fingers on grinding paper

Overall assessed likelihood of the incident: Less likely (2)

Comment to likelihood assessment:

Use gloves

Assessment of risk for the consequence area: Helse

Assessed likelihood (common for incident): Less likely (2)

Assessed consequence: Small (1)

Comment to consequence assessment:

Minor wound





Sample preparation/Use of band saw (incident)

Risk of cutting fingers.

Overall assessed likelihood of the incident: Less likely (2)

Comment to likelihood assessment:

Cutting large plates, hand far away from the saw blade

Assessment of risk for the consequence area: Helse

Assessed likelihood (common for incident): Less likely (2)

Assessed consequence: Large (3)

Comment to consequence assessment:

May lose fingers



Sample preparation/Liquid Nitrogen (incident)

Handling cold liquid N2 (-196 C)

Overall assessed likelihood of the incident: Less likely (2)

Comment to likelihood assessment:

[Ingen registreringer]

Assessment of risk for the consequence area: Helse

Assessed likelihood (common for incident): Less likely (2)

Assessed consequence: Medium (2)

Comment to consequence assessment:

Do not harm the skin in direct contact. Metal parts (jewels) and eyes must not be exposed



**Stress testing (hazard)**

Use of tensile test machine.

Stress testing/Finger pinching (incident)

Danger of pinching fingers in the machinery

Overall assessed likelihood of the incident: Less likely (2)

Comment to likelihood assessment:

Supervision with operator ensures right handling procedures of samples when testing

Assessment of risk for the consequence area: Helse

Assessed likelihood (common for incident): Less likely (2)

Assessed consequence: Large (3)

Comment to consequence assessment:

May cause large wounds on fingers. Testing should not precede if incident happens

**Extrusion (hazard)**

Making aluminium profiles by screw extrusion

Extrusion /Hot work (incident)

Handling warm metals (steel and aluminium) during experimental work.

Overall assessed likelihood of the incident: Likely (3)

Comment to likelihood assessment:

Easy to touch warm objects while handling a fast operation

Assessment of risk for the consequence area: Helse

Assessed likelihood (common for incident): Likely (3)

Assessed consequence: Medium (2)

Comment to consequence assessment:

The touching time will be very low. Easy access to water and medical equipment.





Extrusion /Falling objects. (incident)

This work involves moving heavy steel components by hand.

Overall assessed likelihood of the incident: Less likely (2)

Comment to likelihood assessment:

Good grip on all components

Assessment of risk for the consequence area: Helse

Assessed likelihood (common for incident): Less likely (2)

Assessed consequence: Medium (2)

Comment to consequence assessment:

No components exceed 50 kg, and are never carried over 70 cm height.





Overview of risk mitigating action which have been decided:

Below is an overview of risk mitigating actions, which is intended to contribute towards minimizing the likelihood and/or consequence of incidents:

Overview of risk mitigating actions which have been decided, with description:

